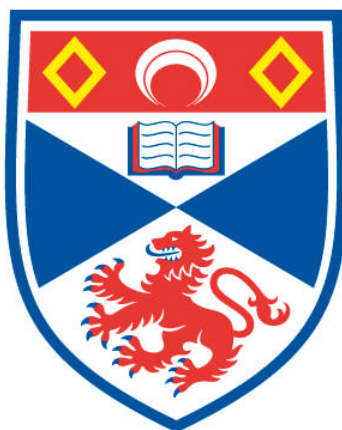


# **COORDINATIVELY UNSATURATED METAL ORGANIC FRAMEWORKS FOR OLEFIN SEPARATIONS**

**Catherine Louise Renouf**

**A Thesis Submitted for the Degree of PhD  
at the  
University of St Andrews**



**2013**

**Full metadata for this item is available in  
Research@StAndrews:FullText  
at:**

**<http://research-repository.st-andrews.ac.uk/>**

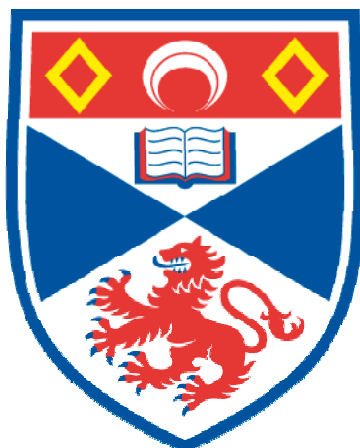
**Please use this identifier to cite or link to this item:**

**<http://hdl.handle.net/10023/3686>**

**This item is protected by original copyright**

**This item is licensed under a  
Creative Commons License**

Coordinatively unsaturated metal organic  
frameworks for olefin separations



University of  
St Andrews

**Catherine Louise Renouf MChem**

A thesis submitted in application for the degree of  
*Doctor of Philosophy*

in the Faculty of Science at the University of St Andrews

26<sup>th</sup> March 2013





## ***Acknowledgements***

Firstly, thank you to both of my supervisors, Russell Morris and Ronan Bellabarba, for their help and guidance throughout this project.

I am hugely grateful to Simon Teat and Christine Beavers on Beamline 11.3.1 at the ALS for their immense patience and trust during gas cell experiments. Thanks also to engineers Jason Knight and Jamie Nasiatka for their expertise developing the gas cell at the ALS and to Doug Taube for enlightening and entertaining discussions during beamtime.

Thanks to my colleagues who have variously driven me mad and preserved my sanity during many long hours of beamtime, namely Phoebe Allan, Sam Morris, Laura McCormick, Becca Randall, Paul Wheatley and Dave Aldous. Thanks also to the other Morris group members who have helped with my research and become good friends along the way, particularly Alistair McKinlay, Morven Duncan and Bo Xiao.

A special thanks goes to Phoebe Allan; I can't think of a better person with whom to spend two months of beamtime.

Of course, I must thank my parents, Frank and Brenda, and my sister, Lizzie, for their support and encouragement throughout my PhD and the rest of my education.

Finally, thank you to the EPSRC and Sasol Technology UK Ltd. for providing the funding that has allowed me to carry out this research.

## **Abstract**

The research presented in this thesis aims to assess the capacity of metal organic frameworks with open metal sites for the separation of olefin mixtures.

Chapter 1 provides a background to the field, including industrial separation techniques, metal organic frameworks and their applications and the current state-of-the-art for olefin separation. Chapter 3 describes the experimental techniques used in this research.

Ethylene and propylene adsorption and desorption isotherms on Ni-CPO-27 and HKUST-1 at a range of temperatures are presented and compared in Chapter 4, and used to calculate isosteric heats of adsorption at varying coverages using the virial method. These pure component isotherms are used in Chapter 5 to predict selectivities for the separation of binary mixtures using ideal adsorbed solution theory. Temperature programmed desorption is used in Chapter 5 to calculate the enthalpy of desorption using Redhead's method and the heating rate variation method, and the two results are compared. The results presented in Chapters 4 and 5 conclude that propylene/ethylene separation is possible using adsorption onto metal organic frameworks with open metal sites.

A new *in situ* environmental gas cell for single crystal X-ray diffraction is developed in Chapter 6, and the challenges encountered during this development process are discussed. The dehydration of one framework, Co-CPO-27, is studied in detail using the environmental gas cell. A dehydrated structure of HKUST-1, obtained using the gas cell, is presented for the first time.

Crystal structures for the complete dehydration-adsorption-delivery cycle for biologically active NO on Co-CPO-27 are presented in Chapter 7, showing the utility of the *in situ* gas cell for prolonged experiments in multiple different gaseous environments. The crystal structure of NO-loaded Co-CPO-27 improves upon the models suggested in the literature, and the treatment of the dual occupancy of the open metal sites by water and NO is discussed in depth. A crystal structure of CO-loaded Co-CPO-27 is obtained for the first time, and crystal structures of Co-CPO-27 in ethylene and propylene environments are presented.

# TABLE OF CONTENTS

Declaration.....	2
Courses Attended .....	3
Acknowledgements .....	4
Abstract.....	5
<b>CHAPTER 1: INTRODUCTION.....</b>	<b>10</b>
1.1 Gas separation.....	10
1.1.1 Adsorptive separation .....	11
1.1.2 Olefin separation.....	12
1.1.2.1 Fischer-Tropsch process .....	12
1.1.2.2 Industrial separation .....	13
1.2 Metal organic frameworks .....	14
1.2.1 Applications .....	15
1.2.1.1 Gas storage .....	15
1.2.1.2 Gas separation .....	17
1.2.1.3 Other applications.....	19
1.3 MOFs for hydrocarbon separations .....	25
1.3.1 Olefin/paraffin separation .....	25
1.3.2 Ethylene/acetylene separation .....	27
1.3.3 Olefin separation.....	29
1.4 References.....	30
<b>CHAPTER 2: AIMS.....</b>	<b>33</b>
<b>CHAPTER 3: EXPERIMENTAL TECHNIQUES.....</b>	<b>34</b>
3.1 Gas adsorption .....	34
3.1.1 Langmuir theory <sup>1,2</sup> .....	34
3.1.2 BET theory <sup>1,2</sup> .....	35
3.1.3 Chemisorption and physisorption <sup>2,5</sup> .....	37
3.1.4 Enthalpy of adsorption .....	40
3.1.5 Gravimetric adsorption.....	41

3.1.5.1	Experimental <sup>12</sup> .....	41
<b>3.2</b>	<b>Gas desorption</b> .....	<b>43</b>
3.2.1	Temperature programmed desorption.....	43
3.2.1.1	Experimental .....	43
3.2.2	Enthalpy of desorption .....	44
<b>3.3</b>	<b>Single crystal X-ray diffraction</b> .....	<b>45</b>
3.3.1	Synchrotron radiation .....	45
3.3.2	Beamline 11.3.1.....	46
3.3.3	Structure solution and refinement.....	46
<b>3.4</b>	<b>References</b> .....	<b>47</b>

## **CHAPTER 4: OLEFIN ADSORPTION IN COORDINATIVELY**

### **UNSATURATED MOFS.....49**

<b>4.1</b>	<b>Introduction</b> .....	<b>49</b>
4.1.1	M-CPO-27.....	49
4.1.1.1	Olefin adsorption .....	51
4.1.2	HKUST-1 .....	53
4.1.2.1	Olefin adsorption .....	55
4.1.3	STAM-1 .....	58
<b>4.2</b>	<b>Aims</b> .....	<b>60</b>
<b>4.3</b>	<b>M-CPO-27 results</b> .....	<b>61</b>
4.3.1	Ethylene .....	61
4.3.2	Propylene .....	68
<b>4.4</b>	<b>HKUST-1 results</b> .....	<b>70</b>
4.4.1	Ethylene .....	70
4.4.2	Propylene .....	77
<b>4.5</b>	<b>STAM-1 results</b> .....	<b>84</b>
4.5.1	Ethylene .....	84
4.5.2	Propylene .....	85
<b>4.6</b>	<b>Comparisons</b> .....	<b>86</b>
<b>4.7</b>	<b>Summary</b> .....	<b>87</b>
<b>4.8</b>	<b>References</b> .....	<b>88</b>

## **CHAPTER 5: OLEFIN SEPARATION USING COORDINATIVELY**

### **UNSATURATED MOFS.....90**

<b>5.1</b>	<b>Aims</b> .....	<b>90</b>
<b>5.2</b>	<b>Ideal adsorbed solution theory</b> .....	<b>90</b>
5.2.1	Ni-CPO-27 .....	91
5.2.2	HKUST-1 .....	92
5.2.3	Comparisons.....	94
<b>5.3</b>	<b>Desorption</b> .....	<b>95</b>
5.3.1	Ni-CPO-27 .....	95
5.3.2	HKUST-1 .....	98
<b>5.4</b>	<b>Summary and further work</b> .....	<b>101</b>
<b>5.5</b>	<b>References</b> .....	<b>102</b>

## **CHAPTER 6: DEVELOPMENT OF A STATIC GAS CELL FOR *IN SITU***

### **SINGLE CRYSTAL X-RAY DIFFRACTION .....103**

<b>6.1</b>	<b>Declaration</b> .....	<b>103</b>
<b>6.2</b>	<b>Introduction</b> .....	<b>103</b>
6.2.1	SRS, beamline 9.8.....	104
6.2.2	Co-CPO-27 .....	105
6.2.3	HKUST-1 .....	106
<b>6.3</b>	<b>ALS beamline 11.3.1</b> .....	<b>106</b>
6.3.1	General experimental procedure .....	112
6.3.2	Gas cell improvements .....	113
<b>6.4</b>	<b>Dehydration</b> .....	<b>115</b>
6.4.1	Co-CPO-27.....	115
6.4.2	HKUST-1 .....	121
<b>6.5</b>	<b>Summary</b> .....	<b>123</b>
<b>6.6</b>	<b>CIF key</b> .....	<b>125</b>
<b>6.7</b>	<b>References</b> .....	<b>126</b>

## CHAPTER 7: *IN SITU* GAS ADSORPTION SINGLE CRYSTAL STUDIES

.....	<b>127</b>
<b>7.1 Aims</b> .....	<b>127</b>
<b>7.2 Nitric oxide</b> .....	<b>127</b>
7.2.1 Applications .....	129
7.2.2 Previous work .....	131
7.2.3 Experimental .....	133
7.2.4 Results.....	134
7.2.4.1 Dehydrated Co-CPO-27 .....	134
7.2.4.2 NO-loaded Co-CPO-27.....	135
7.2.4.3 NO delivery .....	141
7.2.5 Discussion.....	142
<b>7.3 Carbon monoxide</b> .....	<b>145</b>
7.3.1 Applications .....	146
7.3.2 Previous work .....	147
7.3.3 Experimental .....	149
7.3.4 Results.....	149
<b>7.4 Olefins</b> .....	<b>152</b>
7.4.1 Ethylene and propylene .....	152
7.4.1.1 Previous work .....	152
7.4.1.2 Experimental .....	153
7.4.1.3 Results.....	153
<b>7.5 Summary</b> .....	<b>157</b>
<b>7.6 CIFs</b> .....	<b>158</b>
<b>7.7 References</b> .....	<b>159</b>
<b>CHAPTER 8: CONCLUSIONS AND FURTHER WORK</b> .....	<b>161</b>

# CHAPTER 1: Introduction

## **1.1 Gas separation**

The separation of gases is undertaken to fulfil three primary functions; concentration, fractionation and purification. Industrially, 90-95 % of all chemical processes involve distillation, with other methods of gas purification including absorption and adsorption.

Fractional distillation is used in crude oil refinery to separate the crude oil into its more useful component parts, namely petroleum gas, petrol, naphtha, kerosene, diesel and asphalt, while impurities such as sulfur and water are removed. Crude oil fractionation is typically carried out at approximately 350 °C.<sup>1</sup> Distilled spirits are produced in a similar way, where dilute ethanol solutions are distilled to produce a condensate that contains a high percentage of ethanol alongside water, esters and other alcohols.

Gas separation by absorption is also known as scrubbing, where a liquid is used to remove pollutants from a gas stream. The flue gas comes into contact with a counter-flow of solution droplets and soluble pollutants such as sulfoxides dissolve in the water and are removed from the stream.<sup>2</sup>

Gas purification by adsorption requires a supporting, usually porous, material. Many examples exist in industry for applications as diverse as gas masks, sensors and gas stream purification. A huge variety of porous materials have been explored as adsorbents such as activated carbon, zeolites and carbon nanotubes. Early gas masks used during the First World War, for example, contained activated charcoal to adsorb poisonous gases, while modern gas masks contain filters carefully selected according to the toxic compounds they may encounter.

### 1.1.1 Adsorptive separation

Gas molecules in contact with a solid interact with its surface to form a thin film in a process termed adsorption. Adsorption can occur through intermolecular forces such as van der Waals interactions or through the formation of chemical bonds between the gaseous molecule and the solid surface: physisorption and chemisorption, respectively.

In adsorptive separation, a mixture of gases is flowed over a solid adsorbent, or 'support'. This adsorbent is carefully chosen so that it preferentially adsorbs some of the gases in a mixture, retaining them within the support whilst allowing the others to flow through more freely. This is different to molecular sieving, where size differences between gas molecules and the support's pores exclude some gaseous molecules.

A substrate must display a number of characteristics for it to be suitable for adsorptive separation. It must have a high adsorption capacity and a high selectivity for the gases it is to remove from the mixture; both depend upon the nature of the adsorbent, such as chemical properties, pore size and surface area, and the conditions of the separation, such as temperature and pressure. Desorption of the adsorbed gas must also be considered, as regeneration of the adsorbent must be easy and complete enough to give a large working capacity; processes such as temperature swing adsorption (TSA) and pressure swing adsorption (PSA) use changes in temperature and pressure to regenerate the adsorbent after saturation.<sup>3</sup> The mechanical properties of the adsorbent must be such that it can withstand the temperatures and pressures it will encounter in an industrial setting. Adsorption capacity should remain high after many adsorption-desorption cycles in order for a separation process to be useful, without poisoning of the adsorption sites by other species.

Several techniques are used to explore the separation performance of an adsorbent. Initial experiments often involve adsorption isotherms and pulse testing of single component systems, allowing the comparison of characteristics such as surface areas, adsorption capacities and enthalpies of adsorption and desorption. The separation capacity of an adsorbent can be predicted from such results and breakthrough curves are often calculated computationally while experimental

breakthrough measurements and chromatographic separations can be carried out in a lab-based setting.<sup>3,4</sup>

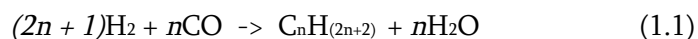
## 1.1.2 Olefin separation

### 1.1.2.1 Fischer-Tropsch process

The Fischer-Tropsch process, used to produce liquid hydrocarbons from coal, natural gas or, more recently, biomass, was invented in the 1920s in Germany by Franz Fischer and Hans Tropsch. Germany had little access to petroleum during World War II but possessed huge amounts of coal, so the Fischer-Tropsch process was used extensively alongside coal hydrogenation plants to produce diesel for the war effort.<sup>5</sup>

South Africa also lacked petroleum access but possessed large coal reserves, and in 1955 Sasol began to produce liquid fuels from coal in Sasolburg, South Africa. As well as diesel fuel, Sasol produces a variety of synthetic petroleum products such as plastics and waxes.<sup>6</sup> High capital costs and high operation and maintenance costs restrict the popularity of synthetic oil from natural gas, as often the direct sale of natural gas to consumers is more profitable. However, in very coal-rich places like South Africa, or in places where the natural gas is far away from cities and too impractical to pipe, the Fischer-Tropsch process remains invaluable. In the future, it is likely that biofuels will be produced through a combination of biomass gasification and the Fischer-Tropsch process.<sup>7</sup>

A series of chemical reactions is used to convert carbon monoxide and hydrogen gas into liquid hydrocarbons, represented by the general equation (1.1). Most Fischer-Tropsch processes use cobalt, iron or ruthenium catalysts at temperatures between 150 and 300 °C.<sup>8</sup>



The production of alkanes is desired, although methane is usually avoided due to its low boiling point. Small amounts of impurities including olefins (alkenes), alcohols and oxygenated hydrocarbons are also formed. Separation of these impurities from the alkanes is necessary to produce pure syncrude, and the impurities can be converted into other useful products such as textiles, paints and detergents.

### 1.1.2.2 Industrial separation

Some olefins have boiling points very similar to one another (Table 1.1), preventing their separation by distillation.<sup>9</sup> Current methods of separation involve cryogenic distillation instead, which is highly energy intensive and expensive.<sup>10</sup>

Table 1.1: Boiling points of olefins similar to 1-pentene and 1-hexene.

Olefin	Normal boiling point / °C
3-methyl-1-butene	20.10
<b>1-pentene</b>	<b>29.96</b>
2-methyl-1-butene	31.20
<i>trans</i> -2-pentene	36.34
<i>cis</i> -2-pentene	36.93
4-methyl- <i>trans</i> -2-pentene	58.30
2-methyl-1-pentene	62.10
<b>1-hexene</b>	<b>63.48</b>
2-ethyl-1-butene	64.70
<i>cis</i> -3-hexene	66.40

Electrochemical separation has been investigated as an alternative approach. Olefins react with 1,2-ene-dithiolate complexes and smaller chains have smaller rate constants, allowing for kinetic separation.<sup>11</sup> Similarly, etherification of branched olefins with methanol over an acidic catalyst takes place without reaction of linear olefins, allowing for separation of the unwanted branched products.<sup>12</sup> The isolated products from these techniques are not commercially useful and must be processed further requiring additional expense, so neither method is ideal for use within industry.

## **1.2 Metal organic frameworks**

The International Union of Pure and Applied Chemistry (IUPAC) has recently published provisional recommendations for defining metal organic frameworks (MOFs), coordination polymers and coordination networks. A coordination polymer is defined as a compound extending infinitely in 1-, 2- or 3-dimensions through coordination bonds. A coordination network is similar, with a compound extending in 1-dimension through coordination bonds but in 2- or 3-dimensions through crosslinking. A MOF can be either a coordination polymer or a coordination network, but must additionally contain potential voids due to an open framework structure.<sup>13</sup>

A MOF is constructed of metal ions or clusters connected together in 1-, 2- or 3-dimensions by coordination bonds with multidentate organic linkers. These organic linkers are most frequently carboxylate ligands, with other common linkers including pyridyl, nitrile and sulfonate groups.

MOFs are usually synthesised using hydrothermal or solvothermal methods, but other techniques such as ionothermal synthesis, microwave synthesis and mechanical synthesis are increasingly employed. Vapour diffusion and layering can produce good quality single crystals in small quantities, so these methods are often used when structural studies using single crystal X-ray diffraction are required.

In many cases MOFs contain pores that usually hold either solvent molecules or, in the case of charged frameworks, counterions.<sup>14</sup> Different shaped organic linkers produce different shaped pores within the framework. Longer linkers can produce larger pores in frameworks with otherwise identical topology, termed isorecticular MOFs (IRMOFs), until interpenetration is observed where separate but identical frameworks connect together like links in a chain (Figure 1.1).<sup>15</sup>

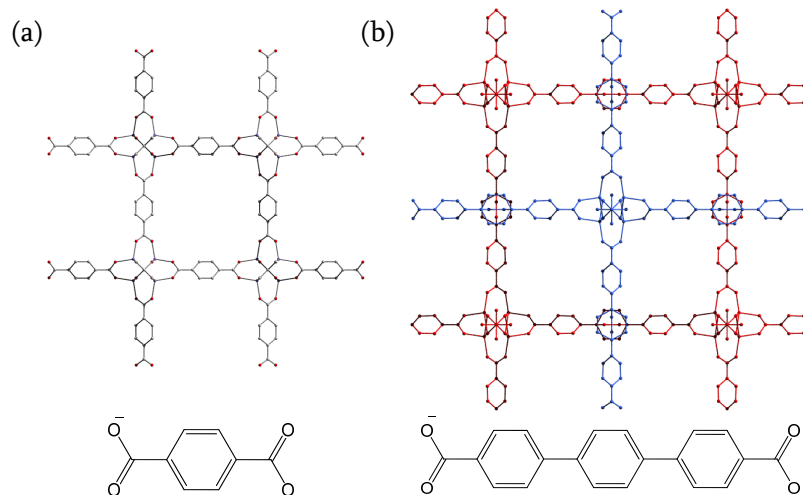


Figure 1.1: (a) MOF-5 ( $Zn_4(O)(BDC)_3$ ) and its organic linker, 1,4-benzenedicarboxylate (BDC) (zinc atoms are shown in purple, oxygen in red and carbon in grey; hydrogen atoms are omitted for clarity); (b) interpenetrated IRMOF-15 ( $Zn_4(O)(TPDC)_3$ ) and its organic linker, [1,1':4',1''-terphenyl]-4,4''-dicarboxylate (TPDC). The two interpenetrating frameworks are shown in different colours.

## 1.2.1 Applications

High porosity provides MOFs with very high surface areas in proportion to their mass, and this can be exploited in the same way as any other surface. Most MOF research has historically centred on hydrogen and  $CO_2$  storage, gas separations and catalysis, but other more diverse applications are increasingly reported including drug delivery, biomedical imaging, electrochemistry and luminescence.

### 1.2.1.1 Gas storage

Increasing awareness of the environmental impact of the use of fossil fuels for energy generation has led to a search for alternative fuels, particularly as a replacement for petrol. Similarly, the capture of harmful gases close to their point of generation before their release into the environment is desirable. MOFs with high surface areas offer a high gas storage density. Those with exposed metals or ligands allow interactions between the gas molecules and the framework, increasing storage capacity further.<sup>16</sup> The storage of potential fuel gases such as hydrogen and methane using MOFs instead of traditional gas cylinders would be particularly advantageous, as storage within a MOF would avoid the need for transporting flammable gases under high pressures.

The requirements for gas storage are similar to those for other applications that utilise a MOF's porosity. The pores and pore windows must be large enough to allow the gas to pass through and the interactions between the gas and the framework must be strong enough to retain the gas within the pores. Release of the gas when required must be controllable and straightforward.

These requirements can be achieved by the appropriate choice of metal and ligand. Methane storage, for example, can be significantly improved by favourable interactions between guest methane molecules and the organic linker. The Zn-based MOF, IRMOF-6 (Figure 1.2), containing cyclobutabenzene-dicarboxylate linkers, has a pore opening of 5.9 Å, which is large enough to incorporate a methane molecule. IRMOF-6 has a remarkably high methane uptake of 240 cm<sup>3</sup> (STP, standard temperature and pressure) g<sup>-1</sup>. The amount of methane adsorbed by the framework at 36 atm, a pressure considered safe and cost-effective, is equal to 70 % of the amount of methane stored in compressed gas cylinders at a more hazardous pressure of 205 atm. Similar MOFs with different linkers but analogous framework topologies showed significantly lower methane capacities; the exceptional capacity of IRMOF-6 is attributed to the increased interactions between methane and the hydrophobic C<sub>2</sub>H<sub>4</sub> units within the linker.<sup>15</sup>

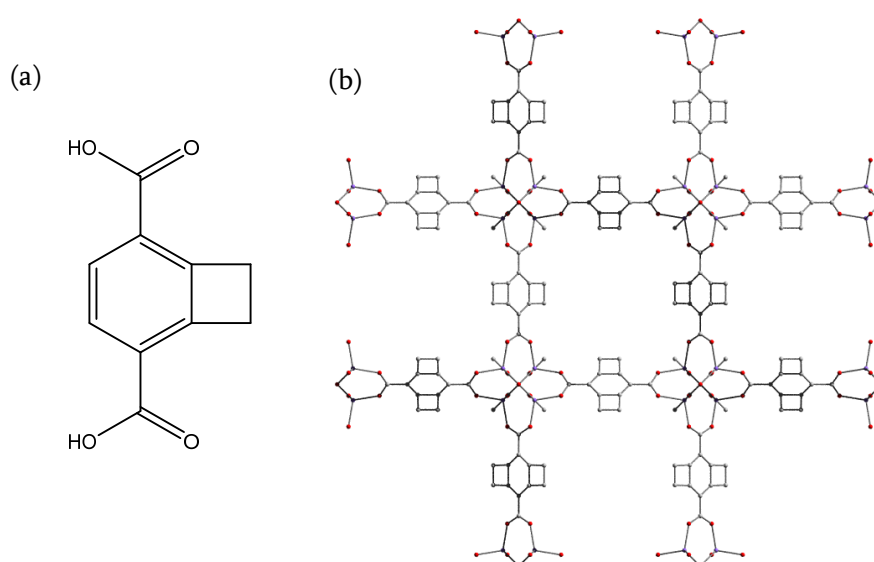


Figure 1.2: (a) Organic linker, 1,2-dihydrocyclobutabenzene-3,6-dicarboxylic acid; (b) crystal structure of IRMOF-6 (zinc atoms shown in purple, oxygen in red and carbon in grey; hydrogen atoms and solvent molecules omitted for clarity).

### 1.2.1.2 Gas separation

Separation of CO<sub>2</sub> from other gases is important for a range of reasons. Carbon capture and storage to reduce CO<sub>2</sub> emissions involves the removal of CO<sub>2</sub> from flue gases at power plants. Additionally, removal of CO<sub>2</sub> from methane streams is important in the upgrading of natural gas. As such, separation of CO<sub>2</sub> from mixtures with N<sub>2</sub>, CH<sub>4</sub>, O<sub>2</sub>, H<sub>2</sub>, CO and Ar using MOF adsorption has been studied extensively.<sup>4</sup>

A series of zeolitic imidazolate frameworks (ZIFs) with functional groups pointing into the pores demonstrate the influence that the interactions between dipolar CO<sub>2</sub> and a polar framework have on CO<sub>2</sub> selectivity. The functional groups -PhNO<sub>2</sub>, -CN, -PhBr, -PhCl, -Ph and -PhMe vary both the diameter of the pore openings and the polarity of the framework (Table 1.2). CO<sub>2</sub> uptake is independent of the size of the pore opening, but dependent upon the polarity of the functional group. Calculated selectivities for CO<sub>2</sub>/CH<sub>4</sub>, CO<sub>2</sub>/N<sub>2</sub> and CO<sub>2</sub>/O<sub>2</sub> mixtures clearly demonstrate that the separation of CO<sub>2</sub> mixtures using functionalised ZIFs is due to interactions with the framework functional groups and not due to a size selective effect (Figure 1.3).

Table 1.2: Functional groups and pore openings of functionalised ZIFs. ZIFs ordered from highest to lowest CO<sub>2</sub> uptake according to CO<sub>2</sub> adsorption isotherms, as shown in Figure 1.3(b).

Functional group	Name	Pore opening / Å
-PhNO <sub>2</sub>	ZIF-78	3.8
-CN	ZIF-82	8.1
-PhCl	ZIF-69	4.4
-PhBr	ZIF-81	3.9
-Ph	ZIF-68	7.5
-PhMe	ZIF-79	4.0
None	ZIF-70	13.1

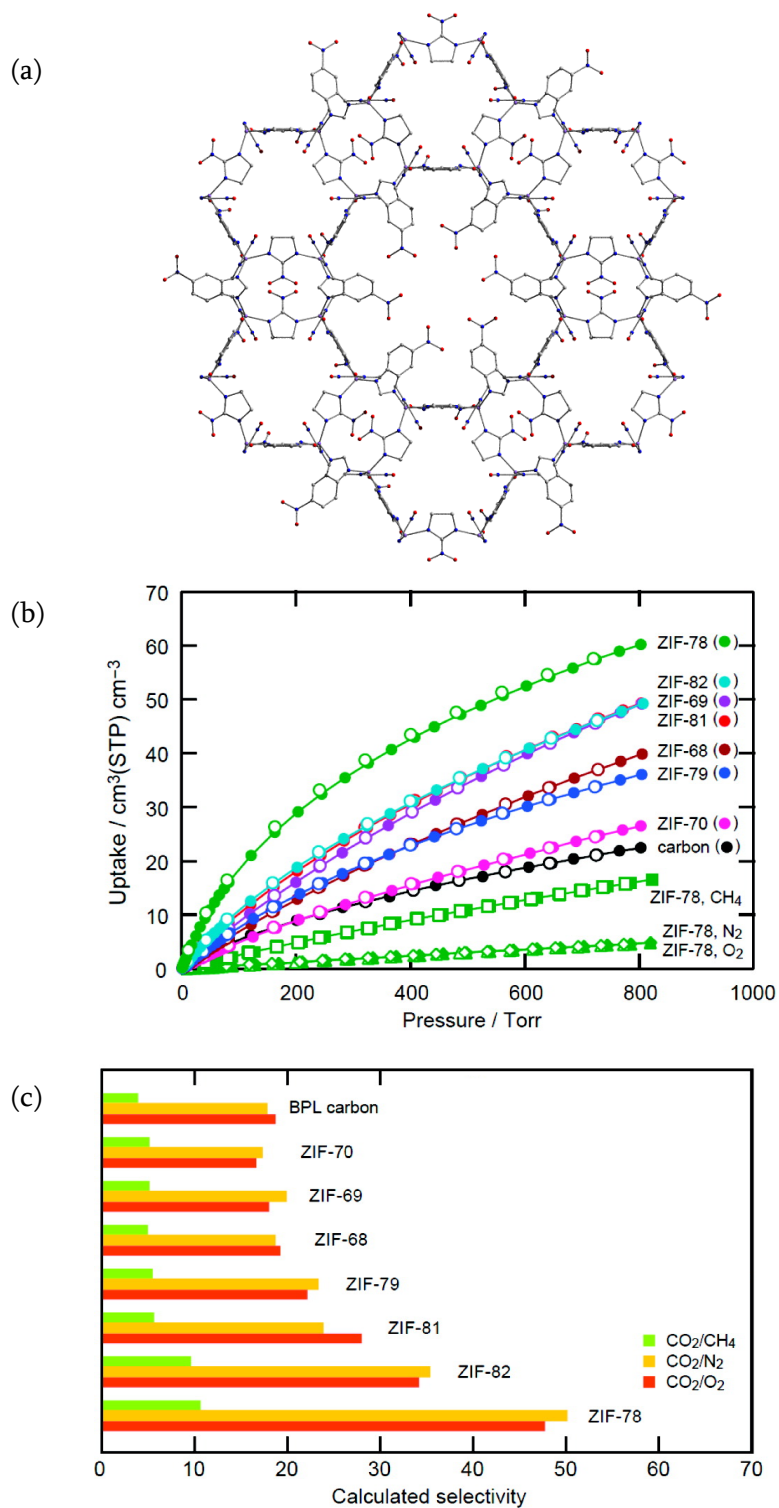


Figure 1.3: (a) Crystal structure of ZIF-78 (zinc atoms shown in purple, oxygen in red and carbon in grey; hydrogen atoms omitted for clarity). -NO<sub>2</sub> functional groups are split over two sites, so one site is displayed for simplification; (b) CO<sub>2</sub> adsorption isotherms of ZIFs and BPL carbon, currently used in industry; (c) calculated CO<sub>2</sub>/CH<sub>4</sub>, CO<sub>2</sub>/N<sub>2</sub> and CO<sub>2</sub>/O<sub>2</sub> selectivities of ZIFs and BPL carbon. (b) and (c) adapted from reference 17.

Natural gas offers a cleaner alternative to energy production in comparison to other fossil fuels, particularly petrol, and is also safer in the event of a spill. However, hydrogen sulfide in parts per million (ppm) levels must be removed from methane before its transportation in order to prevent corrosion of the pipelines. Adsorption onto porous solids offers an attractive solution that prevents the use of other chemicals or energy-intensive processes. A vanadium(IV)-containing MOF with BDC linkers, MIL-47(V) (MIL = Materials Institute Lavoisier; Figure 1.4), demonstrates a higher capacity for adsorption of H<sub>2</sub>S than for CH<sub>4</sub>, with simulation experiments suggesting a selectivity of approximately 30 for H<sub>2</sub>S versus CH<sub>4</sub> at 1.0 MPa. H<sub>2</sub>S adsorption onto MIL-47(V) is reversible and leaves the framework undamaged for further adsorption cycles to proceed, whereas a similar iron(III)-framework, MIL-53(Fe), was destroyed by treatment with H<sub>2</sub>S.<sup>18</sup>

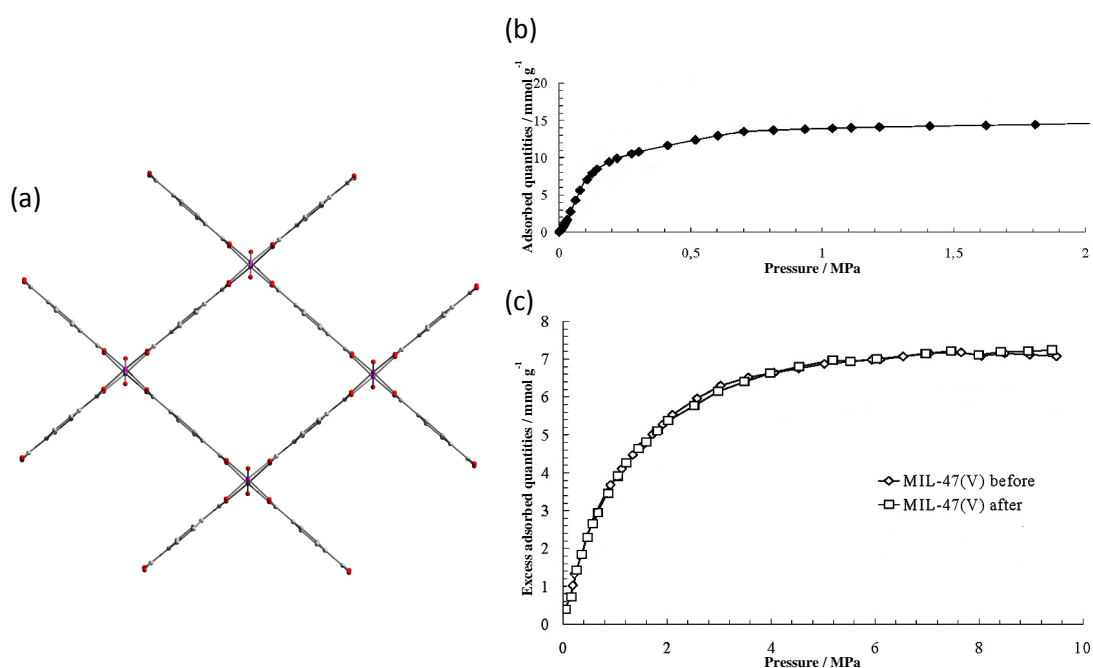


Figure 1.4: (a) Crystal structure of MIL-47(V)<sup>19</sup> (vanadium atoms shown in pink, oxygen in red and carbon in grey; hydrogen atoms omitted for clarity); (b) H<sub>2</sub>S adsorption isotherm on MIL-47(V); (c) CH<sub>4</sub> adsorption isotherms on MIL-47(V) before and after H<sub>2</sub>S exposure/delivery. (b) and (c) adapted from reference 18.

### 1.2.1.3 Other applications

MOFs can act as heterogeneous catalysts using functional groups attached to the linkers or open metal sites generated within the framework upon activation. Their

high surface area offers a high density of active sites, and the tunability of the size and shape of their pores can impose restrictions upon the size or shape of reagent molecules. In this way, chiral MOF catalysts can promote asymmetric reactions, such as with enantiomeric zinc-based frameworks Zn-PYI1 and Zn-PYI2 (PYI = pyrrolidine-2-ylimidazole; Figure 1.5), where chiral organocatalysts coordinate to the metal sites and propagate into the framework pores. Both chiral frameworks catalyse the photo- $\alpha$ -alkylation of aldehydes in a 73-74 % yield, while the same reaction carried out in the presence of a non-chiral MOF and organocatalytic D-/L-PYI produced a similar yield of 62-67 %. An aldehyde larger than the Zn-PYI1/2 pores only gave a conversion of 7 %. In the case of phenylpropylaldehyde, Zn-PYI1 and Zn-PYI2 produced enantiomeric excesses (ee) of 92 % and 81 % respectively, far outperforming the control reaction (ee = 21-22 %) where the photocatalyst was present but the movement of the substrates within the pores was chirally unrestricted.<sup>20</sup>

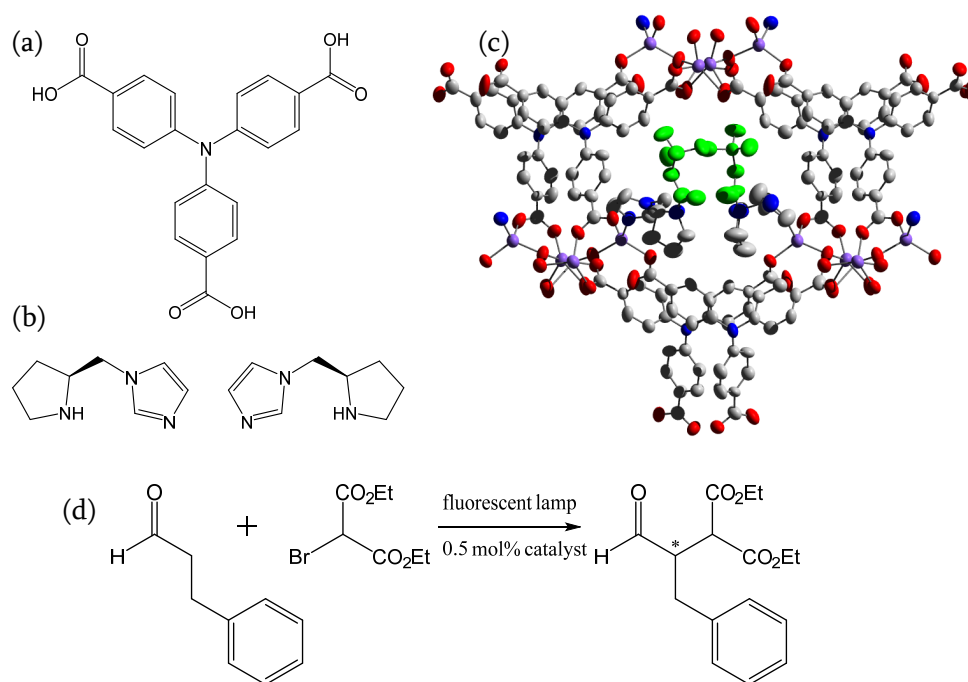


Figure 1.5: (a) Organic linker, 4,4',4''-tricarboxyltriphenylamine; (b) asymmetric organocatalytic groups, L- and D-pyrrolidine-2-ylimidazole; (c) crystal structure of Zn-PYI1, (zinc atoms shown in purple, oxygen in red, nitrogen in blue, carbon in grey, boc (*tert*-butylloxycarbonyl) protecting groups on the secondary amine shown in green); (d)  $\alpha$ -alkylation of phenylpropylaldehyde.

The use of MOFs as drug delivery agents is a more recent area of research that is beginning to attract interest in the biological community.<sup>21</sup> The high porosity of MOFs allows for a controlled release of drug molecules in a similar way to currently-used zeolites, but the presence of organic groups lining the pore walls increases the capacity for high drug loading. A chromium MOF, MIL-101, with two differently sized pores (29 and 34 Å), adsorbs approximately 1.4 g of ibuprofen per gram of dehydrated material, which is a significantly higher loading than in zeolite MCM-41 (MCM = mesoporous crystalline material) with similar pore sizes. Ibuprofen is released into simulated body fluid in three stages (Figure 1.6); the first stage, lasting approximately 8 hours, involves the release of physisorbed ibuprofen by diffusion. The second and third stages of release both involve the drug held close to the cage walls through cation-anion and  $\pi$ - $\pi$  interactions, with the ibuprofen held in the larger pores being released more quickly. Ibuprofen release from MIL-101 takes 6 days in total. This release profile is in contrast to that of the zeolite, MCM-41, and a different chromium-based MOF with smaller cages, MIL-100, which take a total of 2 and 3 days respectively. The longer, controlled delivery of drug molecules from MOFs is an advantage for improved control of drug administration.<sup>22</sup>

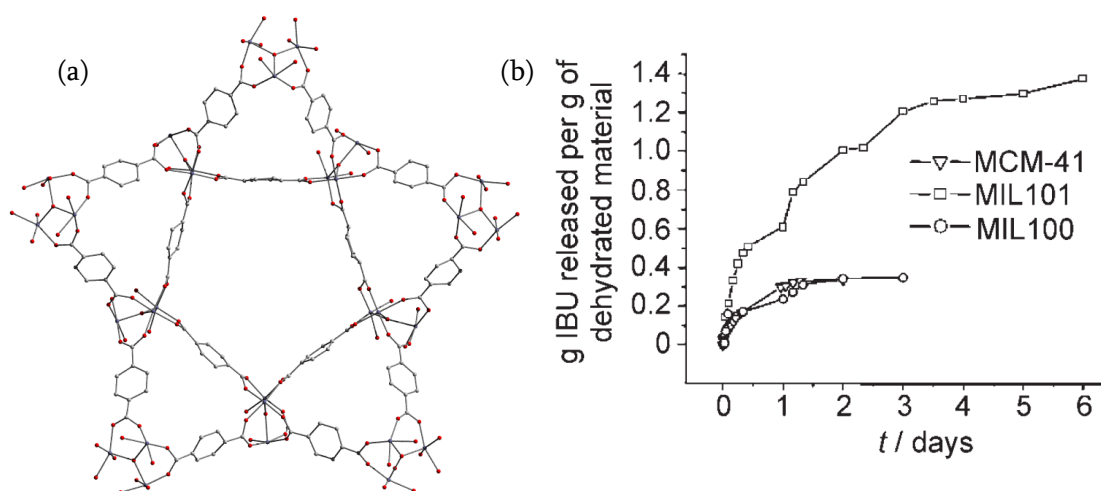


Figure 1.6: (a) View down the pentagonal opening of the smaller pore of MIL-101<sup>23</sup> (chromium atoms in purple, oxygen in red and carbon in grey; hydrogen atoms and water omitted for clarity); (b) ibuprofen delivery in simulated body fluid from MIL-100, MIL-101 and MCM-41, figure adapted from reference 23.

Biomedical imaging is also an emerging area of application-based MOF research. Some MOFs are active as magnetic resonance imaging (MRI) contrast agents. For many MRI scans, large doses of small molecules such as gadolinium-chelates are often used to enhance the contrast between normal and diseased tissue; the contrast agent's paramagnetic properties change the relaxation times of atoms within the tissue. However, the low retention time, low sensitivity and low selectivity of such Gd-complexes means high doses are required, making toxicity an issue. Nanoparticles of a Gd-containing MOF,  $\text{Gd}(\text{bhc})_{1.5}(\text{H}_2\text{O})_2$ , (bhc = benzene hexacarboxylic acid; Figure 1.7) show very high relaxivity values, lending them well to use as MRI contrast agents.<sup>24</sup> Increased nanoparticle size increases relaxivity values *in vivo*, and MOF nanoparticle size is tunable.<sup>25</sup> Moreover, the versatility of MOFs with functionalization of the linkers may allow nanoparticulate MOF contrast agents to be specifically targeted to certain regions of the body.

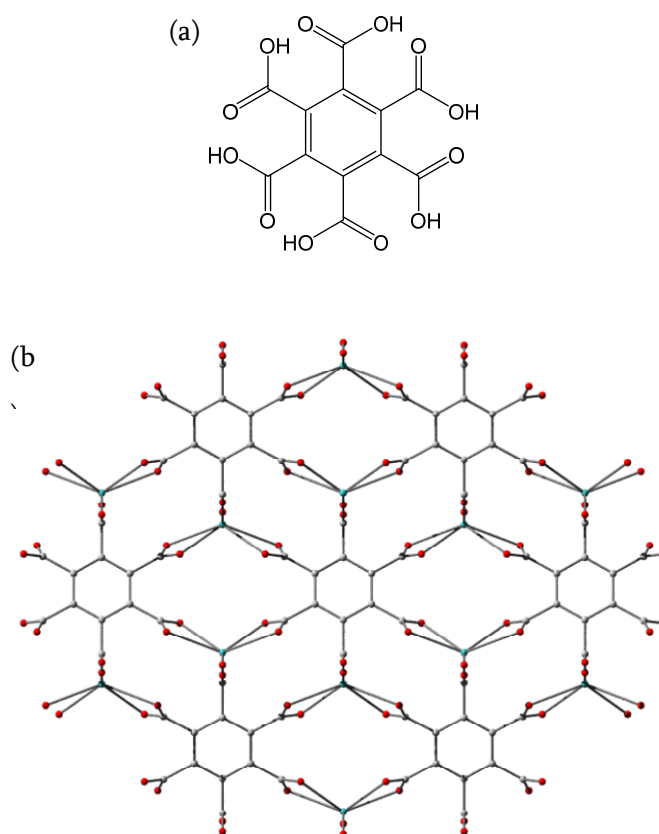


Figure 1.7: (a) Organic linker, benzene hexacarboxylic acid (bhc); (b) crystal structure<sup>26</sup> of  $\text{Gd}(\text{bhc})_{1.5}(\text{H}_2\text{O})_2$  (gadolinium atoms shown in turquoise, oxygen in red and carbon in grey; hydrogen atoms and coordinated water molecules omitted for clarity).

MOFs have been investigated for use in a wide range of electrochemical applications, from electrode materials for batteries to surface films to inhibit corrosion.<sup>27</sup> Most portable electronic devices use rechargeable lithium-ion batteries, where lithium ions in the cathode material migrate to the negative electrode and insert into the anode material on charge. The reverse process occurs on discharge. Novel electrode materials at both the anode and the cathode are required to improve the capacity of such rechargeable batteries, and the inherent tunability of MOFs may provide materials with improved properties. For example, an iron-based MOF,  $\text{Fe}^{\text{III}}(\text{OH})_{0.8}\text{F}_{0.2}(\text{bdc})\cdot\text{H}_2\text{O}$  (Figure 1.8), mixed with 15 wt% carbon was investigated for use as the positive electrode alongside lithium metal as the negative electrode. During charge, lithium ions insert into the anode material to form  $\text{Li}_{0.6}\text{Fe}^{\text{III}}(\text{OH})_{0.8}\text{F}_{0.2}(\text{bdc})\cdot\text{H}_2\text{O}$ . This new battery using a MOF-based positive electrode material has a capacity of  $75 \text{ mA h g}^{-1}$  (significantly lower than the current standard cathode material,  $\text{LiCoO}_2$ , at  $148 \text{ mA h g}^{-1}$ ) and Li-insertion is fully reversible for 50 cycles. Mössbauer spectroscopy reveals that, when the battery is fully charged and the MOF contains no lithium, all iron ions are high spin  $\text{Fe}^{\text{III}}$ . As discharge proceeds, an increasing amount of high spin  $\text{Fe}^{\text{II}}$  is observed and so a mixed valence material is present.<sup>28</sup>

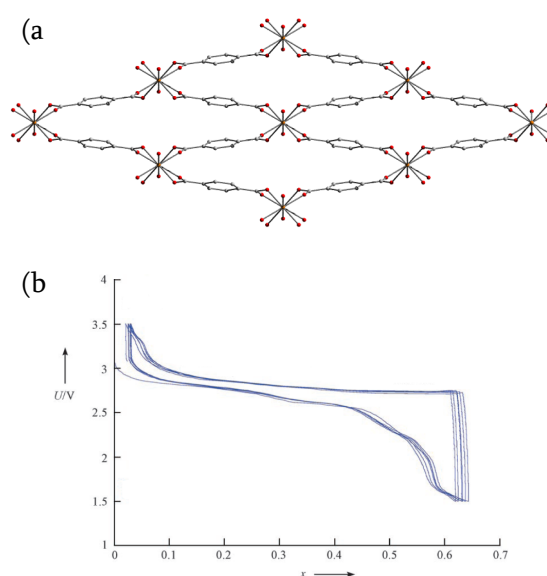


Figure 1.8: (a) Crystal structure of  $\text{Fe}^{\text{III}}(\text{OH})(\text{bdc})\cdot\text{H}_2\text{O}$  (iron atoms shown in orange, oxygen in red and carbon in grey; hydrogen atoms omitted for clarity); (b) voltage profile (adapted from reference 28) for a  $\text{Li}/[\text{Fe}^{\text{III}}(\text{OH})_{0.8}\text{F}_{0.2}(\text{bdc})\cdot\text{H}_2\text{O}]$  half-cell cycled between 1.5 and 3.5 V at a rate of one equivalent of Li in 40 h.

The luminescent properties of some MOFs along with their capacity to adsorb molecules within their pores have led to the investigation of MOFs as luminescent sensors. A cadmium-based MOF with carboxylate linkers (Figure 1.9) displays fluorescence at room temperature as an emulsion in many solvents due to the presence of  $d^{10}$  metal ions. As an emulsion in acetone, however, luminescence is entirely quenched. Increasing amounts of acetone in a 1-propanol emulsion produce a first-order exponential decay in fluorescence intensity, indicating that the quenching process is diffusion-controlled. In the presence of acetone, the energy absorbed by the organic linkers within the MOF is transferred to the acetone molecules, reducing the luminescence intensity. This quantitative relationship between acetone concentration and fluorescence intensity indicates that such MOFs show potential for the selective sensing of acetone through fluorescence quenching. A detection system for volatile organic solvent molecules such as acetone is valuable in the protection of the environment, and fluorescent sensors such as this provide short response times and good sensitivity at a low cost.<sup>29</sup>

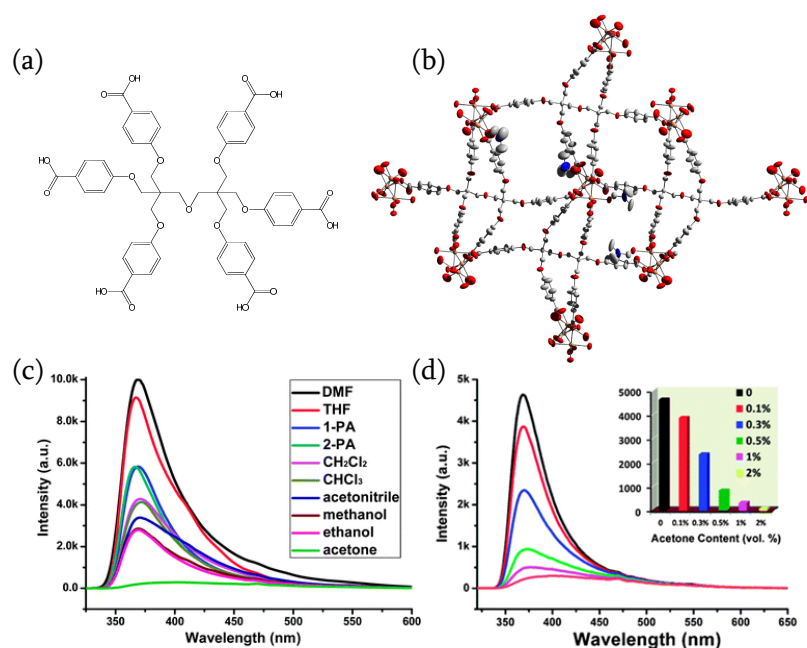


Figure 1.9: (a) Organic linker, hexa[4-(carboxyphenyl)oxamethyl]-3]oxapentane acid (COA); (b)  $\text{Cd}_3(\text{COA})(\text{H}_2\text{O})_2(\text{DMF})_2 \cdot 5\text{H}_2\text{O}$  viewed down the *b*-axis (DMF = dimethylformamide; cadmium atoms shown in peach, oxygen in red, nitrogen in blue and carbon in grey; non-coordinated DMF molecules and hydrogen atoms omitted for clarity); (c) fluorescence shown in pure solvents; (d) fluorescence shown in 1-propanol with varying amounts of acetone (images (c) and (d) adapted from reference 29).

## **1.3 MOFs for hydrocarbon separations**

### **1.3.1 Olefin/paraffin separation**

Olefins and paraffins with carbon chains of similar length exhibit similar properties, so their separation is challenging. Industrial separation of such mixtures is highly important in the petrochemical industry, but currently energy-intensive cryogenic distillation is used at great expense.<sup>30</sup>

Adsorptive separation would be a more energy efficient option, but conventional adsorbents such as activated carbon and porous silica show poor selectivity. Zeolites have been investigated for olefin/paraffin separations, but few have shown potential; ITQ-32 (ITQ = Instituto de Tecnologia Quimica), a pure silica zeolite, showed high selectivity for 1-butene over butane suggesting good separation capacity, but it was not selective for 2-butene adsorption, thus preventing the removal of butenes from mixtures with butane. Moreover, adsorption of 1-butene was too slow for feasible industrial separations.<sup>31</sup> Feedstock compositions are frequently unpredictable and contaminants often negatively impact new technologies to such an extent that the pre-treatment processes required for their removal outweigh the benefits afforded by avoiding cryogenic separation.<sup>30</sup>

Some MOF-based adsorptive olefin/paraffin separations based upon the preferential adsorption of the olefin component have been reported. HKUST-1 (HKUST = Hong Kong University of Science and Technology), for example, selectively adsorbs ethylene over ethane due to interactions between the ethylene  $\pi$ -bonds and the partial positive charges on the framework's copper atoms.<sup>32</sup> The propylene adsorption capacity of HKUST-1 is approximately three times higher than carbon molecular sieves and 13X zeolite, and at pressures above 50 kPa propylene adsorption is greater than both propane and isobutane. Calculated Henry's constants for these three gases indicate that HKUST-1 has a higher affinity for propylene than propane and isobutane due to interactions between the olefin  $\pi$ -orbitals and the unsaturated copper sites.<sup>33</sup> Binary breakthrough curves of a 26 % propane/ 74 % propylene mixture over HKUST-1 at 373 K and 150 kPa confirm that the separation of

such a mixture is possible using the HKUST-1 framework, with propane being output after 800 s and propylene being detected 50 s later.<sup>34</sup>

Adsorption isotherms for ethane, propane, ethylene and propylene on Mg-CPO-27 (CPO = coordination polymer, Oslo) indicate that propylene adsorbs to vacant magnesium sites most strongly while the framework's affinity for both alkanes was significantly lower than for the olefins (Table 1.3). The stronger interaction with olefins is, as with HKUST-1, due to the interaction between olefin  $\pi$ -orbitals and unsaturated metal sites.  $C_3$  hydrocarbons adsorb more strongly than their  $C_2$  counterparts because of the presence of significant dipole moments in the longer molecules.<sup>35</sup>

Table 1.3: Heats of adsorption at zero coverage of  $C_2$  and  $C_3$  alkanes and olefins on Mg-CPO-27.

Adsorbate	Heat of adsorption at zero coverage / $\text{kJ mol}^{-1}$
Ethane	35.4
Ethylene	42.6
Propane	33.9
Propylene	60.5

Kinetic separation of propane/propylene mixtures is likely to be possible using ZIF-8, a zinc-based framework. ZIF-8, containing 2-methylimidazole ligands and pore openings of 3.26 Å, has identical adsorption capacities for propane and propylene at 30 °C and 600 torr and identical isosteric heats of adsorption at zero coverage. The rates of adsorption of each  $C_3$  gas are, however, very different (Figure 1.10); the ratio of the diffusion rate constants,  $D(C_{\text{propane}})/D(C_{\text{propylene}})$ , is 125. An isostructural MOF with 2-chloroimidazole ligands and pore openings of 3.37 Å displays similar properties, but the ratio of the diffusion rate constants is only 60. Evidently the very small difference in pore size greatly affects the selectivity of the framework, so the selectivity of the adsorption process is based upon molecule size. The energy barriers

for adsorption of similarly sized propane and propylene are very different, with the activation energy for adsorption on ZIF-8 measuring  $74.1 \text{ kJ mol}^{-1}$  for propane and  $9.7 \text{ kJ mol}^{-1}$  for propylene.<sup>36</sup>

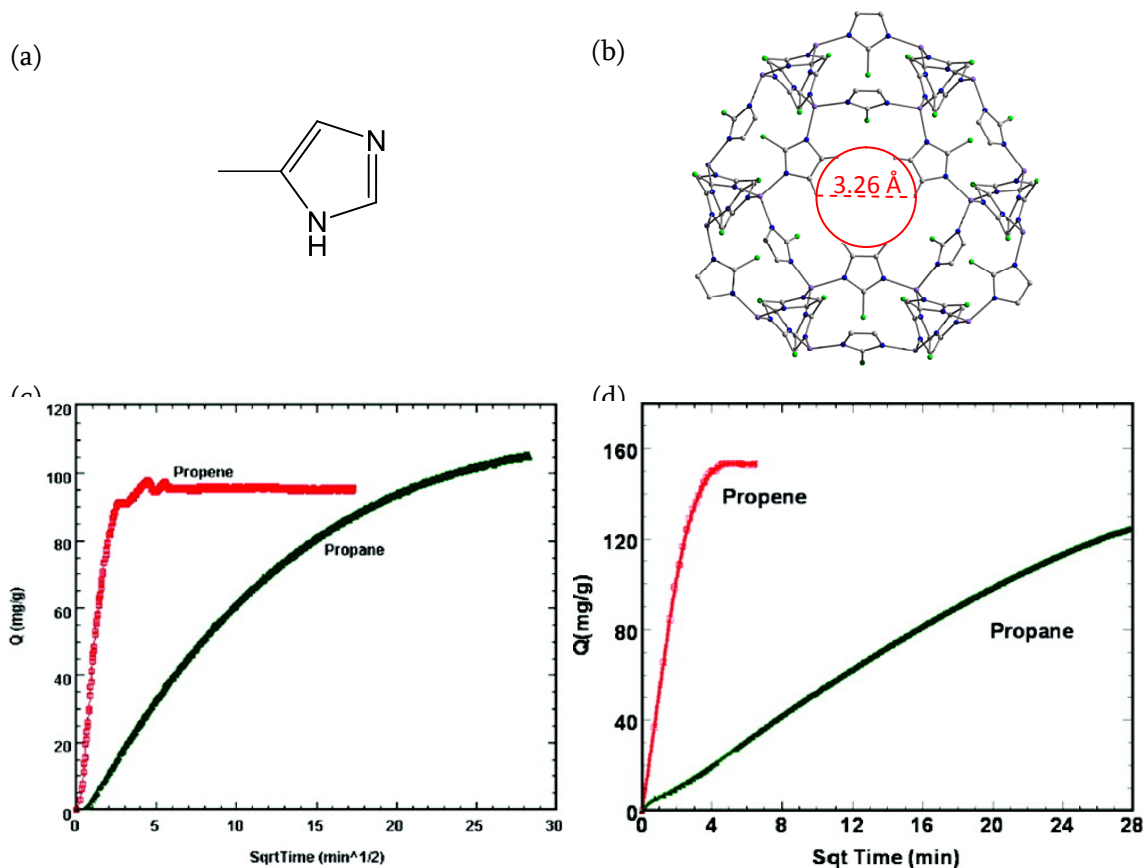


Figure 1.10: (a) 2-Methylimidazole; (b) ZIF-8<sup>37</sup> viewed down the (0.5,0.5,0.5) axis (zinc atoms shown in purple, oxygen in red, carbon in grey, methyl groups shown in green, hydrogen atoms protruding into the pore opening displayed but others omitted for clarity. Red circle indicates the pore opening); (c) propane and propylene uptake by ZIF-8; (d) propane and propylene uptake by the chloro-analogue of ZIF-8; (c) and (d) adapted from reference 36.

### 1.3.2 Ethylene/acetylene separation

Steam cracking, where saturated hydrocarbons are converted into lighter olefins, is commonly used in industry to produce ethylene from ethane. Typically, though, the ethylene product contains approximately 1 % acetylene. The Ziegler-Natta catalysts used in ethylene polymerization are poisoned by the presence of ppm levels of

acetylene in the ethylene feed, lowering the quality of polymer products as well as slowing down their synthesis.<sup>38</sup>

The separation of ethylene and acetylene is, therefore, an important industrial process and two different methods are commonly used. Noble metal catalysts, such as supported palladium, are used to partially hydrogenate acetylene into ethylene. Such catalysts are expensive, however, and the overhydrogenation of olefins into paraffins is an undesired side effect.<sup>38</sup> Alternatively, organic solvents such as DMF can be used to extract the cracked olefins leaving pure acetylene behind,<sup>39</sup> but the significant loss of solvent experienced after multiple operations makes this solvent extraction process less than ideal.<sup>40</sup> More recent, non-absorptive, attempts to separate ethylene and acetylene have involved hydrogenation by non-precious metal catalysts such as nickel-zinc alloys,<sup>41</sup>  $\pi$ -complexation<sup>11</sup> and ionic liquid extraction<sup>42</sup>.

Size-selective adsorption of acetylene onto a Zn/Cu-based mixed metal-organic framework (MMOF) occurs due to thermodynamically and kinetically controlled framework flexibility. Two similar MOFs were produced, one containing 1,4-benzenedicarboxylate (BDC) ligands and the other containing 1,4-cyclohexanedicarboxylate (CDC) ligands. Both ethylene and acetylene have full access to the pores of the BDC framework at 195 K and so acetylene/ethylene selectivity is only 1.6. The CDC framework, however, shows an acetylene/ethylene selectivity of 25.5 at 195 K and 1 atm due to the different degree of access to the framework pores. The isosteric heat of adsorption at zero coverage is approximately equal for each gas, so the separation capacity cannot be due to interactions with the pore surfaces. Instead, the larger CDC linker produces narrower pore openings which favour size-specific separation of ethylene and acetylene; acetylene fully enters the micropores at 195 K while ethylene is either blocked or only very slowly adsorbed. The separation process is temperature dependent due to the expansion of the pore openings at higher temperature, as although adsorption of acetylene over ethylene is still favoured at 295 K, the selectivity is only 5.2.<sup>40</sup>

### 1.3.3 Olefin separation

A zinc-based MOF, MAMS-2 (MAMS = mesh adjustable molecular sieve), with hydrophobic and hydrophilic pores was constructed with *tert*-butyl groups pointing into the hydrophobic pores (Figure 1.11). The *tert*-butyl groups act as a gate, only allowing molecules of certain sizes into the hydrophobic pores. The interaction between these *tert*-butyl groups is reduced at higher temperatures, causing the gate to open wider and allow the passage of larger molecules. The relationship between temperature and pore opening is linearly related, so the size of the pore opening can be adjusted as desired within the range of 2.9 to 4.6 Å. Propylene, with a kinetic diameter of 4.5 Å, adsorbs into the hydrophobic pores at 231 K, and optimal ethylene/propylene separation occurs at 195 K where propylene is prevented from entering the pores.<sup>43</sup>

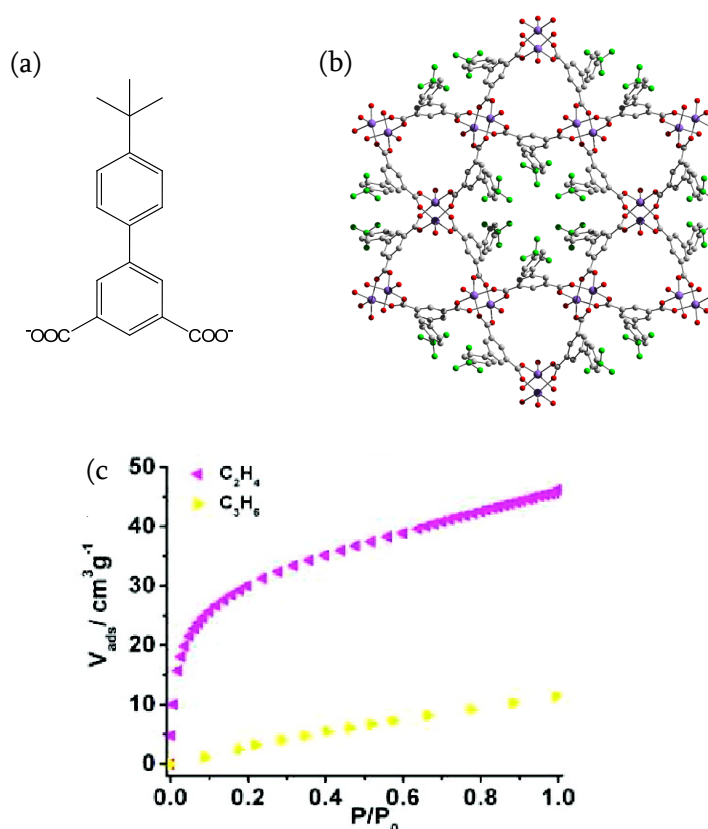


Figure 1.11: (a) 4'-*tert*-Butyl-biphenyl-3,5-dicarboxylate (BBPDC) linker; (b) crystal structure of MAMS-2 (oxygen shown in red, carbon in grey, *tert*-butyl groups in the hydrophobic pores are coloured green and hydrogen atoms are omitted for clarity); (c) ethylene and propylene adsorption isotherms at 195 K (adapted from reference 43).

## 1.4 References

1. *Oil refining and refineries / What we do / BP*.  
<http://www.bp.com/sectiongenericarticle.do?categoryId=9021510&contentId=7040010> (accessed 29/11/2012).
2. C. Driussi and J. Jansz, *J. Cleaner Prod.*, 2006, **14**, 682–688.
3. D. Farrusseng, *Metal-Organic Frameworks Applications from Catalysis to Gas Storage.*, John Wiley & Sons, Weinheim, 2011.
4. J.-R. Li, J. Sculley, and H.-C. Zhou, *Chem. Rev.*, 2012, **112**, 869–932.
5. D. Leckel, *Energy Fuels*, 2009, **23**, 2342–2358.
6. Sasol Facts 2011: Our Products.  
[http://sasol.investoreports.com/sasol\\_sf\\_2011/our-products/introduction](http://sasol.investoreports.com/sasol_sf_2011/our-products/introduction)  
(accessed 06/12/2012).
7. O. R. Inderwildi, S. J. Jenkins, and D. A. King, *Angew. Chem. Int. Ed.*, 2008, **47**, 5253–5255.
8. H. Schulz, *Appl. Catal., A*, 1999, **186**, 3–12.
9. D. R. Lide, *CRC handbook of chemistry and physics : 2008-2009*, CRC Press, Boca Raton; London; New York, 89th edn., 2008.
10. R. S. Andre (Air Products and Chemicals Inc, USA). Method and apparatus for olefinic separation. US Patent 0326946, January 26, 1989.
11. K. Wang, *Science*, 2001, **291**, 106–109.
12. A. de Klerk, *Ind. Eng. Chem. Res.*, 2004, **43**, 6349–6354.
13. S. R. Batten, N. R. Champness, X.-M. Chen, J. Garcia-Martinez, S. Kitagawa, L. Öhrström, M. O’Keeffe, M. P. Suh, and J. Reedijk, *IUPAC Provisional Recommendation*, 2012.
14. A. D. Burrows, M. F. Mahon, C. L. Renouf, C. Richardson, A. J. Warren, and J. E. Warren, *Dalton Trans.*, 2012, **41**, 4153.
15. M. Eddaoudi, J. Kim, N. Rosi, D. Vodak, J. Wachter, M. O’Keeffe, and O. M. Yaghi, *Science*, 2002, **295**, 469–472.
16. U. Mueller, M. Schubert, F. Teich, H. Puetter, K. Schierle-Arndt, and J. Pastré, *J. Mater. Chem.*, 2006, **16**, 626.
17. R. Banerjee, H. Furukawa, D. Britt, C. Knobler, M. O’Keeffe, and O. M. Yaghi, *J. Am. Chem. Soc.*, 2009, **131**, 3875–3877.
18. L. Hamon, C. Serre, T. Devic, T. Loiseau, F. Millange, G. Férey, and G. D. Weireld, *J. Am. Chem. Soc.*, 2009, **131**, 8775–8777.
19. K. Barthelet, J. Marrot, D. Riou, and G. Férey, *Angew. Chem. Int. Ed.*, 2002, **41**, 281–284.
20. P. Wu, C. He, J. Wang, X. Peng, X. Li, Y. An, and C. Duan, *J. Am. Chem. Soc.*, 2012, **134**, 14991–14999.

21. R. C. Huxford, J. Della Rocca, and W. Lin, *Curr. Opin. Chem. Biol.*, 2010, **14**, 262–268.
22. P. Horcajada, C. Serre, M. Vallet-Regí, M. Sebban, F. Taulelle, and G. Férey, *Angew. Chem. Int. Ed.*, 2006, **45**, 5974–5978.
23. G. Férey, C. Mellot-Draznieks, C. Serre, J. Dutour, S. Surblé, and I. Margiolaki, *Science*, 2005, **309**, 2040–2042.
24. K. M. L. Taylor, A. Jin, and W. Lin, *Angew. Chem. Int. Ed.*, 2008, **47**, 7722–7725.
25. W. Hatakeyama, T. J. Sanchez, M. D. Rowe, N. J. Serkova, M. W. Liberatore, and S. G. Boyes, *ACS Applied Materials & Interfaces*, 2011, **3**, 1502–1510.
26. S. S.-Y. Chui, A. Siu, X. Feng, Z. Ying Zhang, T. C. W. Mak, and I. D. Williams, *Inorg. Chem. Commun.*, 2001, **4**, 467–470.
27. A. Morozan and F. Jaouen, *Energy & Environmental Science*, 2012, **5**, 9269.
28. G. Férey, F. Millange, M. Morcrette, C. Serre, M.-L. Doublet, J.-M. Greneche, and J.-M. Tarascon, *Angew. Chem. Int. Ed.*, 2007, **46**, 3259–3263.
29. F.-Y. Yi, W. Yang, and Z.-M. Sun, *J. Mater. Chem.*, 2012, **22**, 23201.
30. R. B. Eldridge, *Ind. Eng. Chem. Res.*, 1993, **32**, 2208–2212.
31. M. Palomino, A. Cantín, A. Corma, S. Leiva, F. Rey, and S. Valencia, *Chem. Commun.*, 2007, 1233.
32. Q. Min Wang, D. Shen, M. Bülow, M. L. Lau, S. Deng, F. R. Fitch, N. O. Lemcoff, and J. Semanscin, *Microporous Mesoporous Mater.*, 2002, **55**, 217–230.
33. N. Lamia, M. Jorge, M. A. Granato, F. A. Almeida Paz, H. Chevreau, and A. E. Rodrigues, *Chem. Eng. Sci.*, 2009, **64**, 3246–3259.
34. M. G. Plaza, A. F. P. Ferreira, J. C. Santos, A. M. Ribeiro, U. Müller, N. Trukhan, J. M. Loureiro, and A. E. Rodrigues, *Microporous Mesoporous Mater.*, 2012, **157**, 101–111.
35. Z. Bao, S. Alnemrat, L. Yu, I. Vasiliev, Q. Ren, X. Lu, and S. Deng, *Langmuir*, 2011, **27**, 13554–13562.
36. K. Li, D. H. Olson, J. Seidel, T. J. Emge, H. Gong, H. Zeng, and J. Li, *J. Am. Chem. Soc.*, 2009, **131**, 10368–10369.
37. K. S. Park, Z. Ni, A. P. Côté, J. Y. Choi, R. Huang, F. J. Uribe-Romo, H. K. Chae, M. O’Keeffe, and O. M. Yaghi, *Proceedings of the National Academy of Sciences*, 2006, **103**, 10186–10191.
38. W. Huang, J. R. McCormick, R. F. Lobo, and J. G. Chen, *J. Catal.*, 2007, **246**, 40–51.
39. K. Weissrnel, *Industrial organic chemistry*, VCH, Weinheim ; New York, 3rd edn., 1997.

40. S.-C. Xiang, Z. Zhang, C.-G. Zhao, K. Hong, X. Zhao, D.-R. Ding, M.-H. Xie, C.-D. Wu, M. C. Das, R. Gill, K. M. Thomas, and B. Chen, *Nat. Commun.*, 2011, **2**, 204.
41. F. Studt, F. Abild-Pedersen, T. Bligaard, R. Z. Sorensen, C. H. Christensen, and J. K. Norskov, *Science*, 2008, **320**, 1320–1322.
42. J. Palgunadi, H. S. Kim, J. M. Lee, and S. Jung, *Chem. Eng. Process.: Process Intensification*, 2010, **49**, 192–198.
43. S. Ma, D. Sun, D. Yuan, X.-S. Wang, and H.-C. Zhou, *J. Am. Chem. Soc.*, 2009, **131**, 6445–6451.

## CHAPTER 2: Aims

The overall aim of this thesis is to assess the capacity of metal organic frameworks with open metal sites for the separation of olefin mixtures.

Adsorption and desorption isotherms for ethylene and propylene will be obtained using different MOFs with open metal sites. The isotherms will be used to calculate the isosteric enthalpies of adsorption at varying coverages.

Ideal adsorbed solution theory will be applied to the experimental adsorption isotherms to evaluate the selectivity of the different MOFs for propylene/ethylene mixtures. The predicted selectivities will be used to suggest whether separation of propylene/ethylene mixtures is possible, and which framework would be most suited to this application. Temperature programmed desorption will also be carried out with ethylene on the different frameworks, allowing the calculation of the enthalpies of desorption. The TPD results will suggest the temperature at which regeneration of the framework would be possible after a separation procedure.

In order to fully understand the adsorption of olefins onto MOFs, structural studies will be undertaken. An *in situ* environmental gas cell for single crystal X-ray diffraction will be developed to allow the study of frameworks under controllable gaseous environments. The dehydration procedure of one MOF will be examined in detail. NO adsorption and release will be carried out within the gas cell to assess its potential for prolonged experiments, exposing a single crystal to multiple different environments. Subsequently, MOF single crystals will be exposed to ethylene and propylene within the gas cell to investigate where in the framework olefins bind.

## CHAPTER 3: Experimental techniques

### 3.1 Gas adsorption

#### 3.1.1 Langmuir theory<sup>1,2</sup>

Langmuir's theory of gas adsorption, as developed in 1916 by Irving Langmuir<sup>3</sup>, is based upon a number of assumptions: only a monolayer of gas is adsorbed, all adsorption sites are equivalent throughout a uniform surface, and there are no interactions between the adsorbed molecules.

Adsorption is treated as an equilibrium where a gaseous molecule,  $A$ , reacts with a vacant site on the surface,  $S$ , to yield an adsorbed complex,  $AS$  (3.1).



This dynamic equilibrium can be expressed by kinetic theory (3.2) where  $\mu$  represents the rate at which gaseous molecules strike the surface,  $m$  is the mass of a gaseous molecule,  $k$  is Boltzmann's constant and  $T$  is the temperature.

$$\mu = \frac{P}{(2\pi mkT)^{1/2}} \quad (3.2)$$

If  $\theta$  is the fractional coverage of the surface,  $\alpha$  is the ratio of molecules that adsorb when they strike the surface and  $\nu$  is the rate of evaporation from a monolayer, the number of molecules adsorbed at equilibrium is:

$$\alpha\mu(1 - \theta) = \nu\theta \quad (3.3)$$

A constant,  $b$ , can be defined:

$$b = \frac{\alpha}{\nu(2\pi mkT)^{1/2}} \quad (3.4)$$

By combining equations (3.2) and (3.3), and introducing constant  $b$ , the Langmuir equation can be derived (3.5).

$$\theta = \frac{bP}{1 + bP} \quad (3.5)$$

If  $V$  is the volume adsorbed at pressure  $P$ , and  $V_m$  is the volume of gas adsorbed to create a complete monolayer, this can be written instead as:

$$V = \frac{V_m P}{1 + bP} \quad (3.6)$$

which can be rearranged to form (3.7).

$$\frac{P}{V} = \frac{P}{V_m} + \frac{1}{bV_m} \quad (3.7)$$

If the assumptions made by Langmuir theory adequately describe a system, a plot of  $\frac{P}{V}$  versus  $P$  produces a straight line with gradient  $\frac{1}{V_m}$  and  $y$ -intercept  $\frac{1}{bV_m}$ .

The surface area occupied by 1 g of adsorbate,  $s$ , can be calculated from  $V_m$ , where  $\sigma$  is the surface area of a single adsorbed gas molecule,  $m$  is the mass of the sample,  $N_A$  is Avogadro's constant and  $V_0$  is the volume of one mole of gas at standard temperature and pressure (3.8).

$$s = \frac{V_m \sigma N_A}{mV_0} \quad (3.8)$$

### 3.1.2 BET theory<sup>1,2</sup>

In 1938 Brunauer, Emmett and Teller developed an extension to Langmuir's theory of adsorption in an attempt to describe multilayer adsorption.<sup>4</sup> As before, a number of assumptions must be made: gas molecules adsorb onto a surface in an infinite number of layers, there is no interaction between the molecules in each layer and all Langmuir assumptions apply to each individual layer.

Multilayer adsorption can be treated as a dynamic equilibrium. As with Langmuir theory, the rate of adsorption of gas molecules onto the bare surface is equal to the rate of desorption from the first layer. This can be expressed mathematically

(3.9), where  $a_1$  and  $b_1$  are constants,  $E_1$  is the heat of adsorption of the first layer and  $s_0$  and  $s_1$  are the surface areas covered by gas molecules.

$$a_1 P s_0 = b_1 s_1 e^{\frac{-E_1}{RT}} \quad (3.9)$$

The same treatment can be applied to the second layer, where the rate of adsorption of gas molecules onto the first layer is equal to the rate of desorption from the second layer (3.10).

$$a_2 P s_1 = b_2 s_2 e^{\frac{-E_2}{RT}} \quad (3.10)$$

By applying this to every layer, a general equation can be obtained (3.11).

$$a_i P s_{i-1} = b_i s_i e^{\frac{-E_i}{RT}} \quad (3.11)$$

The total surface area available for adsorption,  $A$ , and the total volume of gas adsorbed are expressed in (3.12) and (3.13) respectively, where  $V_{sat}$  is the volume of gas adsorbed per unit area when the monolayer is saturated.

$$A = \sum_{i=0}^{i=\infty} s_i \quad (3.12)$$

$$V = V_{sat} \sum_{i=0}^{i=\infty} i s_i \quad (3.13)$$

Combining these two equations gives (3.14).

$$\frac{V}{AV_{sat}} = \frac{V}{V_m} = \frac{\sum_{i=0}^{i=\infty} i s_i}{\sum_{i=0}^{i=\infty} s_i} \quad (3.14)$$

Using the assumption that the adsorption and desorption properties of each layer are the same as those of the first layer, the BET equation can be derived (3.15).  $P_0$  is the saturation pressure of the gas,  $V_a$  is the volume of gas adsorbed at a given pressure,  $P$ , and  $C$  is a constant, as described in (3.16) where  $E_L$  is the heat of liquefaction of the gas.

$$V_a = \frac{V_m CP}{(P_0 - P) \left[ 1 + (C - 1) \frac{P}{P_0} \right]} \quad (3.15)$$

$$C \propto e^{\frac{E_1 - E_L}{RT}} \quad (3.16)$$

Equation (3.15) can be rearranged to form the linear equation (3.17).

$$\frac{P}{V_a(P_0 - P)} = \frac{1}{V_m C} + \frac{C - 1}{V_m C} \left( \frac{P}{P_0} \right) \quad (3.17)$$

If BET theory applies satisfactorily to the experimental data, a plot of  $\frac{P}{V_a(P_0 - P)}$  versus  $\frac{P}{P_0}$  will yield a straight line where the gradient is equal to  $\frac{(C - 1)}{V_m C}$  and the intercept is equal to  $\frac{1}{V_m C}$ .

The mean area occupied by one adsorbed gaseous molecule,  $\sigma$ , can be calculated from the molecular weight of the gas,  $M$ , and the density of the liquefied gas,  $\rho$  (3.18). This, along with  $V_m$  as calculated from (3.17), allows the determination of the surface area of the sample.

$$\sigma = (4)(0.866) \left[ \frac{M}{4(2N_A \rho)^{1/2}} \right]^{2/3} \quad (3.18)$$

### 3.1.3 Chemisorption and physisorption<sup>2,5</sup>

Adsorption of a gas onto a surface can be classified into two distinct types: chemical adsorption, or chemisorption, and physical adsorption, or physisorption.

Physisorption occurs when van der Waals attractions take place between the gas molecules and the adsorbent surface. Induced dipole moments cause the molecules to interact and the gas molecules to adsorb with a heat of adsorption of the same order of magnitude as the heat of gas vapourisation (for N<sub>2</sub>,  $\Delta_{vap} H$  at normal boiling point is 5.57 kJ mol<sup>-1</sup>)<sup>6</sup>. Adsorption is fast since gas molecules are adsorbed at the same speed at which they reach the surface and the adsorption isotherm can

indicate monolayer or multilayer adsorption. Physisorbed gases can be removed by reducing the pressure of the system to below that at which the gas was adsorbed.

Chemisorption occurs when electrons are transferred between the gas and the adsorbent involving the formation of a chemical bond. The heat of adsorption in such a case is usually similar in magnitude to the heat of chemical reactions; the standard enthalpy change for hydrogenation of ethylene at 298 K, for example, is  $-136.3 \text{ kJ mol}^{-1}$ .<sup>7</sup> Adsorption may or may not be rapid, since an energy of activation must be overcome for the adsorption process to occur. Adsorption isotherms always indicate monolayer chemisorption to the surface of the adsorbent. Simply reducing the pressure of the gas will not remove a chemisorbed species; intense heat or an alternative chemisorption process is usually required instead.

Chemisorption can occur in two ways: non-dissociative and dissociative (Figure 3.1). Non-dissociative chemisorption describes the process where a molecule forms a chemical bond to the surface while remaining intact. Initially, as the molecule approaches the surface it experiences van der Waals interactions and physisorbs to the surface, occupying the physisorption minimum in the potential energy curve in Figure 3.2(a). The physisorption minimum is at a distance equal to the sum of the van der Waals radii of the surface atom and the adsorbate molecule. This state is short lived, as the molecule passes over a small activation barrier to reach the chemisorption minimum. Dissociative chemisorption, on the other hand, describes the process where a molecule breaks up as it is adsorbed to produce two separate adsorbed species. This can be either non-activated, which is energetically favourable, or activated, where additional energy is required to cause dissociation. In the activated dissociative chemisorption potential energy curve shown in Figure 3.2(b), the approaching molecule interacts with the surface as before to form a physisorbed species due to van der Waals interactions. An activation energy,  $E_a$ , must be supplied to cause the molecule to overcome the activation barrier, at which point the molecule dissociates to form two chemisorbed species in the chemisorption minimum. Desorption of the species requires a large energy input in order to overcome  $\Delta H_{ads}$  and  $D$ , the energy of dissociation. Non-activated dissociative chemisorption is similar, except that the point at which the physisorption and

chemisorption curves cross lies below zero, so there is no activation energy to be overcome.

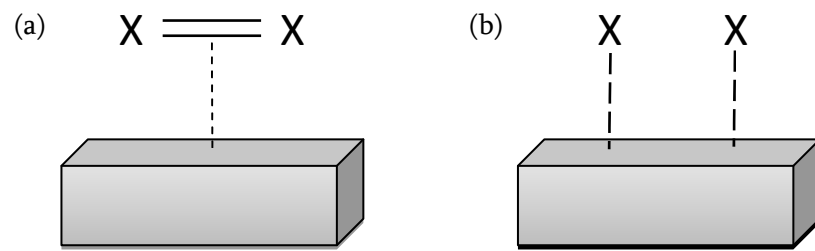


Figure 3.1: Diagrams showing a diatomic molecule,  $X_2$ , chemisorbed onto a surface. (a) Non-dissociative chemisorption, (b) dissociative chemisorption.

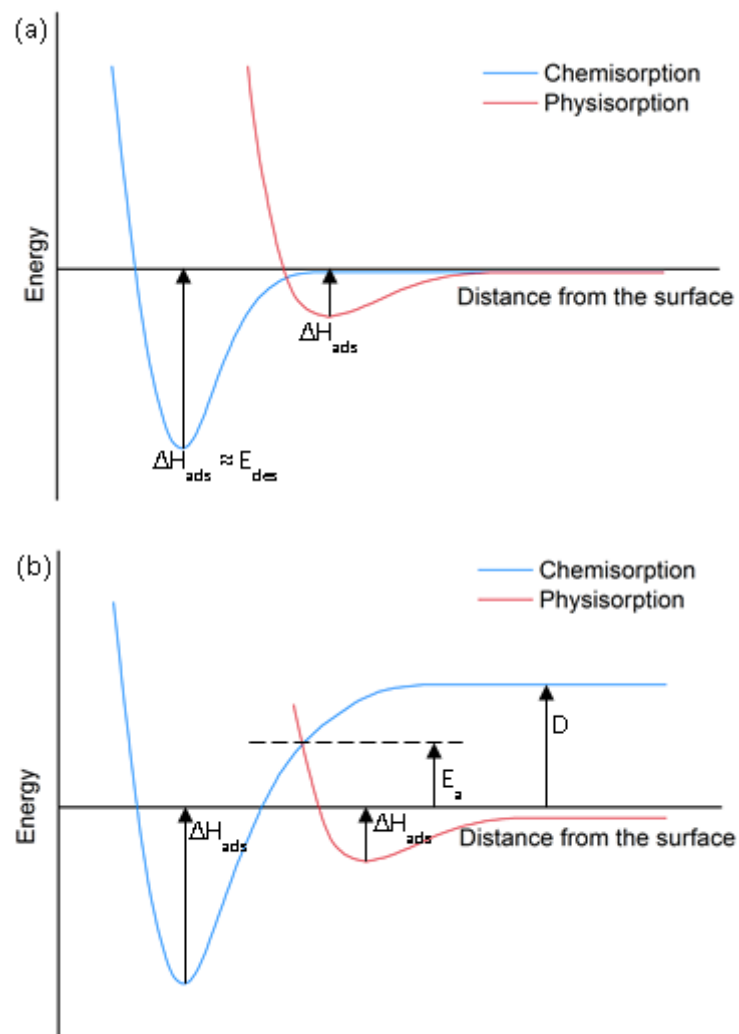


Figure 3.2: Potential energy curves for (a) non-dissociative chemisorption and (b) activated dissociative chemisorption.

### 3.1.4 Enthalpy of adsorption

A virial thermal adsorption equation can be used to describe the effect of temperature and pressure on surface coverage. The use of this equation allows the isosteric heat of adsorption to be calculated from adsorption isotherms performed over a range of temperatures, independent of any isotherm model.

The virial equation (3.19) for gas adsorption onto a solid support applies at fixed temperature, where  $n$  is the amount adsorbed,  $P$  is the pressure in Pa and  $A_i$  are virial coefficients.<sup>8</sup>

$$\ln\left(\frac{n}{P}\right) = A_0 + A_1n + A_2n^2 + A_3n^3 + \dots \quad (3.19)$$

Most gas adsorption processes can be adequately described using just two virial coefficients,  $A_0$  and  $A_1$ , and so the equation can be simplified to (3.20).

$$\ln\left(\frac{n}{P}\right) = A_0 + A_1n \quad (3.20)$$

Although this equation was derived empirically,  $A_0$  and  $A_1$  have physical meaning.  $A_0$  is related to adsorbate-adsorbent interactions and can be used to calculate the heat of adsorption at zero coverage for the system being studied.  $A_1$  is related to the adsorbate-adsorbate interactions.<sup>9</sup> By plotting the data at each temperature using equation (3.20), values for  $A_0$  and  $A_1$  can be calculated.  $A_0$  is related to Henry's law constant,  $K_H$ , by equation (3.21); Henry's law states that, in the low pressure region of an adsorption isotherm, surface coverage is proportional to pressure.<sup>10</sup>

$$K_H = \exp(A_0) \quad (3.21)$$

Isosteric heats of adsorption can be calculated at different surface coverages using equation (3.22), where  $Q$  is the integral heat of adsorption,  $c_G$  is the molar heat capacity of the gas phase at constant pressure and  $c_s$  is the molar heat capacity of the adsorbed phase.

$$\frac{dQ}{dT} = n(c_G - c_S) \quad (3.22)$$

At zero coverage, the isosteric heat of adsorption ( $q_{st}$ ) can be calculated using the  $A_0$  virial parameters obtained from equation (3.20); the gradient of an  $A_0$  vs.  $1/T$  plot is equal to  $-q_{st}/R$ .<sup>11</sup>

The heat of adsorption at varying coverages can be calculated using the Clausius-Clapeyron equation (3.23), which describes the relationship between the temperature of a liquid and its enthalpy of vaporisation. Integration of equation (3.23) provides equation (3.24), where  $c$  is a constant and  $q_{ST}$  is equal to  $-\Delta H_{vap}$ . Plots of  $1/T$  vs.  $\ln P$  at specific coverages give straight lines, and their gradients provide enthalpies of adsorption at specific coverages.

$$\frac{d \ln P}{dT} = \frac{\Delta H_{vap}}{RT^2} \quad (3.23)$$

$$\ln P = \frac{q_{ST}}{RT} + c \quad (3.24)$$

### 3.1.5 Gravimetric adsorption

Gas being adsorbed onto the surface of a sample corresponds to a small mass increase, and gravimetric adsorption apparatus can measure this mass increase using a highly sensitive microbalance.

#### 3.1.5.1 Experimental<sup>12</sup>

A CI Microbalance with a sensitivity of 0.1  $\mu\text{g}$  and a reproducibility of 0.01 % of the load was enclosed within home-built apparatus (Figure 3.3). Above room temperature, the sample environment and counterbalance were kept at equal and constant temperatures using a circulation water bath to minimise the effect of temperature differences from the external environment, but for experiments carried out below room temperature the counterbalance was kept at room temperature. The pressure inside the system was monitored using two BOC active gauges with ranges of  $1 \times 10^{-8}$  to  $1 \times 10^{-2}$  mbar and  $1 \times 10^{-4}$  to  $1 \times 10^3$  mbar. The pressure of the sorbent gas

was measured using a mercury gauge. The sample temperature was monitored using a K-type thermocouple located less than 5 mm away from the sample bucket. The variation in sample temperature was less than 0.1 K throughout the experiment.

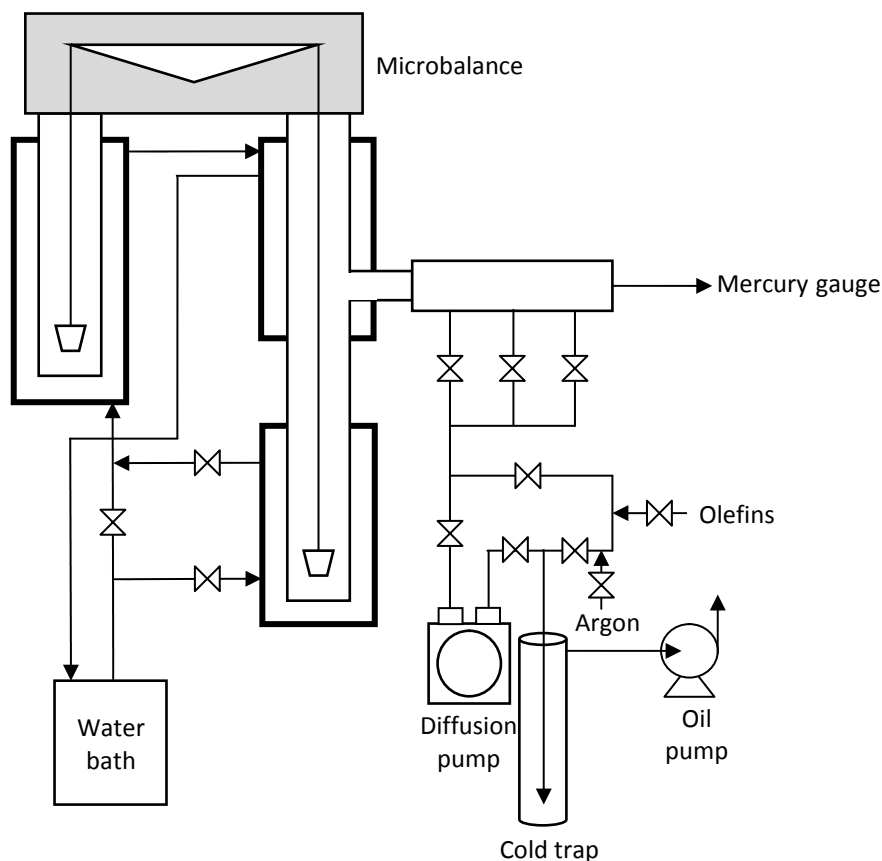


Figure 3.3: Schematic of home-built gravimetric adsorption apparatus.

25 – 30 mg of sample was subjected to an oil-pump vacuum until a pressure of approximately  $1 \times 10^{-2}$  mbar was reached, and then evacuated using a diffusion pump capable of reducing the pressure to approximately  $1 \times 10^{-4}$  mbar. The sample was heated at the required temperature using a heating jacket until no further weight loss was observed. The sample temperature was then decreased to the required experimental temperature and kept constant using either a circulation water bath or an ice bath.

The gas under investigation was introduced into the system until the desired pressure was achieved. The change in mass was measured as a function of time, and recorded once equilibrium had been reached. By introducing small increments of gas into the system and recording mass uptake at each point, an adsorption isotherm was

recorded. Gradual decrease of the pressure inside the system and recording of the mass at equilibrium produced a desorption isotherm.

## **3.2 Gas desorption**

### **3.2.1 Temperature programmed desorption**

Most temperature programmed desorption (TPD) experiments consist of three stages; preparation, gas loading and desorption. Throughout the experiment, a gas flows over a sample and the outgoing gas is detected by a mass spectrometer, but conditions such as the gas chosen or the temperature vary.

During the preparation phase an inert gas such as N<sub>2</sub> flows through the sample at high temperature. The effluent contains any molecules that are removed from the sample during this stage, such as water or solvent molecules, and their identity and relative concentration can be determined from the resultant mass spectrum.

The gas loading phase usually takes place at a lower temperature than the preparation phase. Short pulses of known quantities of the gas under investigation are passed through the sample. Some of the gas is adsorbed onto the sample, while the rest flows straight into the detector. For a short period, the inert gas is flowed through the sample once more to allow any unadsorbed gas to be removed from the system, after which another pulse is introduced. When the area under the mass peaks remains equal from pulse to pulse, the sorbent is fully saturated.

A steady flow of the inert gas is re-established for the desorption stage of the experiment. The temperature of the system is slowly increased at a certain ramp rate and desorption of the gas can be observed in the mass spectrum. When concentration of desorbed gas is plotted against peak temperature, the temperature of the maximum desorption rate corresponds to the peak maximum.

#### **3.2.1.1 Experimental**

TPD experiments were carried out on a Micromeritics AutoChem 2950 HP instrument. The outlet gas composition was monitored by a Pfeiffer Vacuum ThermoStar mass spectrometer with Quadstar 32-bit software.

Approximately 50 mg of sample was loaded into a stainless steel sample tube. Dehydration was carried out in an argon flow at atmospheric pressure at 200 °C for 3 hours. The system was cooled to -35 °C, at which temperature five olefin pulses were introduced followed by a 3 hour flow of argon gas to remove any unadsorbed olefin. The temperature was ramped at a programmed rate between 0.5 and 5 °C min<sup>-1</sup> to 150 °C and desorption of the gas was monitored using the mass spectrometer to produce a TPD spectrum.

### 3.2.2 Enthalpy of desorption

The enthalpy of desorption can be calculated from the TPD spectra.

In Redhead's method, equation (3.25) is used to calculate the enthalpy of desorption,  $E_d$ , from a single TPD spectrum. The pre-exponential factor,  $A$ , depends upon the degrees of freedom of the adsorbate gas and is therefore related to the number of attempts per second of an adsorbed gas to leave the surface.<sup>13</sup>

$$E_d = RT_{\max} \left( \ln \left( A \frac{T_{\max}}{\beta} \right) - 3.64 \right) \quad (3.25)$$

The heating rate variation technique assumes that, as is reasonable for most desorption experiments, the fractional surface coverage at the peak maximum is not a function of the heating rate. TPD spectra are recorded at a range of heating rates which vary by a factor of 10, and from each curve the peak temperature,  $T_p$ , can be calculated. Using equation (3.26), which is correct for a first order process, a plot of  $\ln \left( \frac{\beta}{T_{\max}^2} \right)$  against  $\frac{1}{T_{\max}}$  provides a straight line and the enthalpy of desorption can be calculated from its gradient.<sup>14</sup>

$$\ln \left( \frac{\beta}{T_{\max}^2} \right) = \ln \left( \frac{Rv_n}{E_d T_{\max}} \right) - \frac{E_d}{RT_{\max}} \quad (3.26)$$

### 3.3 Single crystal X-ray diffraction

The background and theory of single crystal X-ray diffraction can be found in *Crystal Structure Determination* by Clegg and *Crystal Structure Analysis: A Primer* by Glusker and Trueblood.<sup>15,16</sup>

#### 3.3.1 Synchrotron radiation

A synchrotron X-ray source produces a highly intense X-ray beam that can be used to study smaller crystals than is possible using a laboratory-based source. High resolution data can be collected, enabling time-resolved, high pressure or microcrystal studies to be undertaken.

Electrons are generated in an electron gun and accelerated through a linear accelerator and a booster synchrotron before injection into the storage ring (Figure 3.4). The storage ring consists of both straight and curved sections, and both regions can produce synchrotron radiation. In the curved sections the electron beam is bent by a strong magnetic field produced by a bending magnet. Insertion devices such as undulators and wigglers are installed in the straight sections of the storage ring, and consist of an array of magnets which ‘wiggle’ the electron beam, producing synchrotron radiation. When the electrons travelling at velocities close to the speed of light are bent with one of these magnets, synchrotron radiation is emitted tangentially to the direction of the electron beam at radiations ranging from microwaves to X-rays.

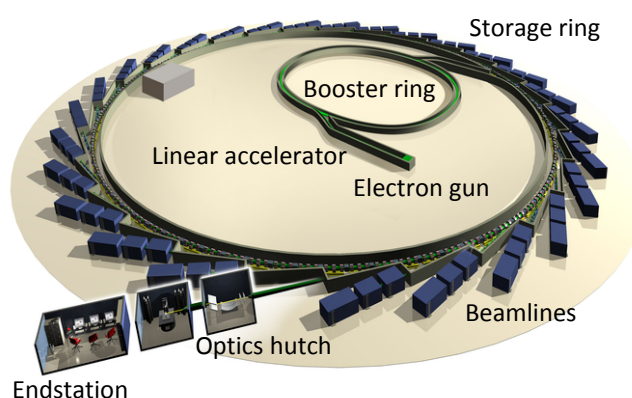


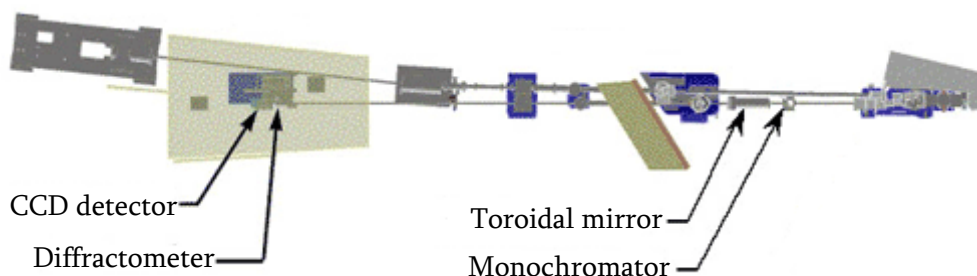
Figure 3.4: Diagram of a typical synchrotron (adapted from reference 17).

Experimental stations, or beamlines, use the synchrotron radiation produced by its bending magnet or insertion device. The beamline's optics adjust the radiation so that the beam received at the endstation is suitable for use in experiments.

### 3.3.2 Beamline 11.3.1

Single crystal X-ray diffraction was carried out on beamline 11.3.1 (Figure 3.5) at the Advanced Light Source at the Lawrence Berkeley National Laboratory in Berkeley, California.

The bending magnet produces radiation with wavelengths from 0.73 to 2.07 Å. A channel-cut Si(111) monochromator positioned 6 m from the radiation source is used to selectively remove the majority of the “white” radiation to give a monochromatic beam with a wavelength of 0.77490 Å. The beam is then focussed using a toroidal mirror located 14 m from the X-ray source. A Bruker CCD shutter controls the exposure time, and a collimator narrows the beam to 100 µm. The endstation uses an Apex II 3-circle diffractometer with a CCD detector, and is equipped with an Oxford Cryostreams 700 Plus device operating in the temperature



range of 100 – 500 K.

Figure 3.5: Diagram of beamline 11.3.1 (adapted from reference 18).

### 3.3.3 Structure solution and refinement

Absorption corrections were performed using SADABS.<sup>19</sup> Structure solution was carried out using SIR-97<sup>20</sup> in all cases, and refined on  $F^2$  using SHELXL-98<sup>21</sup> within the WinGX<sup>22</sup> suite. Non-hydrogen framework atoms were refined anisotropically, and the hydrogen atom on the organic linker was positioned geometrically.

The residual electron density within the pores was calculated using PLATON SQUEEZE.<sup>23,24</sup> A solvent accessible void is a region of a crystal structure in which a sphere of 1.2 Å radius can fit without intersecting the van der Waals radii of any atoms. The electron density within any such regions is estimated, and its contribution is removed from the structure to produce a new reflection file which can be refined against the original model, improving the *R*-factor. In this case SQUEEZE was used to estimate the excess electron density in the framework pores, which can be attributed to disordered water molecules, but the new reflection file was not used in refinements.

### 3.4 References

1. P. Webb and C. Orr, *Analytical methods in fine particle technology*, Micromeritics Instrument Corp., Norcross, Ga., 1997.
2. D. M. Young and A. D. Crowell, *Physical Adsorption of Gases*, Butterworths, London, 1962.
3. I. Langmuir, *J. Am. Chem. Soc.*, 1916, **38**, 2221–2295.
4. S. Brunauer, P. H. Emmett, and E. Teller, *J. Am. Chem. Soc.*, 1938, **60**, 309–319.
5. S. Brunauer, *The Adsorption of Gases and Vapours. Volume I: Physical Adsorption*, Oxford University Press, Oxford, 1944.
6. D. R. Lide, *CRC handbook of chemistry and physics : 2008-2009*, CRC Press, Boca Raton; London; New York, 89th edn., 2008.
7. *Chemistry3: introducing inorganic, organic and physical chemistry*, Oxford University Press, Oxford ; New York, 2009.
8. J. H. Cole, D. H. Everett, C. T. Marshall, A. R. Paniego, J. C. Powl, and F. Rodriguez-Reinoso, *J. Chem. Soc., Faraday Trans.*, 1974, **70**, 2154.
9. M. P. Suh, H. J. Park, T. K. Prasad, and D.-W. Lim, *Chem. Rev.*, 2012, **112**, 782–835.
10. L. Czepirski and J. JagiełŁo, *Chem. Eng. Sci.*, 1989, **44**, 797–801.
11. B. Chen, X. Zhao, A. Putkham, K. Hong, E. B. Lobkovsky, E. J. Hurtado, A. J. Fletcher, and K. M. Thomas, *J. Am. Chem. Soc.*, 2008, **130**, 6411–6423.
12. B. Xiao, P. S. Wheatley, X. Zhao, A. J. Fletcher, S. Fox, A. G. Rossi, I. L. Megson, S. Bordiga, L. Regli, K. M. Thomas, and R. E. Morris, *J. Am. Chem. Soc.*, 2007, **129**, 1203–1209.
13. N. D. Spencer, B. Elsener, and M. Heuberger, 2011.
14. J. L. Falconer and J. A. Schwarz, *Cat. Rev. - Sci. Eng.*, 1983, **25**, 141–227.

15. W. Clegg, *Crystal structure determination*, Oxford University Press, Oxford; New York, 1998.
16. J. P. Glusker, *Crystal structure analysis: a primer*, Oxford University Press, Oxford ; New York, 3rd ed., 2010.
17. *Diamond Light Source - Technology - Components of the machine - Booster synchrotron*.  
<http://www.diamond.ac.uk/Home/Technology/Components/booster.html>  
(accessed 03/05/2013).
18. *ALS Beamline 11.3.1: X-ray Diffraction Facility*.  
<http://xraysweb.lbl.gov/BL1131/1131website/index.htm> (accessed 02/05/2013).
19. *SADABS: Area-Detector Absorption Correction*, Bruker AXS Inc., Madison, Wisconsin, USA, 2001.
20. A. Altomare, M. C. Burla, M. Camalli, G. L. Cascarano, C. Giacovazzo, A. Guagliardi, A. G. Moliterni, G. Polidori, and R. Spagna, *J. Appl. Crystallogr.*, 1999, **32**, 115–119.
21. G. M. Sheldrick, *Acta Crystallogr., Sect. A: Found. Crystallogr.*, 2007, **64**, 112–122.
22. L. J. Farrugia, *J. Appl. Crystallogr.*, 1999, **32**, 837–838.
23. A. L. Spek, *J. Appl. Crystallogr.*, 2003, **36**, 7–13.
24. A. L. Spek, *Acta Crystallogr., Sect D: Biol. Crystallogr.*, 2009, **65**, 148–155.

# CHAPTER 4: Olefin adsorption in coordinatively unsaturated MOFs

## 4.1 Introduction

In MOFs where solvent molecules are coordinated to the metal centres, their removal can generate open metal sites. Activation procedures usually involve heat, vacuum or a dry inert gas stream, or a combination of heat with vacuum/dry gas. If a framework is porous and its open metal sites are accessible, they can be used to physisorb or chemisorb gases.

### 4.1.1 M-CPO-27

M-CPO-27 (CPO = coordination polymer, Oslo) was first synthesised by Dietzel et al. in 2005 as Co-CPO-27 by a hydrothermal reaction of cobalt(II) acetate and 2,5-dihydroxyterephthalic acid in water and tetrahydrofuran (THF) at 110 °C.<sup>1</sup> Large orange parallelepiped-shaped crystals of  $\text{Co}_2(\text{C}_8\text{H}_2\text{O}_6)(\text{H}_2\text{O})_2 \cdot 8\text{H}_2\text{O}$  were studied by single crystal X-ray diffraction (Figure 4.1).

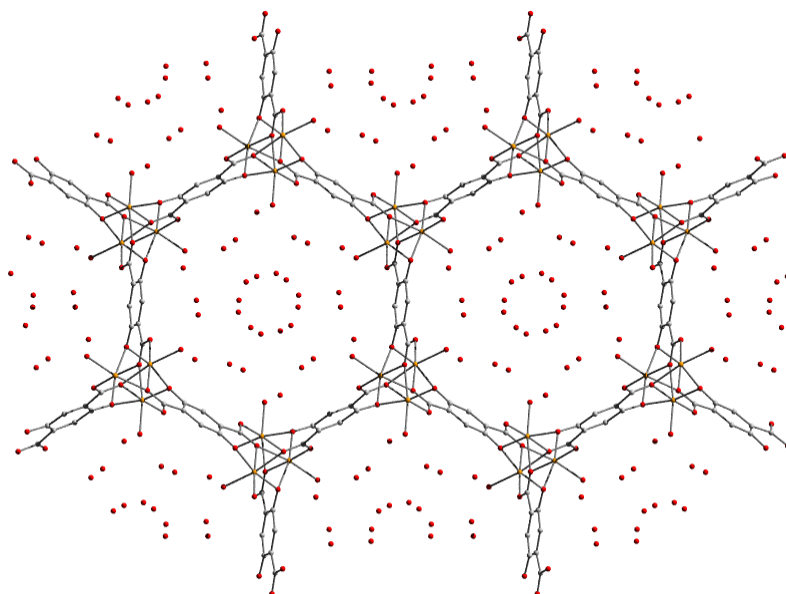


Figure 4.1: Crystal structure of Co-CPO-27 (cobalt atoms shown in orange, oxygen in red and carbon in grey; hydrogen atoms omitted for clarity).<sup>1</sup>

The 3-dimensional framework contains hexagonal shaped pores filled with water molecules, with water also coordinated to the cobalt(II) centres and pointing directly into the pores. A single crystal exposed to a hot nitrogen stream *in situ* provides a dehydrated crystal structure (Figure 4.2), where all water molecules within the pores, including those coordinated to the cobalt centre, are removed with no degradation of crystallinity.

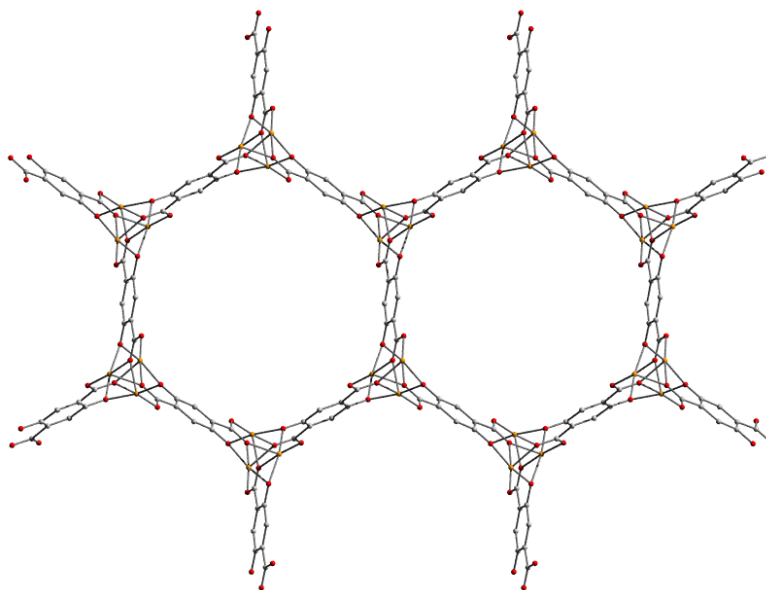


Figure 4.2: Crystal structure of dehydrated Co-CPO-27 (cobalt atoms shown in orange, oxygen in red and carbon in grey; hydrogen atoms omitted for clarity).<sup>1</sup>

The as-synthesised framework contains octahedral cobalt(II) centres. Dehydration removes the water ligand without any significant rearrangement of the other ligands, so the cobalt site in the dehydrated structure is square-pyramidal with one open metal site directly exposed to the pore.

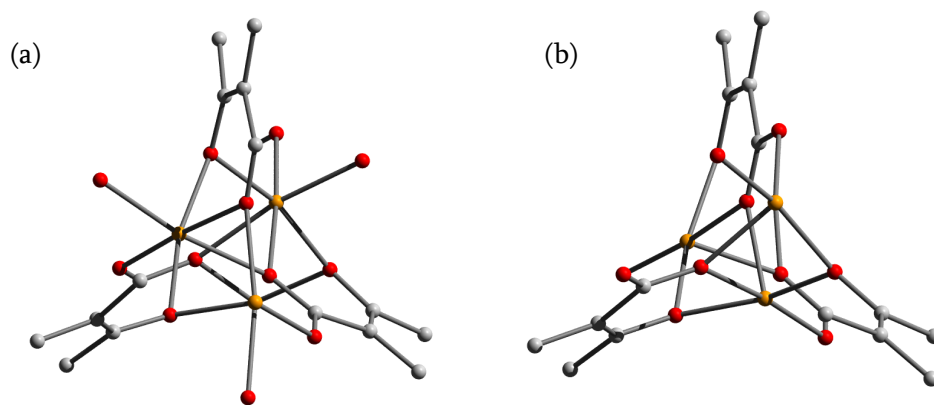


Figure 4.3: Cobalt centres of Co-CPO-27; (a) hydrated, with octahedral geometry around the cobalt site; (b) dehydrated, showing the square-pyramidal cobalt environment and the open metal site.

Analogous compounds in the M-CPO-27 series contain different metal cations, including nickel(II)<sup>2</sup>, magnesium(II)<sup>3</sup>, zinc(II)<sup>4</sup> and iron(II)<sup>5</sup>, all of which undergo complete dehydration upon exposure to heat and vacuum. The same framework was also synthesised in 2005 in its Zn-form by Yaghi et al. with DMF ligands coordinated to the cobalt sites, and was given the name MOF-74.<sup>6</sup>

Nitrogen adsorption isotherms for dehydrated Ni-CPO-27 provide a Langmuir surface area between 1083 m<sup>2</sup> g<sup>-1</sup> and 1316 m<sup>2</sup> g<sup>-1</sup>, a BET surface area of 1266 m<sup>2</sup> g<sup>-1</sup> and a pore volume of approximately 0.41 cm<sup>3</sup> g<sup>-1</sup>.<sup>2,7</sup> The same methods give a BET surface area of 1266 m<sup>2</sup> g<sup>-1</sup> and a pore volume of 0.50 cm<sup>3</sup> g<sup>-1</sup> for Co-CPO-27.<sup>7</sup> The high surface areas of the frameworks in the M-CPO-27 series along with the accessibility of the open metal sites have led to extensive investigation into their gas sorption properties.

#### 4.1.1.1 Olefin adsorption

Ethylene and propylene adsorption isotherms on Fe-CPO-27 at 25 °C, 60 °C and 80 °C were reported by Bloch et al. in 2012 (Figure 4.4) alongside adsorption isotherms of methane, ethane, acetylene and propane.<sup>8</sup> The steep rise in the ethylene, propylene and acetylene adsorption isotherms indicate a strong affinity between the framework and the unsaturated hydrocarbons. The adsorption capacity of the framework decreases with increasing temperature.

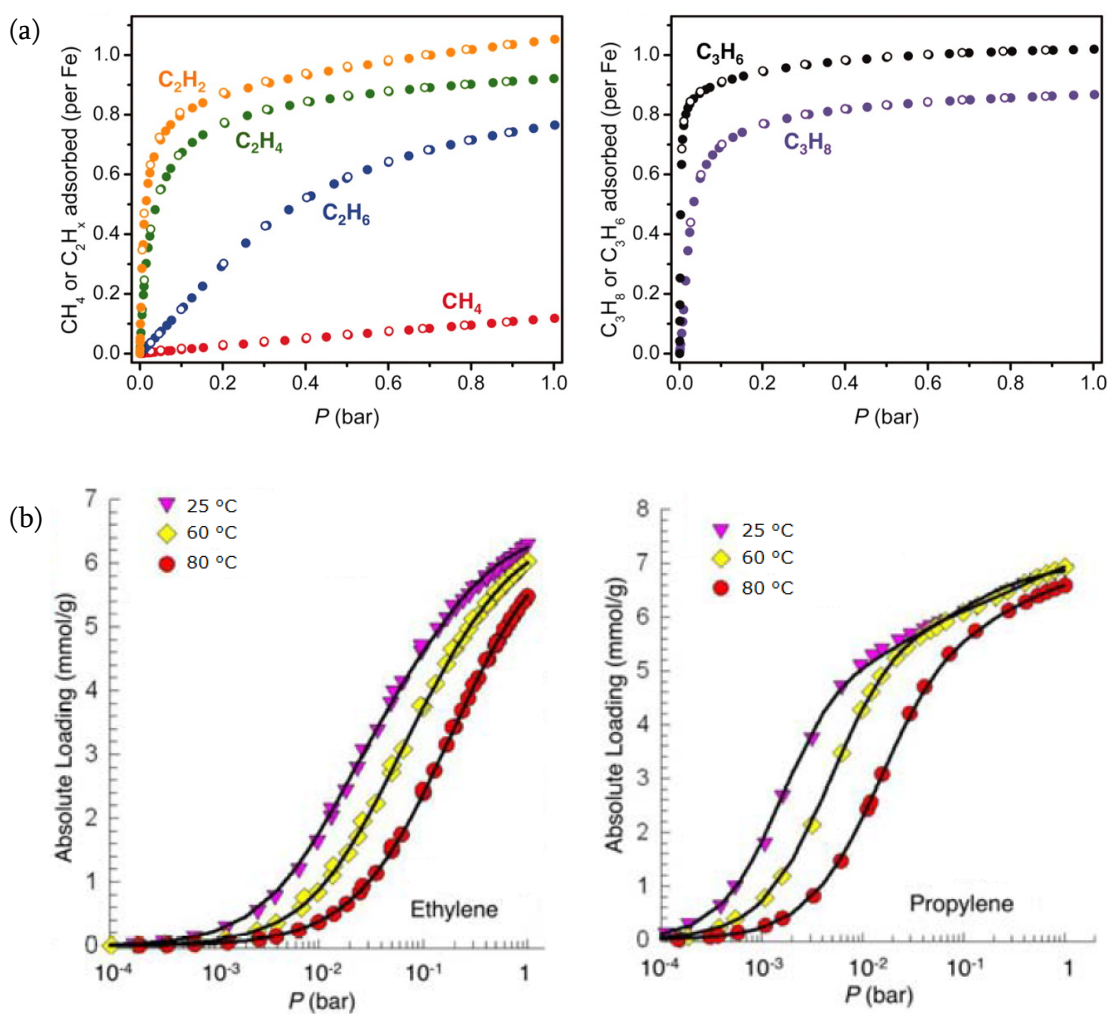


Figure 4.4: (a) Adsorption (filled circles) and desorption (open circles) isotherms on Fe-CPO-27 at 25 °C of methane, ethane, ethylene and acetylene, and propane and propylene. (b) Ethylene and propylene adsorption isotherms on Fe-CPO-27 at 25 °C, 60 °C and 80 °C. Figures adapted from reference 8.

Ethylene adsorption and desorption isotherms on Co-, Ni- and Zn-CPO-27 were reported in 2009 by Matzger et al.<sup>9</sup> The adsorption capacity of Ni-CPO-27 at 1 atm was the highest out of the frameworks tested at 7.97 mmol g<sup>-1</sup> and only Ni-CPO-27 displayed any hysteresis (Figure 4.5).

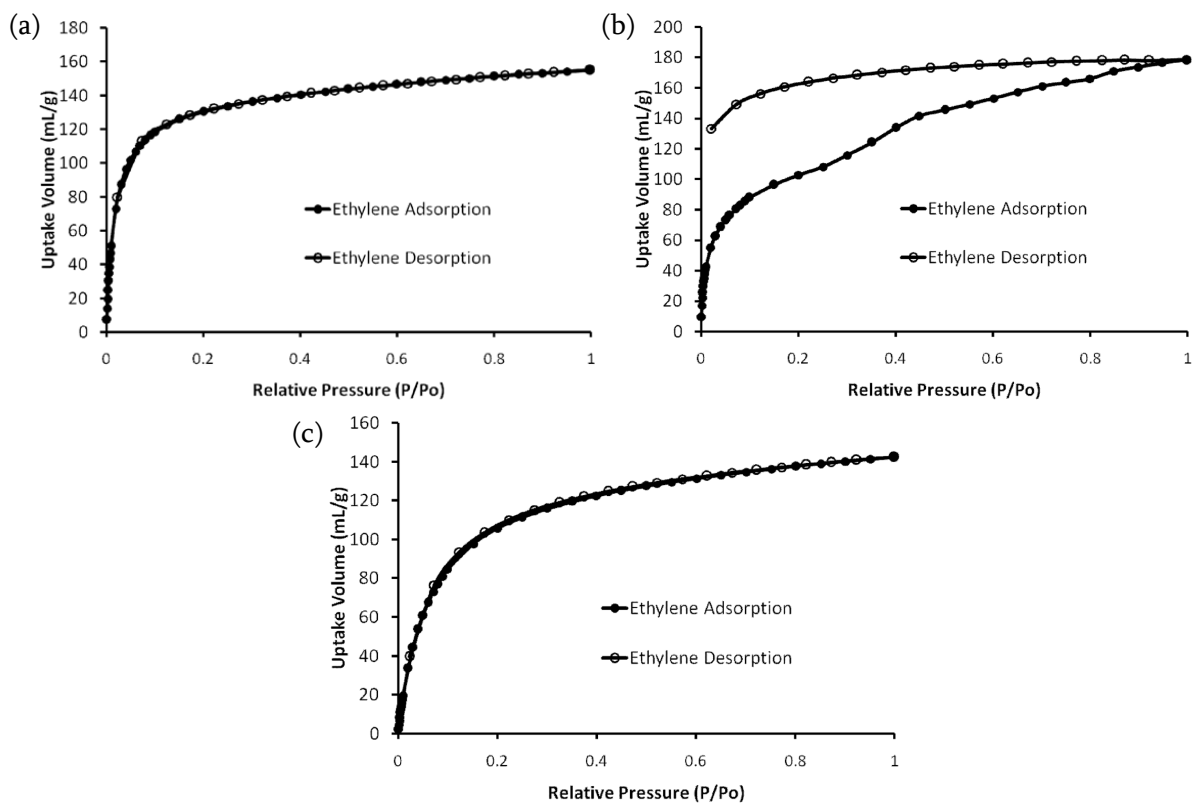


Figure 4.5: Ethylene adsorption and desorption isotherms at 25 °C on (a) Co-CPO-27, (b) Ni-CPO-27 and (c) Zn-CPO-27. Images adapted from reference 9.

#### 4.1.2 HKUST-1

HKUST-1 (HKUST = Hong Kong University of Science and Technology) was first synthesised by Chui et al. in 1999 by the hydrothermal reaction of copper(II) nitrate and trimesic acid in ethanol and water at 180 °C.<sup>10</sup> Cube-shaped turquoise crystals of  $\text{Cu}_3(\text{C}_9\text{O}_6\text{H}_3)_2(\text{H}_2\text{O})_3$  were studied by single crystal X-ray diffraction (Figure 4.6).

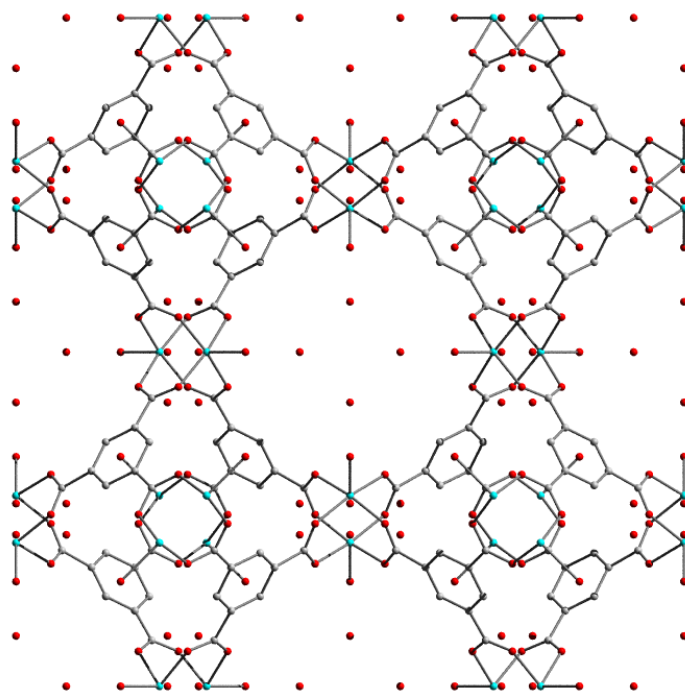


Figure 4.6: Crystal structure of HKUST-1 (copper atoms shown in turquoise, oxygen in red and carbon in grey; hydrogen atoms omitted for clarity).<sup>10</sup>

The three-dimensional framework contains square-shaped pores filled with water molecules, with water also coordinated to the copper(II) centres and pointing directly into the pores. Thermogravimetric analysis (TGA) shows that all water molecules can be removed from the framework by heating the sample under inert gas, with a colour change from turquoise to blue indicating a change in the copper coordination number.

The as-synthesised framework contains pseudo-octahedral copper(II) dimers (Figure 4.7). Dehydration removes the coordinated water ligand, leaving a pseudo-square-pyramidal copper site with one open metal site directly exposed to the pore.

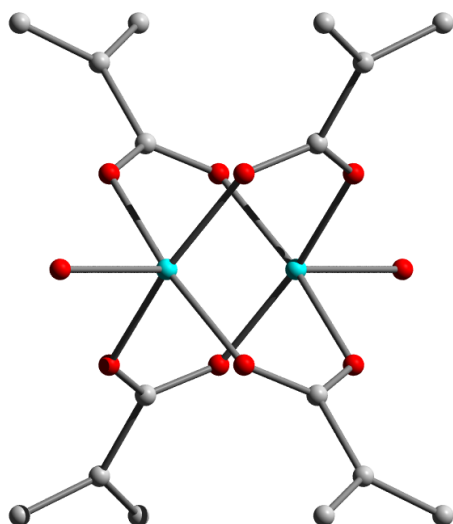


Figure 4.7: Copper dimer of HKUST-1, with pseudo-octahedral geometry around the copper site.

Nitrogen adsorption isotherms for dehydrated HKUST-1 provide a BET surface area of  $692.2 \text{ m}^2 \text{ g}^{-1}$ , a Langmuir surface area of  $917.6 \text{ m}^2 \text{ g}^{-1}$  and a pore volume of  $0.333 \text{ cm}^3 \text{ g}^{-1}$ .<sup>10</sup> The high surface area of HKUST-1 along with the accessibility of its open copper sites after dehydration has led to extensive investigation into its gas adsorption properties.<sup>11</sup>

#### 4.1.2.1 Olefin adsorption

Ethylene and ethane adsorption isotherms at  $22 \text{ }^\circ\text{C}$  were reported by Min Wang et al. (Figure 4.8).<sup>11</sup> Ethylene uptake is significantly higher than that of ethane. The authors suggest that this preferential uptake is due to interactions between the ethylene  $\pi$ -bond and the copper sites.

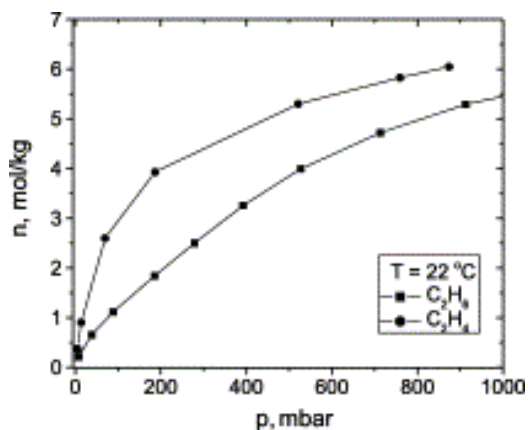


Figure 4.8: Ethylene and ethane adsorption isotherms at 22 °C on HKUST-1. Figure from reference 11.

Computational simulations of ethylene and ethane adsorption show that ethylene adsorbs twice as strongly to HKUST-1 as ethane at low pressures due to interactions between the  $\pi$ -bond and the copper sites. There is also more hydrogen-bonding between ethylene molecules and the oxygen atoms coordinated to the copper site than with ethane due to the orientation of the adsorbed molecules (Figure 4.9). As more ethylene is adsorbed, the binding energy per molecule increases as a result of increased van der Waals interactions between adsorbed molecules.<sup>12</sup>

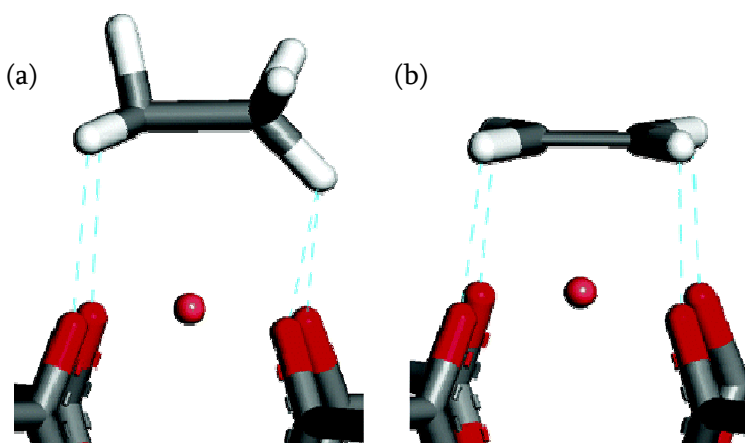


Figure 4.9: Computationally simulated positions of (a) ethane and (b) ethylene on the HKUST-1 metal sites, showing hydrogen bonds to framework oxygen atoms as dashed lines.

The copper cation is the central red sphere. Figure from reference 12.

The ethylene adsorption isotherm on HKUST-1 at 22 °C was simulated and compared to the experimental isotherm discussed above. Isosteric heats of adsorption at varying coverages, calculated using the same computational techniques, decrease initially up to a coverage of 4 mmol g<sup>-1</sup> before increasing. Firstly, ethylene molecules are adsorbed onto open metal sites in the side pockets of HKUST-1, then onto the open metal sites in the pores. Once these sites are all occupied, further molecules are adsorbed into the centre of the pores. The weaker adsorption into the centre of the pores corresponds to a decrease in isosteric heat of adsorption. After a certain loading, interactions between ethylene molecules increase leading to a slight increase in isosteric heat of adsorption (Figure 4.10).<sup>13</sup>

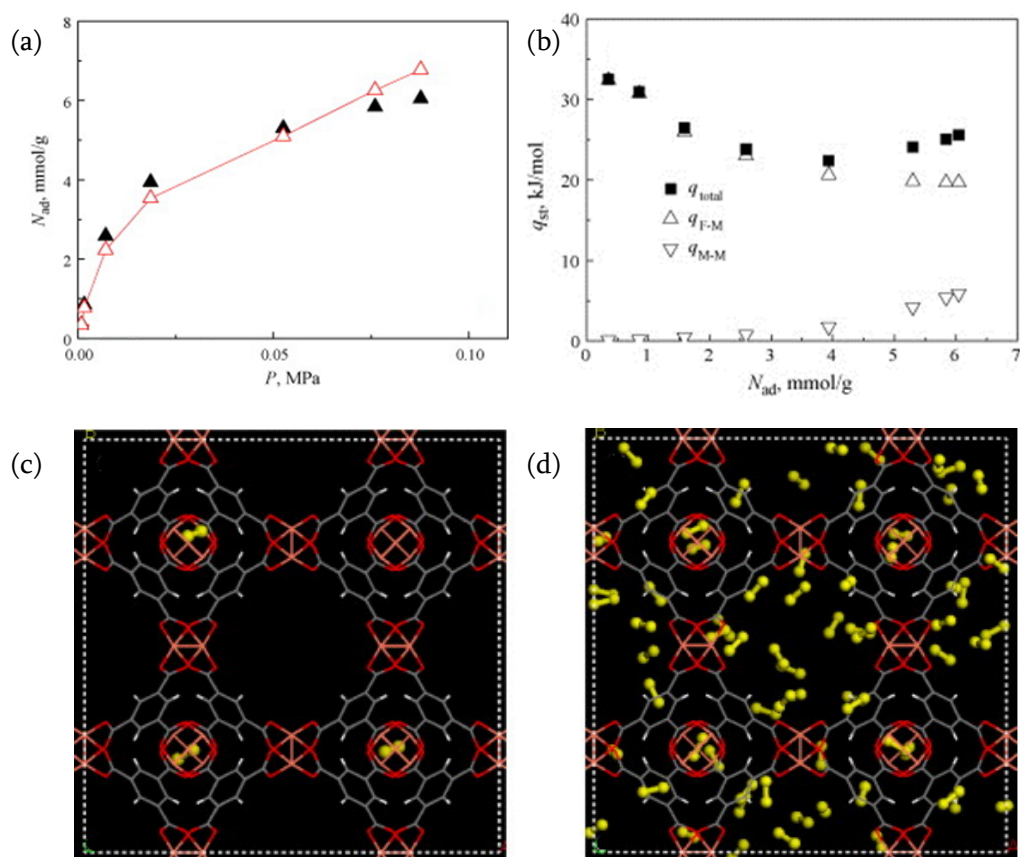


Figure 4.10: (a) Simulated (open triangles) and experimental (filled triangles) ethylene adsorption isotherms on HKUST-1 at 22 °C; (b) isosteric heats of adsorption for ethylene on HKUST-1 ( $q_{total}$  is the total isosteric heat,  $q_{F-M}$  is the contribution from the interactions between the framework and ethylene, and  $q_{M-M}$  is the contribution from the interactions between ethylene molecules); (c) simulated ethylene adsorption to copper sites in the pockets at 0.001 MPa; (d) simulated ethylene adsorption to all copper sites and within the centre of the pores at 0.1 MPa. Figure adapted from reference 13.

### 4.1.3 STAM-1

STAM-1 (STAM = St Andrews MOF) was synthesised by Mohideen et al. in 2011 by the hydrothermal reaction of copper(II) nitrate and trimesic acid in methanol and water at 110 °C. Turquoise crystals of  $\text{Cu}(\text{C}_{10}\text{H}_6\text{O}_6)(\text{H}_2\text{O}) \cdot 1.66\text{H}_2\text{O}$  were studied by single crystal X-ray diffraction (Figure 4.11).<sup>14</sup>

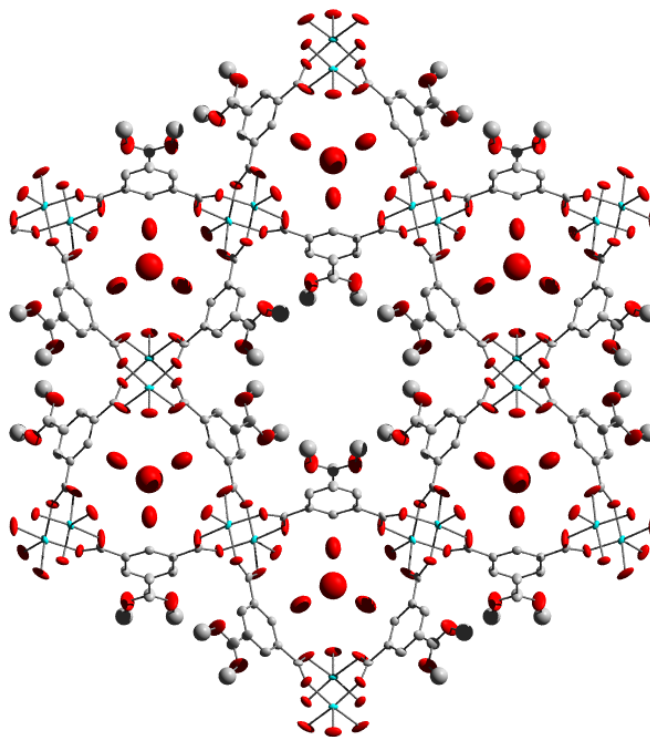


Figure 4.11: Crystal structure of STAM-1 (copper atoms shown in turquoise, oxygen in red and carbon in grey; hydrogen atoms omitted for clarity).

The STAM-1 framework contains the same pseudo-octahedral copper(II) dimers as HKUST-1 (Figure 4.12) arranged to form triangle-shaped pores with coordinated water molecules pointing inside. These hydrophilic pores have a diameter of approximately 5.7 Å as-synthesised and contain ordered solvent molecules. STAM-1 also contains hydrophobic pores lined with ester groups with a pore diameter of approximately 4 Å.

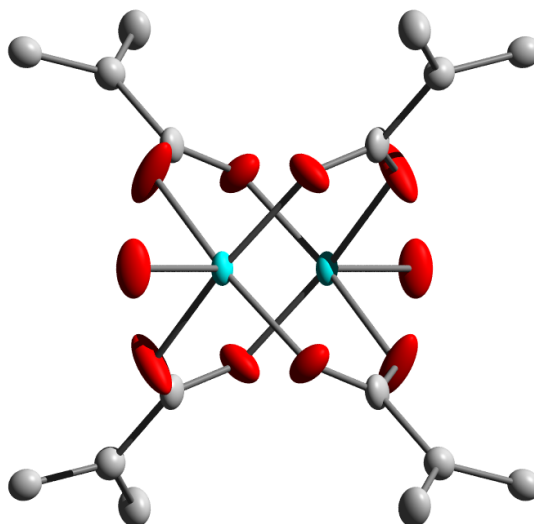


Figure 4.12: Copper dimer of STAM-1, with pseudo-octahedral geometry around the copper sites.

TGA studies show that dehydration occurs up to 150 °C, with powder X-ray diffraction indicating that the dehydrated material remains crystalline. The cell parameters of STAM-1 alter slightly upon dehydration and the framework's symmetry changes from trigonal to triclinic, showing that some structural changes occur due to dehydration. Removal of all solvent molecules from the framework changes the copper environment from pseudo-octahedral to pseudo-square pyramidal, and provides open copper sites in the hydrophilic pores.

Adsorption isotherms of CO<sub>2</sub>, N<sub>2</sub>O, N<sub>2</sub> and CH<sub>4</sub> on STAM-1 provide significantly lower pore volumes than predicted from either crystallographic or molecular modelling studies (CO<sub>2</sub> isotherms give a pore volume of 0.11 cm<sup>3</sup>g<sup>-1</sup> whereas the expected total pore volume is 0.24 cm<sup>3</sup> g<sup>-1</sup>). However, methanol and water vapour adsorption isotherms show pore volumes very similar to the predictions (both 0.22 cm<sup>3</sup> g<sup>-1</sup>). This suggests that only the hydrophobic channels are accessible

for CO<sub>2</sub>, N<sub>2</sub>O, N<sub>2</sub> and CH<sub>4</sub> adsorption, whereas both the hydrophobic and hydrophilic channels are accessible to methanol and water. The methanol and water adsorption isotherms indicate that a gated adsorption process occurs; up to the gate opening pressure, adsorption only occurs into one type of pore, at which point a framework structure change allows access to the second pore-type and the adsorption amount markedly increases (Figure 4.13).

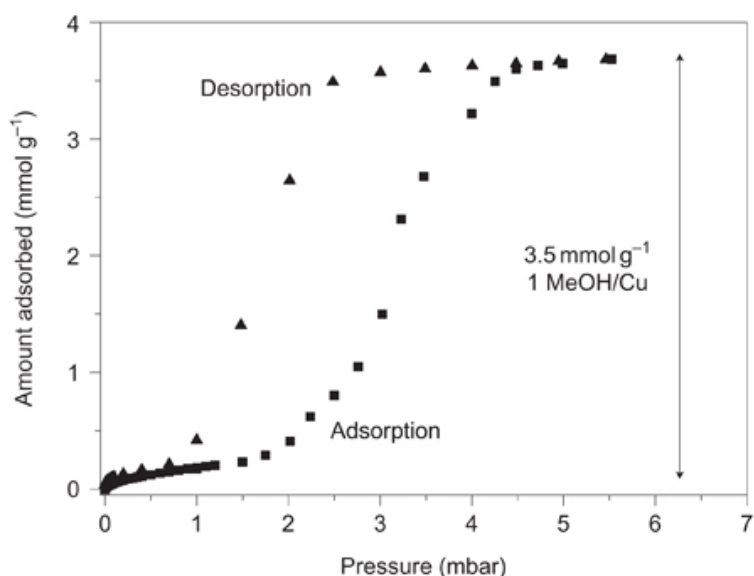


Figure 4.13: Adsorption and desorption isotherms of methanol on STAM-1 at 75 °C.

## 4.2 Aims

In order to evaluate the capacity of MOFs for olefin separation, it is important to understand their behaviour during olefin adsorption. This chapter aims to investigate the adsorption behaviour of Ni-CPO-27 and HKUST-1 using ethylene and propylene. Isothermic heats of adsorption will be calculated both at zero coverage and at higher, varying coverages, allowing the frameworks' capacity for olefin adsorption to be evaluated. Comparisons of the adsorption behaviour will be made between frameworks and gases. Ethylene and propylene adsorption isotherms on STAM-1 will also be examined and compared to isotherms in the literature.

### 4.3 M-CPO-27 results

Ni-CPO-27 was used to study the adsorption isotherms for ethylene and propylene due to its ease of synthesis, high surface area and reproducible porosity.<sup>15</sup>

#### 4.3.1 Ethylene

Gravimetric ethylene adsorption and desorption isotherms on Ni-CPO-27 were carried out at four temperatures; 0 °C, 25 °C, 40 °C and 80 °C (Figure 4.14). In contrast to the isotherm reported in the literature (Figure 4.5), only a small amount of hysteresis was observed at each temperature; the adsorption process was largely reversible.

The steep rises at the beginning of the adsorption isotherms indicate a strong affinity between ethylene and Ni-CPO-27, particularly at lower temperatures. At 25 °C and 777 mmHg, ethylene coverage is at 6.10 mmol g<sup>-1</sup>, which is considerably less than that reported by Matzger et al. at 7.59 mmol g<sup>-1</sup> at atmospheric pressure.<sup>9</sup> At 40 °C and a pressure of 762 mmHg, ethylene uptake corresponds to 6.12 mmol g<sup>-1</sup> which is very close to one ethylene molecule per metal site (6.42 mmol g<sup>-1</sup>) and to ethylene uptake in Fe-CPO-27 at 45 °C and 650 mmHg (6.02 mmol g<sup>-1</sup>).<sup>8</sup>

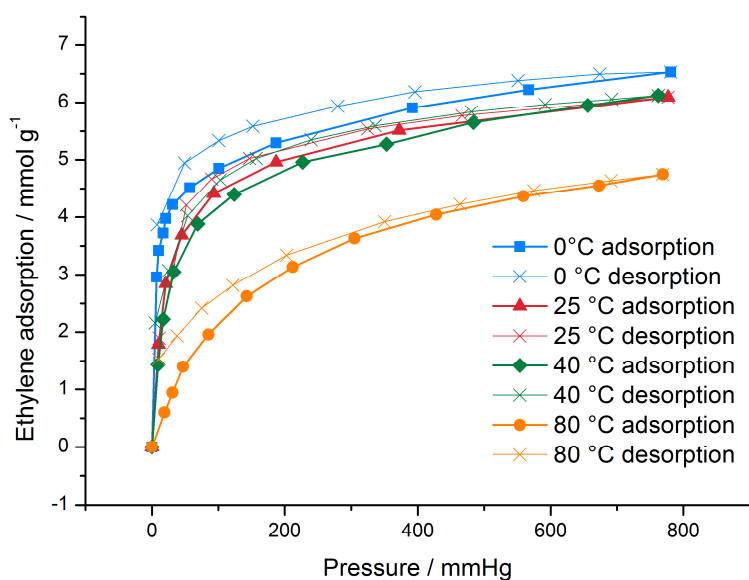


Figure 4.14: Ethylene adsorption isotherms for Ni-CPO-27 at varying temperatures.

Isosteres were plotted using the four adsorption isotherms (Figure 4.15(a)), allowing the calculation of heat of adsorption at varying coverages (Figure 4.15(b)) using the Clausius-Clapeyron equation (3.24).  $R^2$  values ranged from 0.84 for a coverage of 6 mmol g<sup>-1</sup> to 0.999 for 5 mmol g<sup>-1</sup>. Isosteres at 5 and 6 mmol g<sup>-1</sup> only contain three points, as coverage at 80 °C and 1 atm was less than 5 mmol g<sup>-1</sup>. The isosteric heat of adsorption increases as coverage increases, suggesting that the presence of ethylene molecules within the framework encourages the uptake of further ethylene, probably through intermolecular interactions; this is, however, a small effect. After a coverage of 3 mmol g<sup>-1</sup> the isosteric heat of adsorption decreases as more ethylene is introduced into the framework suggesting that, as loading approaches 1 gas molecule per metal site the heat of adsorption decreases, possibly due to the coordinated ethylene molecules sterically hindering access to the remaining open metal sites.

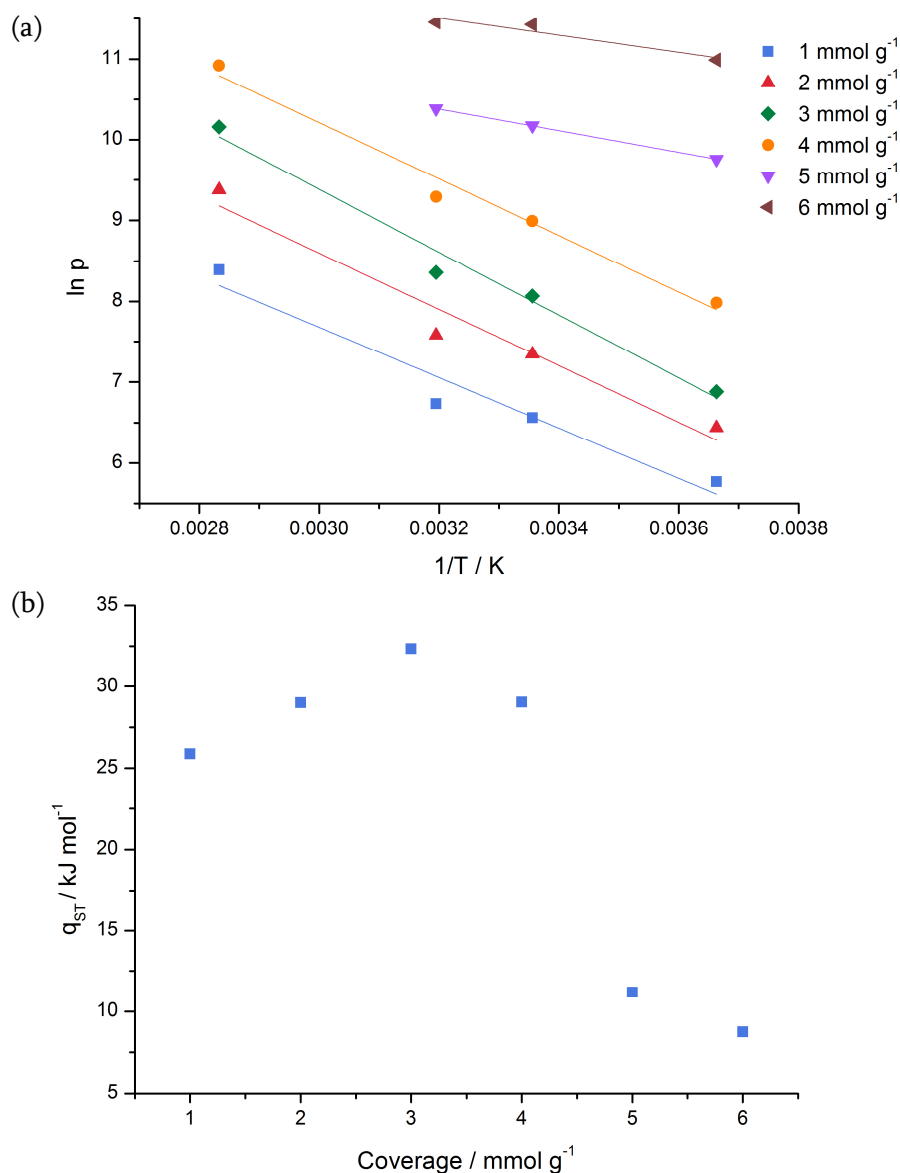


Figure 4.15: (a) Isotherms for ethylene adsorption on Ni-CPO-27 at varying coverages; (b) isosteric heat of adsorption as a function of loading for ethylene on Ni-CPO-27.

Virial plots of the adsorption isotherms (Figure 4.16) produced straight lines with  $R^2$  values above 0.94 (Table 4.1), and  $A_0$  values for each temperature were calculated from the linear regressions. A van't Hoff plot (Figure 4.16) also produced a straight line with an  $R^2$  value of 0.97, from which the isosteric enthalpy of adsorption at zero coverage was calculated to be 57.79 kJ mol<sup>-1</sup> with an estimated error of 5.80 kJ mol<sup>-1</sup>.

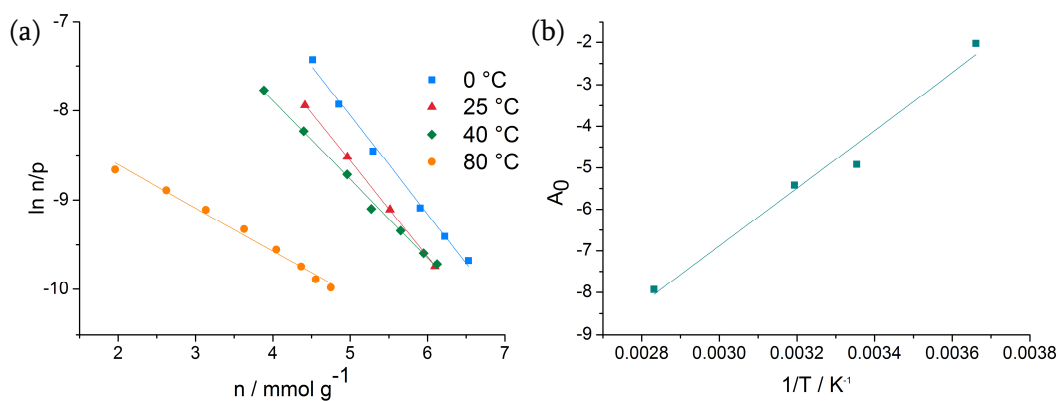


Figure 4.16: (a) Virial plots and (b) van't Hoff plot for ethylene adsorption on Ni-CPO-27.

Table 4.1: Henry's constants for adsorption of ethylene on Ni-CPO-27.

Temperature / °C	$K_H / \text{mmol g}^{-1} \text{ kPa}^{-1}$	$R^2$
0	$132 \pm 24$	0.990
25	$7.3 \pm 2.5$	0.941
40	$4.4 \pm 0.9$	0.966
80	$0.36 \pm 0.03$	0.970

Henry's constant is highest at 0 °C, decreasing quickly as the temperature of adsorption decreases. This suggests that the interactions between ethylene and Ni-CPO-27 are significantly reduced at higher temperatures.

Model adsorption isotherms were calculated from the virial parameters and plotted in Figure 4.17 for comparison to the experimental results.

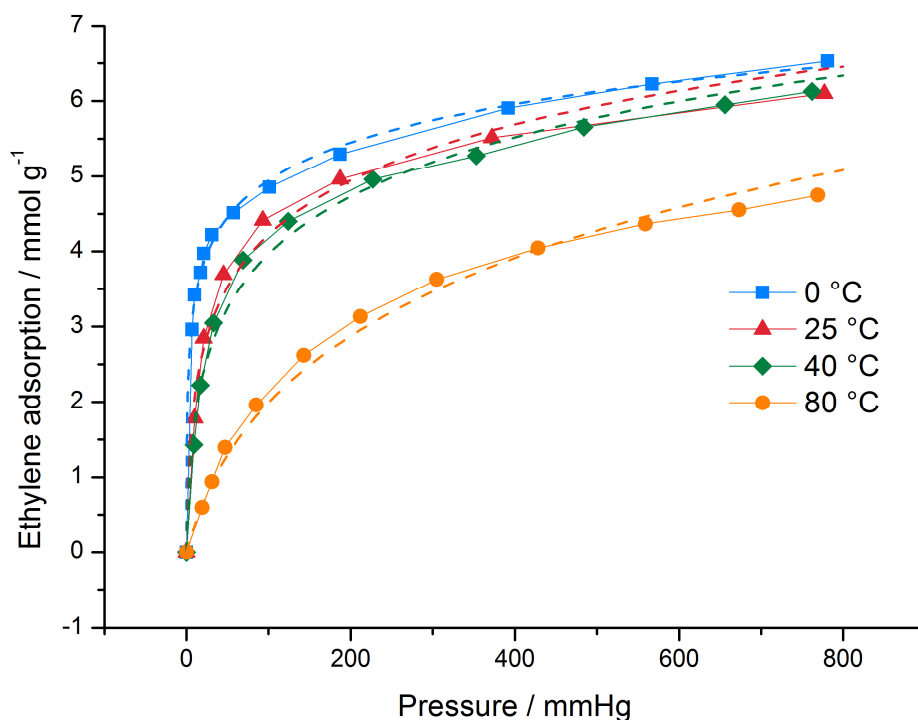


Figure 4.17: Adsorption isotherms for ethylene on Ni-CPO-27. Solid lines are experimental isotherms. Dashed lines are isotherms calculated from the virial parameters.

The calculated isotherms underestimate ethylene adsorption at low pressures and overestimate at high pressures. Examination of the virial plots in Figure 4.16 reveals that the data are not perfectly represented by single straight lines, particularly at higher temperatures. Adsorption of ethylene seems to change the framework's capacity for further adsorption, and so two straight lines may better represent the real data.

Figure 4.16 indicates that deviation from linearity does not occur at a particular coverage at all temperatures, so pressure was used as a limit. The isotherms were treated in two sections; data points below 50 mmHg ethylene pressure, and data points above 50 mmHg ethylene pressure. As before, virial plots and van't Hoff plots were produced (Figure 4.18).

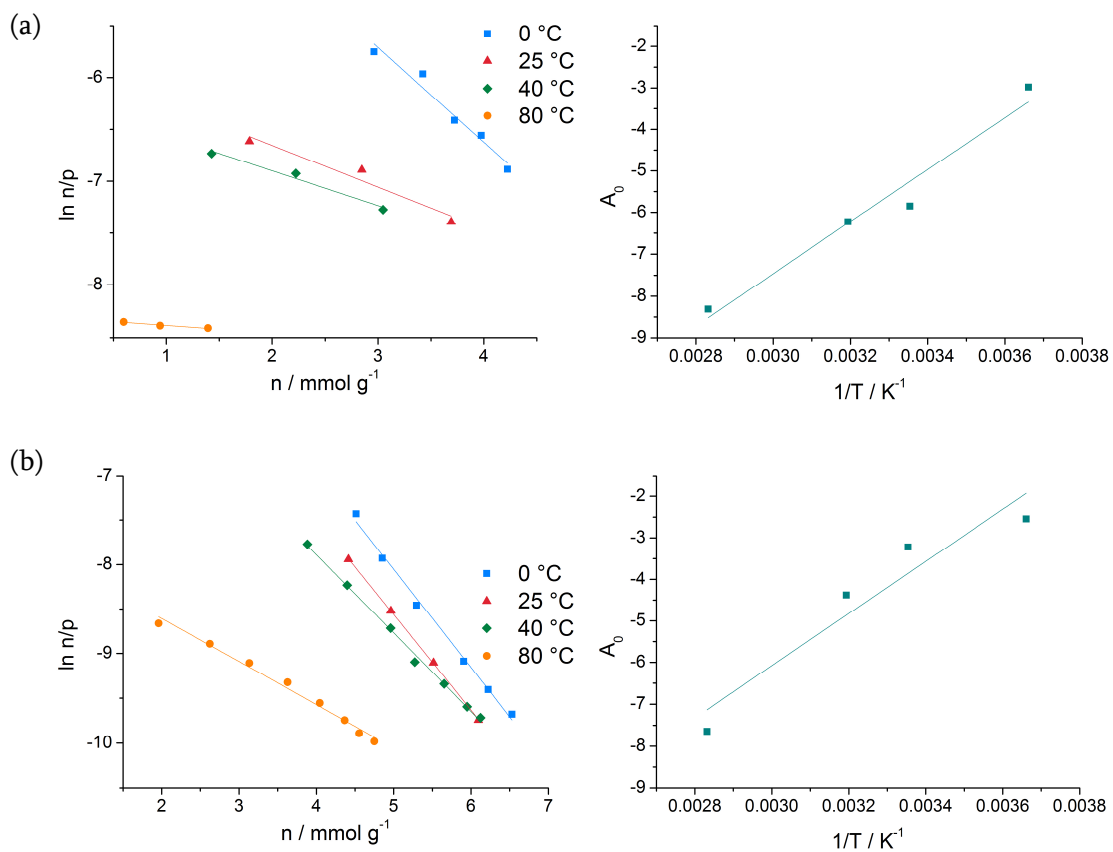


Figure 4.18: Virial plots (left) and van't Hoff plot (right) for ethylene adsorption on Ni-CPO-27, (a) below 50 mmHg; (b) above 50 mmHg.

Table 4.2: Henry's constants for adsorption of ethylene below and above 50 mmHg on Ni-CPO-27.

Temperature / °C	$K_H$ (below 50 mmHg) / $\text{mmol g}^{-1} \text{kPa}^{-1}$	$R^2$	$K_H$ (above 50 mmHg) / $\text{mmol g}^{-1} \text{kPa}^{-1}$	$R^2$
0	$51.0 \pm 24.1$	0.951	$78.7 \pm 17.9$	0.993
25	$2.9 \pm 2.5$	0.894	$40.1 \pm 1.4$	0.999
40	$2.0 \pm 0.9$	0.953	$12.6 \pm 1.5$	0.996
80	$0.25 \pm 0.03$	0.912	$0.48 \pm 0.04$	0.986

The isosteric enthalpy of adsorption was  $51.90 \text{ kJ mol}^{-1} \pm 7.15 \text{ kJ mol}^{-1}$  below 50 mmHg, and  $52.19 \text{ kJ mol}^{-1} \pm 11.14 \text{ kJ mol}^{-1}$  above 50 mmHg. Henry's constant

(Table 4.2) is higher at ethylene pressures above 50 mmHg, suggesting that gas molecules interact more with the framework surface at higher pressures.

Model isotherms were calculated from the virial parameters to produce Figure 4.19.

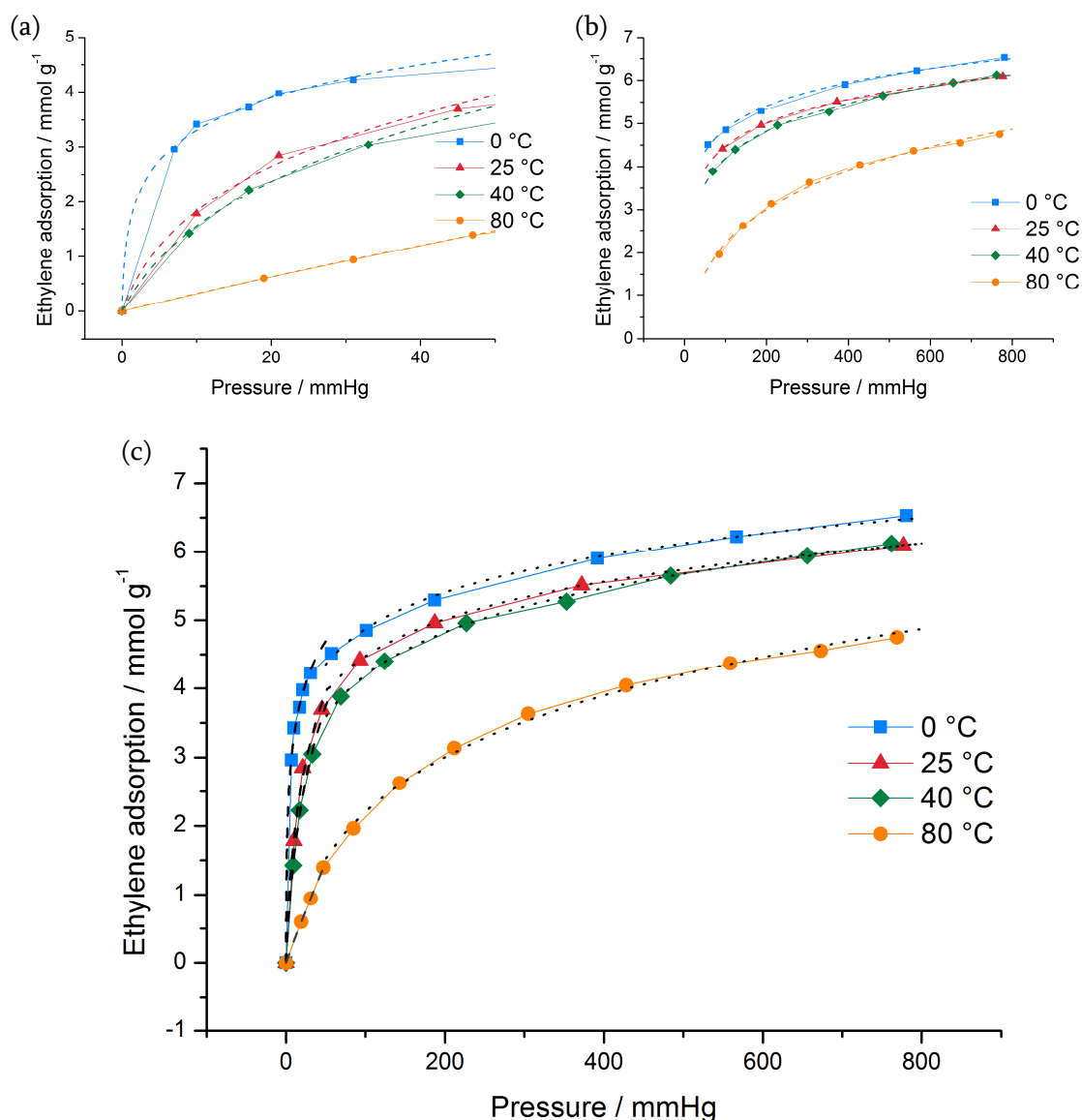


Figure 4.19: Adsorption isotherms for ethylene on Ni-CPO-27. (a) Below 50 mmHg. Solid lines are experimental isotherms. Dashed lines are isotherms calculated from the virial parameters. (b) Above 50 mmHg. Solid lines are experimental isotherms. Dashed lines are isotherms calculated from the virial parameters. (c) Full isotherms. Solid lines are experimental isotherms. Dashed and dotted lines are isotherms calculated from the virial parameters below and above 50 mmHg respectively.

The combined calculated isotherms in Figure 4.19(c) are much closer to the experimental results, particularly at higher ethylene pressures. This signifies that the treatment of ethylene adsorption onto Ni-CPO-27 as taking place over two stages is a reasonable model.

### 4.3.2 Propylene

Gravimetric propylene adsorption and desorption isotherms on Ni-CPO-27 were carried out at four temperatures; 25 °C, 35 °C, 40 °C and 55 °C (Figure 4.20). The adsorption process is reversible with no hysteresis observed.

The steep rises at the beginning of the adsorption isotherms indicate that Ni-CPO-27 has a strong affinity for propylene at all four temperatures. At 25 °C and 754 mmHg, propylene coverage is 7.12 mmol g<sup>-1</sup>. The adsorption capacity of Ni-CPO-27 is much higher than one molecule of propylene per nickel atom (6.42 mmol g<sup>-1</sup>), so some propylene is being adsorbed into the centre of the pores after saturation of the metal sites. Propylene uptake in Ni-CPO-27 at 40 °C (6.79 mmol g<sup>-1</sup> at 780 mmHg) is higher than in Fe-CPO-27 at 45 °C and 650 mmHg (6.66 mmol g<sup>-1</sup>)<sup>8</sup>.

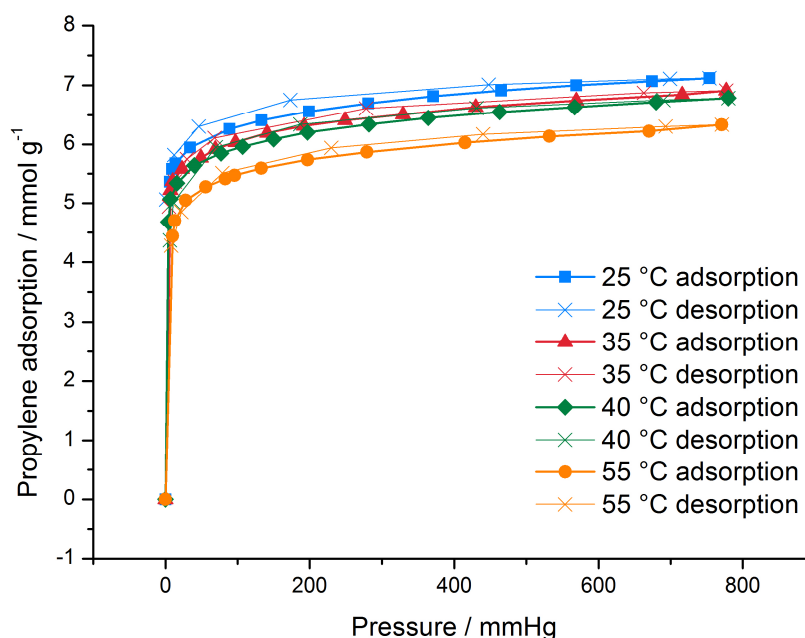


Figure 4.20: Propylene adsorption isotherms for Ni-CPO-27 at varying temperatures.

Due to the steep isotherms at low pressures, propylene coverage was not measured below 4 mmol g<sup>-1</sup>. Therefore isosteres could not be produced for propylene adsorption on Ni-CPO-27, preventing the calculation of isosteric enthalpy of adsorption at varying coverage.

Virial plots of the adsorption isotherms (Figure 4.21(a)) produced straight lines with  $R^2$  values above 0.99 and  $A_0$  values for each temperature were calculated from the linear regressions. A van't Hoff plot (Figure 4.21(b)) also produced a straight line with an  $R^2$  value of 0.963, from which the isosteric enthalpy of adsorption at zero coverage was calculated to be 125.96 kJ mol<sup>-1</sup> with an estimated error of 17.45 kJ mol<sup>-1</sup>.

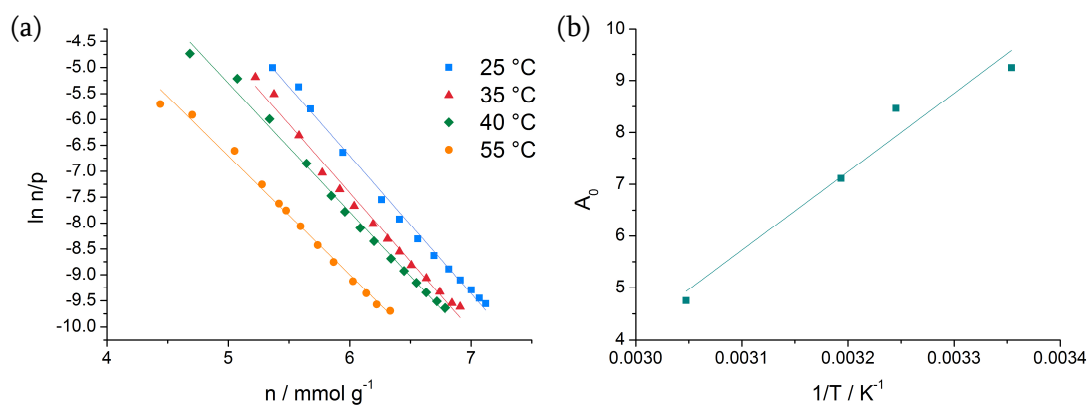


Figure 4.21: (a) Virial plots and (b) van't Hoff plot for propylene adsorption on Ni-CPO-27.

Table 4.3: Henry's constants for adsorption of propylene on Ni-CPO-27.

Temperature / °C	$K_H$ / mmol g <sup>-1</sup> kPa <sup>-1</sup>	$R^2$
25	10340000 ± 3720000	0.995
35	4740000 ± 2300000	0.990
40	1227000 ± 415000	0.994
55	116200 ± 41200	0.992

Henry's constant (Table 4.3) is highest at 25 °C, decreasing as the temperature of adsorption decreases. This suggests that the interactions between propylene and Ni-CPO-27 are reduced at higher temperatures.

Model adsorption isotherms were calculated from the virial parameters and plotted in Figure 4.22 for comparison to the experimental results.

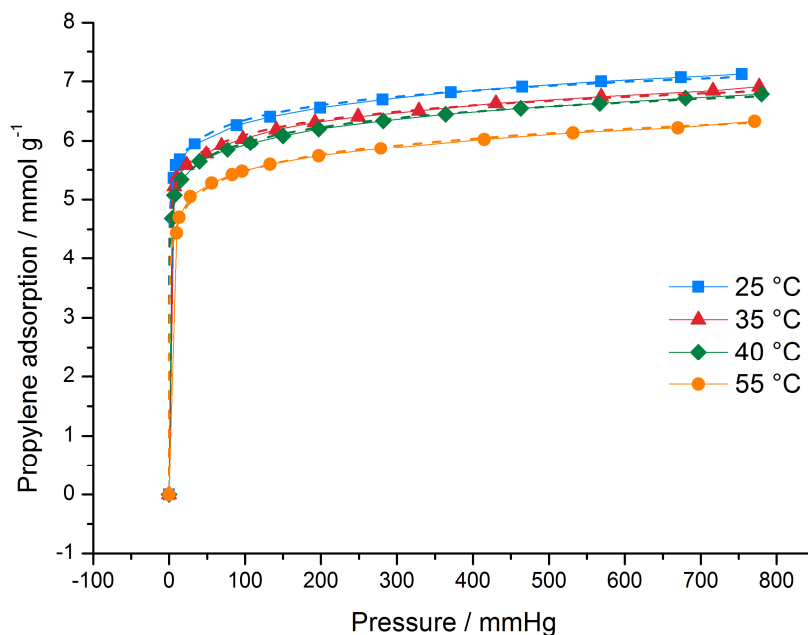


Figure 4.22: Adsorption isotherms for propylene on Ni-CPO-27. Solid lines are experimental isotherms. Dashed lines are isotherms calculated from the virial parameters.

The calculated isotherms accurately represent propylene adsorption throughout the full temperature and pressure range, as supported by the virial plots in Figure 4.21 which produce straight lines with high  $R^2$  values. Adsorption of propylene does not change the framework's capacity for further adsorption.

## 4.4 HKUST-1 results

### 4.4.1 Ethylene

Gravimetric ethylene adsorption and desorption isotherms on HKUST-1 were carried out at four temperatures; 25 °C, 35 °C, 40 °C and 55 °C (Figure 4.23). The adsorption process is reversible with no hysteresis observed.

The steep rise at the beginning of the 25 °C adsorption isotherm indicates that HKUST-1 has a strong affinity for ethylene at this temperature, although at higher temperatures this affinity is significantly weaker, as evidenced by the much shallower

ethylene uptake. At 25 °C and 772 mmHg, ethylene coverage is 8.17 mmol g<sup>-1</sup>, which is higher than that observed before both experimentally (approximately 6 mmol g<sup>-1</sup> at 22 °C and 675 mmHg)<sup>11</sup> and computationally (approximately 7 mmol g<sup>-1</sup> at 22 °C and 675 mmHg)<sup>13</sup>. The adsorption capacity of HKUST-1 is much higher than one molecule of ethylene per copper atom (4.96 mmol g<sup>-1</sup>), so some ethylene is being adsorbed into the centre of the pores after saturation of the metal sites.

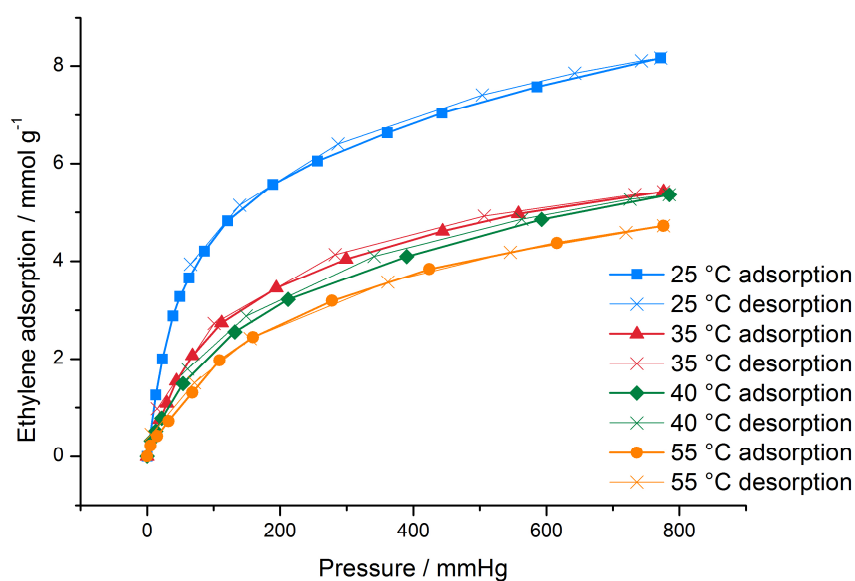


Figure 4.23: Ethylene adsorption isotherms for HKUST-1 at varying temperatures.

Isosteres were plotted using the four adsorption isotherms (Figure 4.24(a)), allowing the calculation of heat of adsorption at varying coverages (Figure 4.24(b)).  $R^2$  values ranged from 0.789 for a coverage of 4 mmol g<sup>-1</sup> to 0.937 for 5 mmol g<sup>-1</sup>. Isosteres at 4 and 5 mmol g<sup>-1</sup> only contain three points, as coverage at 55 °C did not exceed 5 mmol g<sup>-1</sup>.

The isosteric heat of adsorption increases as coverage increases, suggesting that the presence of ethylene molecules within the framework encourages the uptake of further gas through intermolecular interactions, although this is only a small effect. The enthalpy calculated at 5 mmol g<sup>-1</sup> coverage is anomalously high, caused by the use of only three isotherms in its calculation.

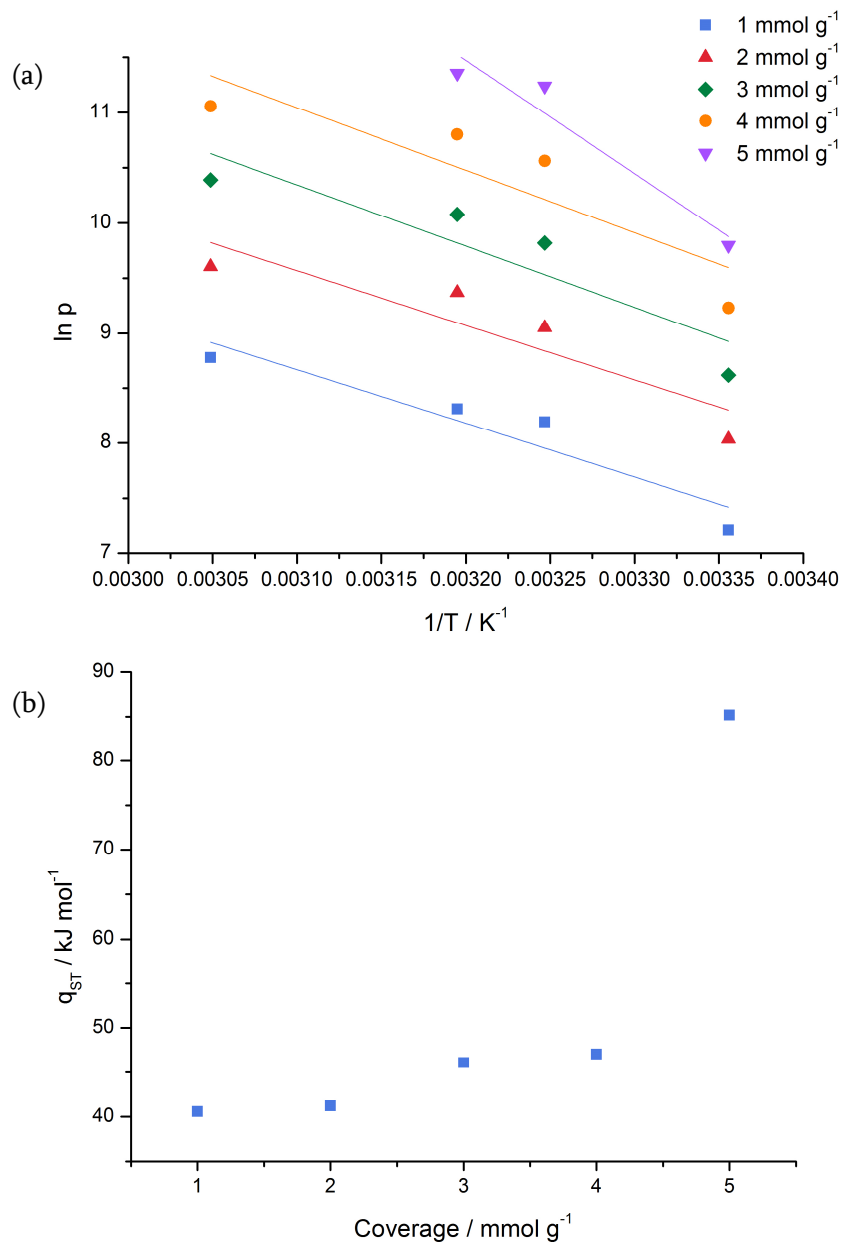


Figure 4.24: (a) Isosteres for ethylene adsorption on HKUST-1 at varying coverages; (b) isosteric heat of adsorption as a function of loading for ethylene on HKUST-1.

Virial plots of the adsorption isotherms (Figure 4.25(a)) produced straight lines with  $R^2$  values above 0.89, and  $A_0$  values for each temperature were calculated from the linear regressions. A van't Hoff plot (Figure 4.25(b)) also produced a straight line with an  $R^2$  value of 0.72, from which the isosteric enthalpy of adsorption was calculated to be 42.03 kJ mol<sup>-1</sup> with an estimated error of 14.45 kJ mol<sup>-1</sup>.

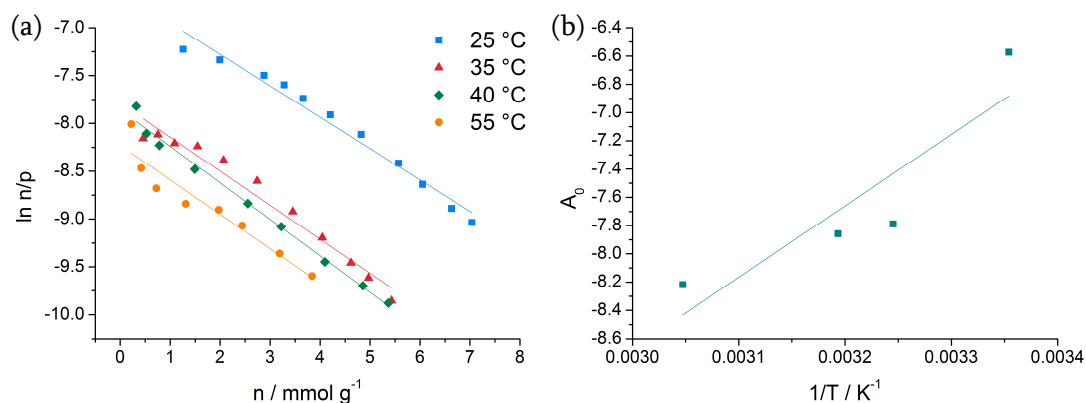


Figure 4.25: (a) Virial plots and (b) van't Hoff plot for ethylene adsorption on HKUST-1.

Table 4.4: Virial constants for adsorption of ethylene on HKUST-1.

Temperature / °C	$K_H / \text{mmol g}^{-1} \text{ kPa}^{-1}$	$R^2$
25	$1.33 \pm 0.10$	0.972
35	$0.415 \pm 0.030$	0.964
40	$0.387 \pm 0.017$	0.990
55	$0.267 \pm 0.021$	0.895

Henry's constant (Table 4.4) is highest at 25 °C, decreasing as the temperature of adsorption decreases. This suggests that the interactions between ethylene and HKUST-1 are reduced at higher temperatures.

Model adsorption isotherms were calculated from the virial parameters and plotted in Figure 4.26 for comparison to the experimental results.

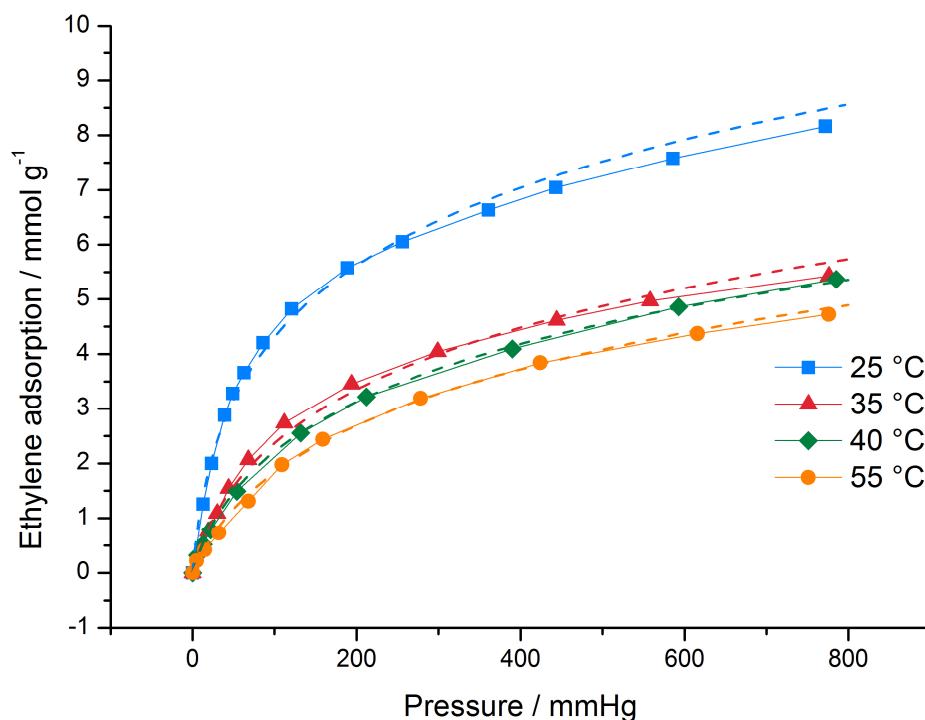


Figure 4.26: Adsorption isotherms for ethylene on HKUST-1. Solid lines are experimental isotherms. Dashed lines are isotherms calculated from the virial parameters.

The calculated isotherms slightly underestimate ethylene adsorption at low pressures and overestimate at high pressures, although this effect is much more significant for the isotherms obtained at 25 °C and 35 °C. The calculated isotherms at 40 °C and 80 °C are good approximations of the experimental isotherms. Examination of the virial plots in Figure 4.25 reveals that the data are not perfectly represented by single straight lines, particularly at higher temperatures and lower coverages. If adsorption of ethylene changes the framework's capacity for further adsorption, possibly through contraction or expansion of the framework, two straight lines may better represent the real data.

The isotherms were treated in two sections; data points below 50 mmHg ethylene pressure, and data points above 50 mmHg ethylene pressure. As before, virial plots and van't Hoff plots were produced (Figure 4.27).

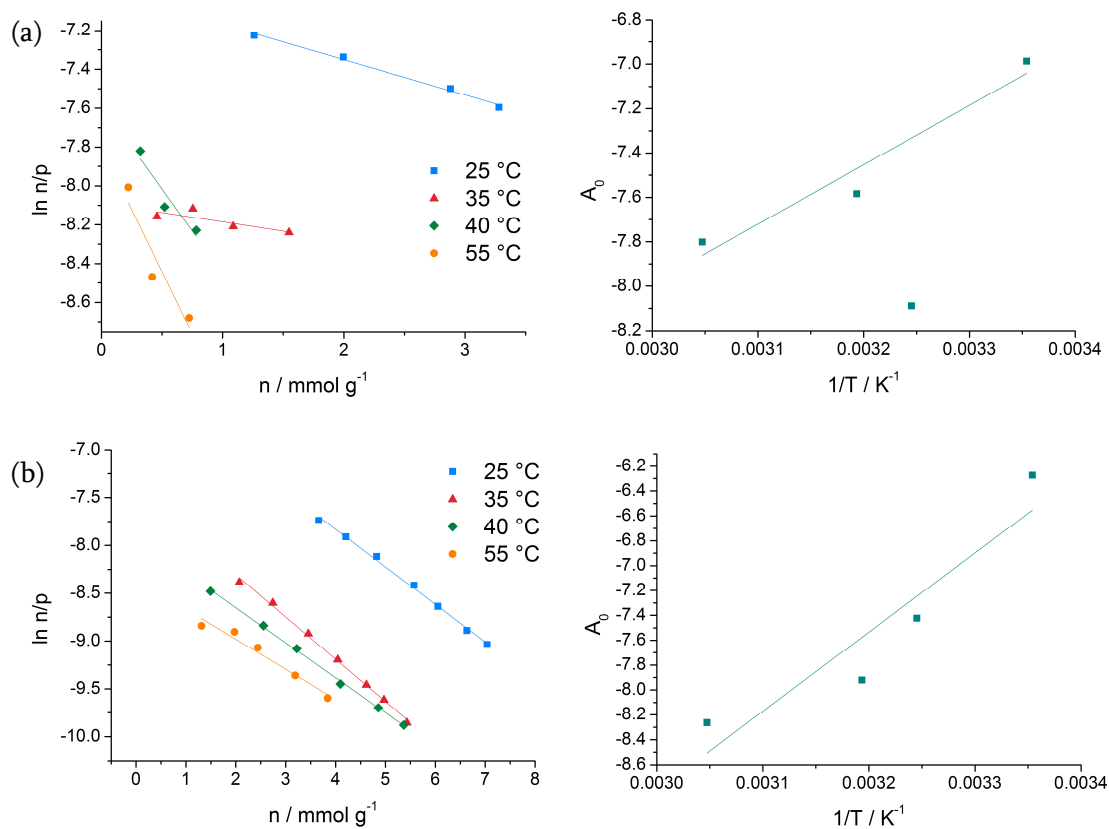


Figure 4.27: Virial plots (left) and van't Hoff plots (right) for ethylene adsorption on HKUST-1, (a) below 50 mmHg (straight line in van't Hoff plot calculated without point \*); (b) above 50 mmHg.

Table 4.5: Henry's constants for adsorption of ethylene below and above 50 mmHg on HKUST-1.

Temperature / °C	$K_H$ (below 50 mmHg) / $\text{mmol g}^{-1} \text{kPa}^{-1}$	$R^2$	$K_H$ (above 50 mmHg) / $\text{mmol g}^{-1} \text{kPa}^{-1}$	$R^2$
25	$1.247 \pm 0.025$	0.989	$1.906 \pm 0.074$	0.996
35	$0.307 \pm 0.015$	0.528	$0.597 \pm 0.026$	0.996
40	$0.509 \pm 0.081$	0.816	$0.363 \pm 0.009$	0.998
55	$0.409 \pm 0.092$	0.785	$0.236 \pm 0.020$	0.952

The isosteric enthalpy of adsorption was calculated to be  $22.78 \text{ kJ mol}^{-1} \pm 5.16 \text{ kJ mol}^{-1}$  below 50 mmHg, and  $56.51 \text{ kJ mol}^{-1} \pm 13.68 \text{ kJ mol}^{-1}$  above 50 mmHg. Henry's constant is very similar below and above 50 mmHg (Table 4.5), so the interactions between ethylene and HKUST-1 are similar at all pressures.

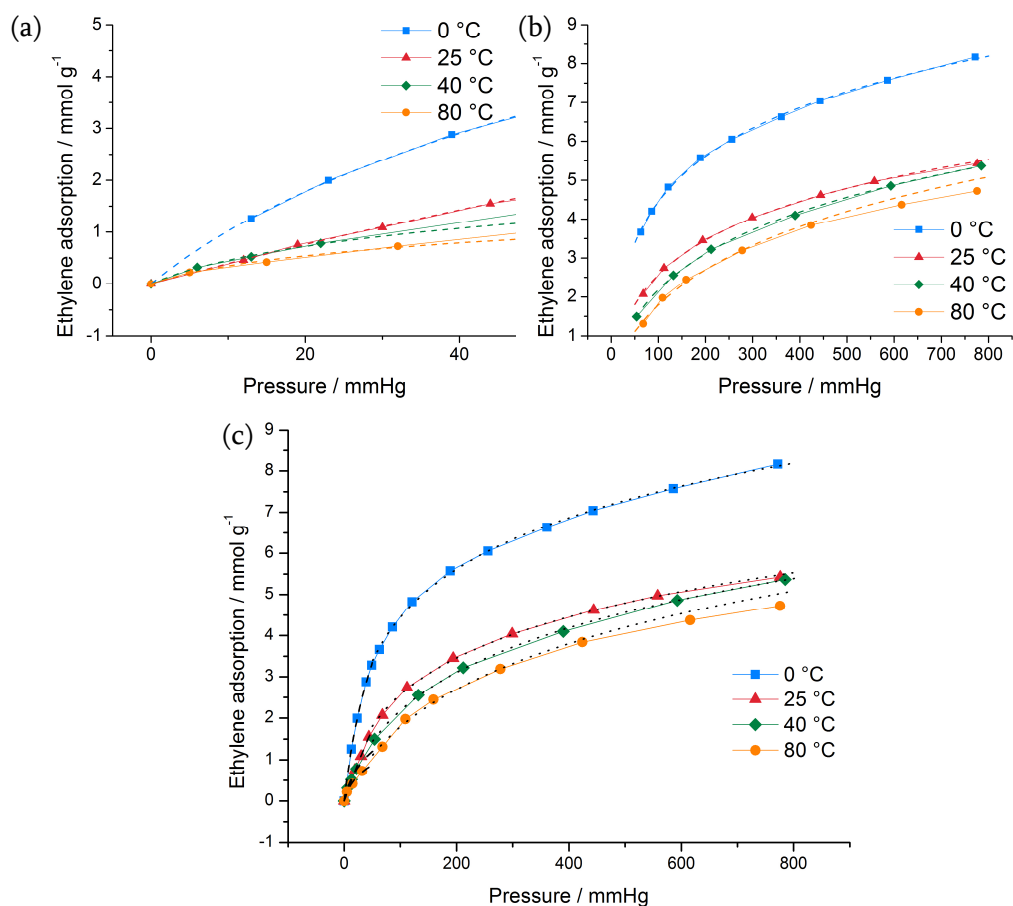


Figure 4.28: Adsorption isotherms for ethylene on HKUST-1. (a) Below 50 mmHg. Solid lines are experimental isotherms. Dashed lines are isotherms calculated from the virial parameters. (b) Above 50 mmHg. Solid lines are experimental isotherms. Dashed lines are isotherms calculated from the virial parameters. (c) Full isotherms. Solid lines are experimental isotherms. Dashed lines are isotherms calculated from the virial parameters under and over 50 mmHg.

The combined calculated isotherms in Figure 4.28(c) are slightly closer to the experimental results than the isotherms in Figure 4.26. However,  $R^2$  values throughout the series of calculations are much higher overall when the adsorption isotherms are treated as a single set of data. The adsorption of ethylene onto

HKUST-1 is preferentially modelled by a single step process, so ethylene adsorption does not appear to change the framework structure in a way that alters its adsorption capacity.

#### 4.4.2 Propylene

Gravimetric propylene adsorption and desorption isotherms on HKUST-1 were carried out at four temperatures; 25 °C, 35 °C, 40 °C and 55 °C (Figure 4.29). The adsorption process is reversible with no hysteresis observed.

The steep rises at the beginning of the adsorption isotherms indicate that HKUST-1 has a strong affinity for propylene, although at higher temperatures this affinity is slightly weaker than at lower temperatures. At 25 °C and 777 mmHg, ethylene coverage is 7.02 mmol g<sup>-1</sup>. The adsorption capacity of HKUST-1 is much higher than one molecule of propylene per copper atom (4.96 mmol g<sup>-1</sup>), so some propylene is being adsorbed into the centre of the pores after saturation of the metal sites.

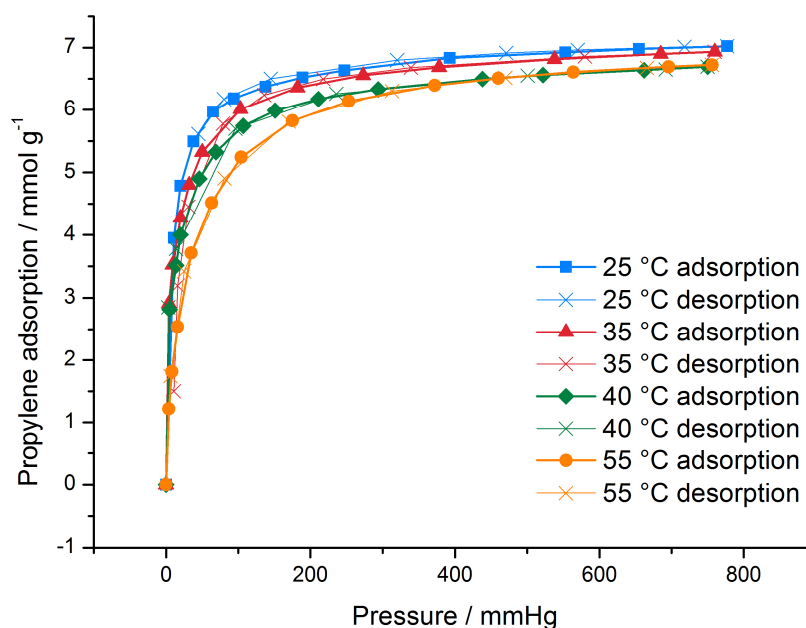


Figure 4.29: Propylene adsorption isotherms for HKUST-1 at varying temperatures.

Isosteres were plotted (Figure 4.30(a)), allowing the calculation of heat of adsorption at varying coverages (Figure 4.30(b)). Only the 35 °C, 40 °C and 55 °C isotherms were used to plot isosteres due to the lack of low-coverage data at 25 °C.  $R^2$  values ranged from 0.88 for a coverage of 6 mmol g<sup>-1</sup> to 0.999 for 4 mmol g<sup>-1</sup>.

The isosteric heat of adsorption increases as coverage increases up to 3 mmol g<sup>-1</sup>, suggesting that the presence of propylene molecules within the framework encourages the uptake of further gas through intermolecular interactions. After 3 mmol g<sup>-1</sup> of propylene is present within the framework, the isosteric heat of adsorption decreases. The open copper sites are not fully occupied at this coverage, so the propylene within the framework must be hindering the adsorption of more gas, possible through steric effects.

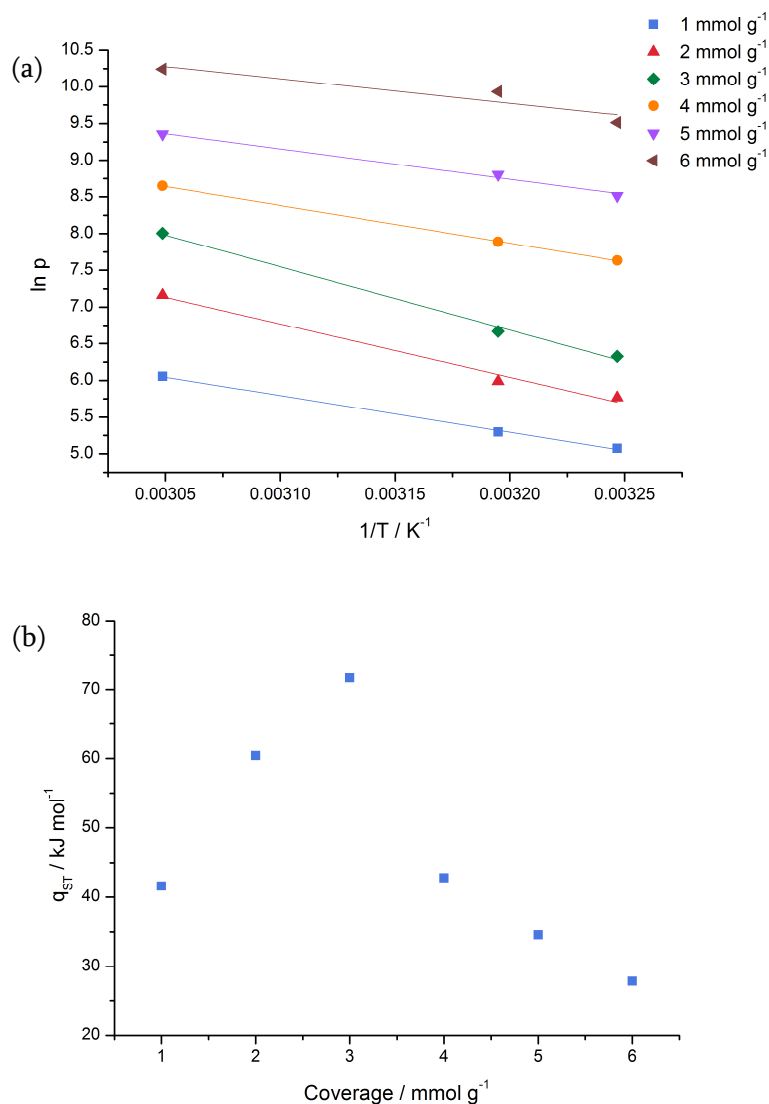


Figure 4.30: (a) Isosteres for propylene adsorption on HKUST-1 at varying coverages; (b) isosteric heat of adsorption as a function of loading for propylene on HKUST-1.

Virial plots of the adsorption isotherms (Figure 4.31(a)) produced straight lines with  $R^2$  values above 0.901, and  $A_0$  values for each temperature were calculated from the linear regressions. A van't Hoff plot (Figure 4.31(b)) also produced a straight line with an  $R^2$  value of 0.989, from which the isosteric enthalpy of adsorption was calculated to be 124.72 kJ mol<sup>-1</sup> with an estimated error of 9.51 kJ mol<sup>-1</sup>.

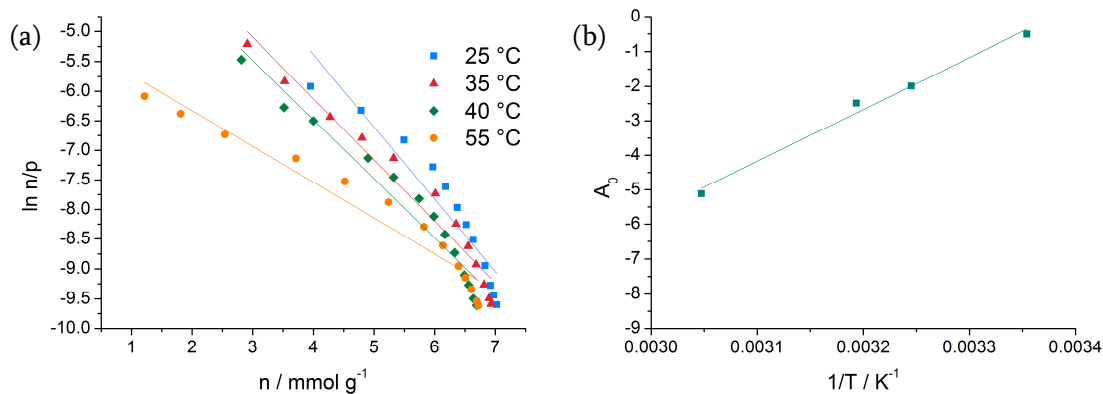


Figure 4.31: (a) Virial plots and (b) van't Hoff plot for propylene adsorption on HKUST-1.

Table 4.6: Henry's constants for adsorption of propylene on HKUST-1.

Temperature / °C	$K_H / \text{mmol g}^{-1} \text{ kPa}^{-1}$	$R^2$
25	$605 \pm 533$	0.901
35	$137 \pm 54$	0.961
40	$83.7 \pm 33.0$	0.951
55	$6.01 \pm 1.38$	0.948

Henry's constant (Table 4.6) is highest at 25 °C, decreasing quickly as the temperature of adsorption decreases. This suggests that the interactions between propylene and HKUST-1 are significantly reduced at higher temperatures.

Model adsorption isotherms were calculated from the virial parameters and plotted in Figure 4.32 for comparison to the experimental results.

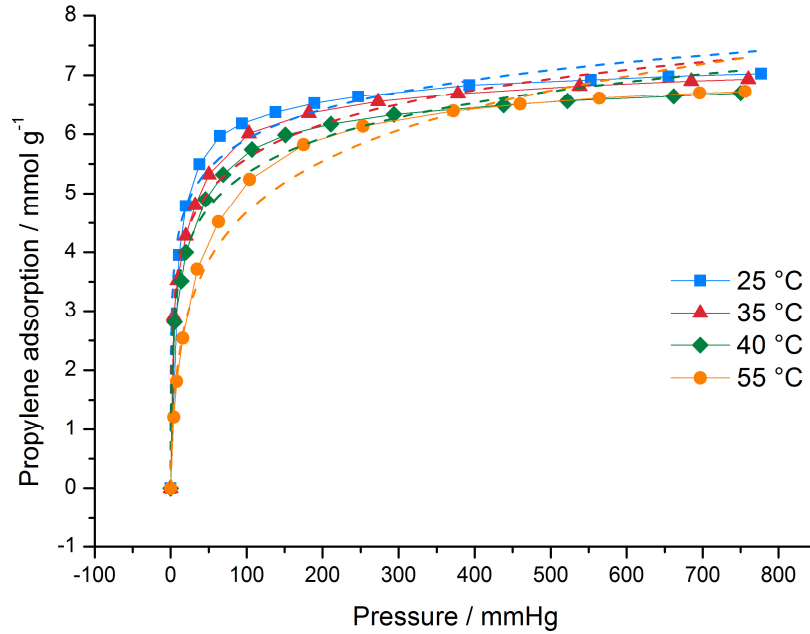


Figure 4.32: Adsorption isotherms for propylene on HKUST-1. Solid lines are experimental isotherms. Dashed lines are isotherms calculated from the virial parameters.

The calculated isotherms significantly underestimate propylene adsorption at low pressures and Figure 4.31 reveals that the data are not perfectly represented by single straight lines, particularly at coverages above  $6 \text{ mmol g}^{-1}$ . Adsorption of propylene seems to change the framework's capacity for further adsorption, possibly through contraction or expansion of the framework, and so two straight lines may better represent the real data.

The isotherms were treated in two sections; data points below  $6 \text{ mmol g}^{-1}$  coverage and data points above  $6 \text{ mmol g}^{-1}$  coverage. As before, virial plots and van't Hoff plots were produced (Figure 4.33).

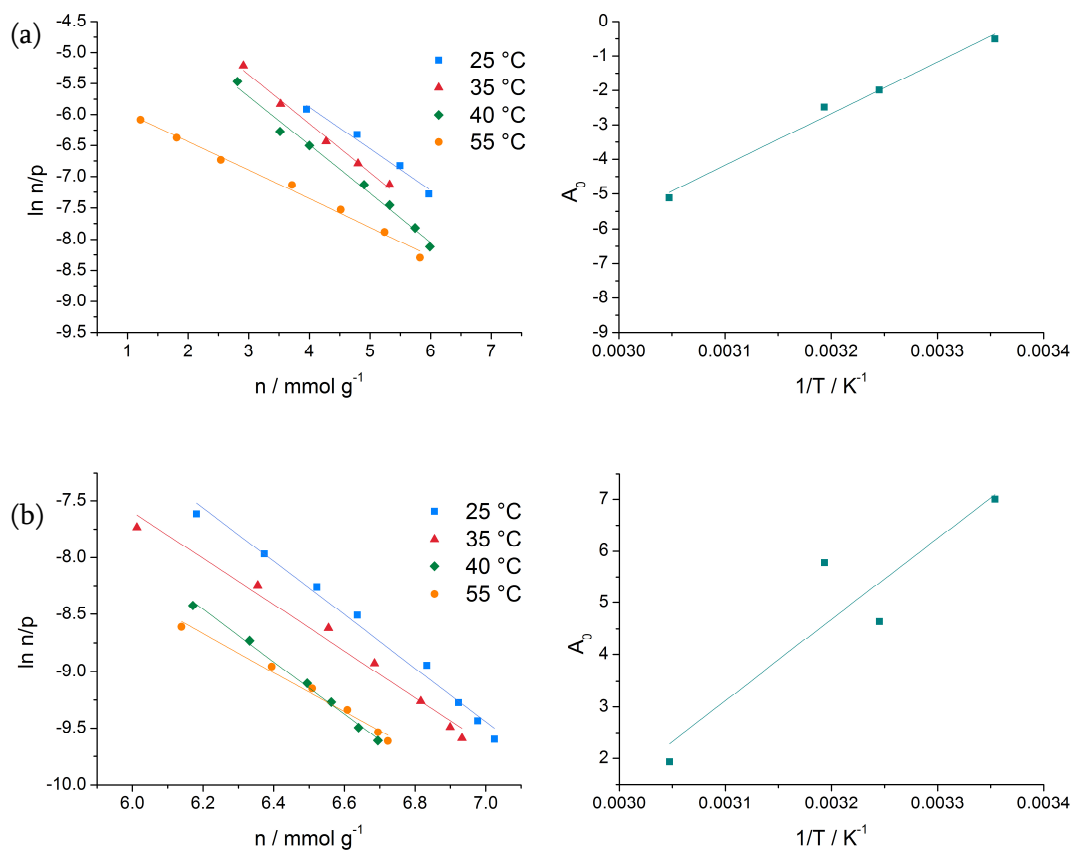


Figure 4.33: Virial plots (left) and van't Hoff plots (right) for propylene adsorption on HKUST-1, (a) below 6 mmol g<sup>-1</sup>; (b) above 6 mmol g<sup>-1</sup>.

Table 4.7: Henry's constants for adsorption of propylene below and above 50 mmHg on HKUST-1.

Temperature / °C	$K_H$ (below 50 mmHg) / mmol g <sup>-1</sup> kPa <sup>-1</sup>	$R^2$	$K_H$ (above 50 mmHg) / mmol g <sup>-1</sup> kPa <sup>-1</sup>	$R^2$
25	40.5 ± 8.9	0.977	1100000 ± 290000	0.989
35	50.5 ± 11.2	0.992	103000 ± 4400	0.984
40	34.4 ± 12.3	0.990	323000 ± 4000	0.996
55	3.99 ± 0.26	0.993	6920 ± 30	0.986

The isosteric enthalpy of adsorption was calculated to be 66.08 kJ mol<sup>-1</sup> ± 27.76 kJ mol<sup>-1</sup> below 6 mmol g<sup>-1</sup>, and 14.90 kJ mol<sup>-1</sup> ± 3.20 kJ mol<sup>-1</sup> above 6 mmol g<sup>-1</sup>, suggesting more interaction between propylene and HKUST-1 at lower coverages.

Henry's constant (Table 4.7) is higher at propylene coverages above  $6 \text{ mmol g}^{-1}$ , suggesting that gas molecules interact more with the framework surface at higher coverages. At high loading  $K_H$  is larger since a large amount of pressure must be applied to increase the loading further.

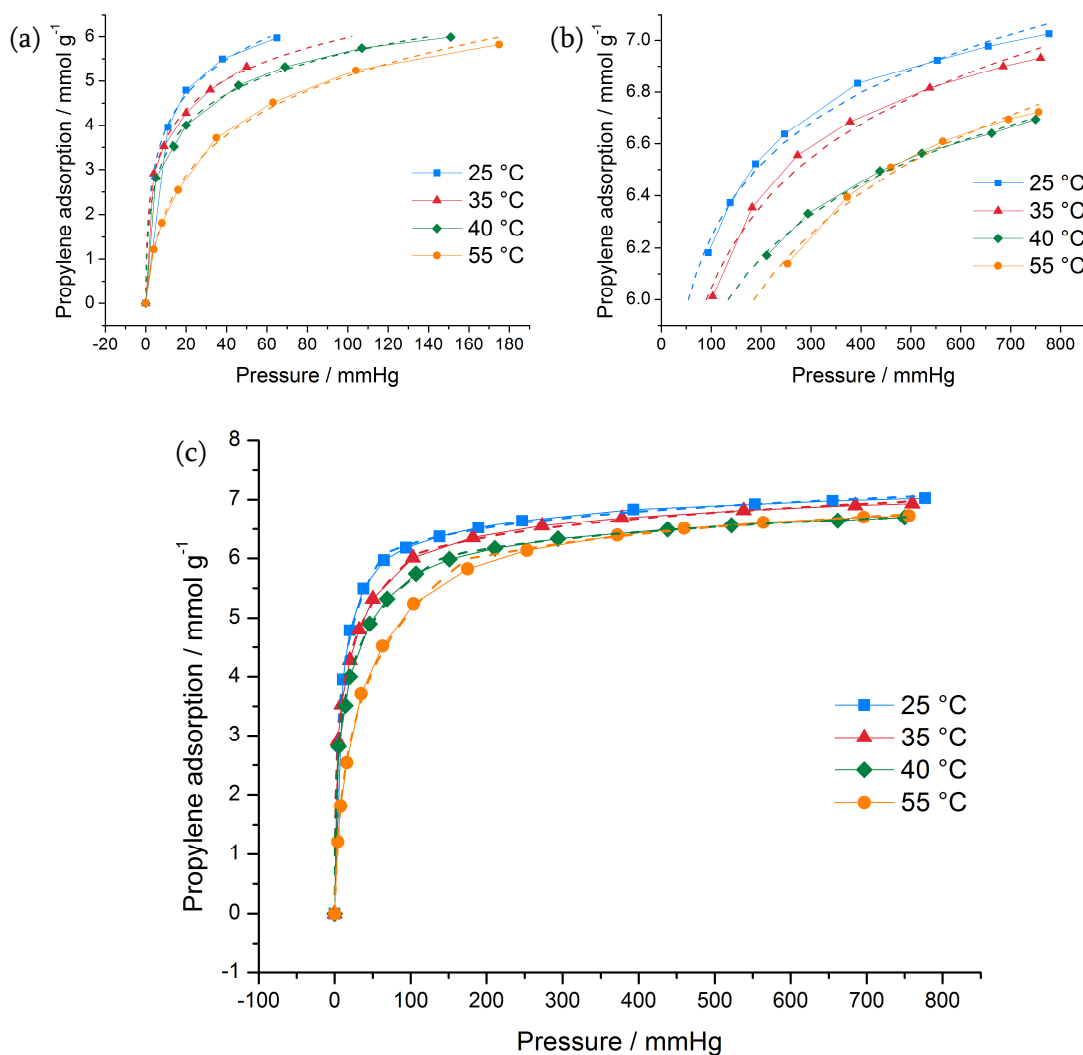


Figure 4.34: Adsorption isotherms for propylene on HKUST-1. (a) Below  $6 \text{ mmol g}^{-1}$ . Solid lines are experimental isotherms. Dashed lines are isotherms calculated from the virial parameters. (b) Above  $50 \text{ mmHg}$ . Solid lines are experimental isotherms. Dashed lines are isotherms calculated from the virial parameters. (c) Full isotherms. Solid lines are experimental isotherms. Dashed lines are isotherms calculated from the virial parameters.

The combined calculated isotherms in Figure 4.34(c) are much closer to the experimental results than the isotherms in Figure 4.32.  $R^2$  values are higher when the adsorption isotherms are treated as two straight lines. Therefore, the adsorption of propylene onto HKUST-1 is preferentially modelled by a two-step process. When

HKUST-1 has adsorbed  $6 \text{ mmol g}^{-1}$ , which equates to approximately one molecule of gas per metal site, the framework's capacity for further adsorption is reduced as evidenced by the lower  $q_{ST}$  values shown in Figure 4.30.

## 4.5 STAM-1 results

### 4.5.1 Ethylene

Gravimetric ethylene adsorption and desorption isotherms on STAM-1 were carried out at three temperatures:  $0 \text{ }^{\circ}\text{C}$ ,  $25 \text{ }^{\circ}\text{C}$  and  $40 \text{ }^{\circ}\text{C}$  (Figure 4.35). Some hysteresis is observed, suggesting that the adsorption of ethylene is not fully reversible.

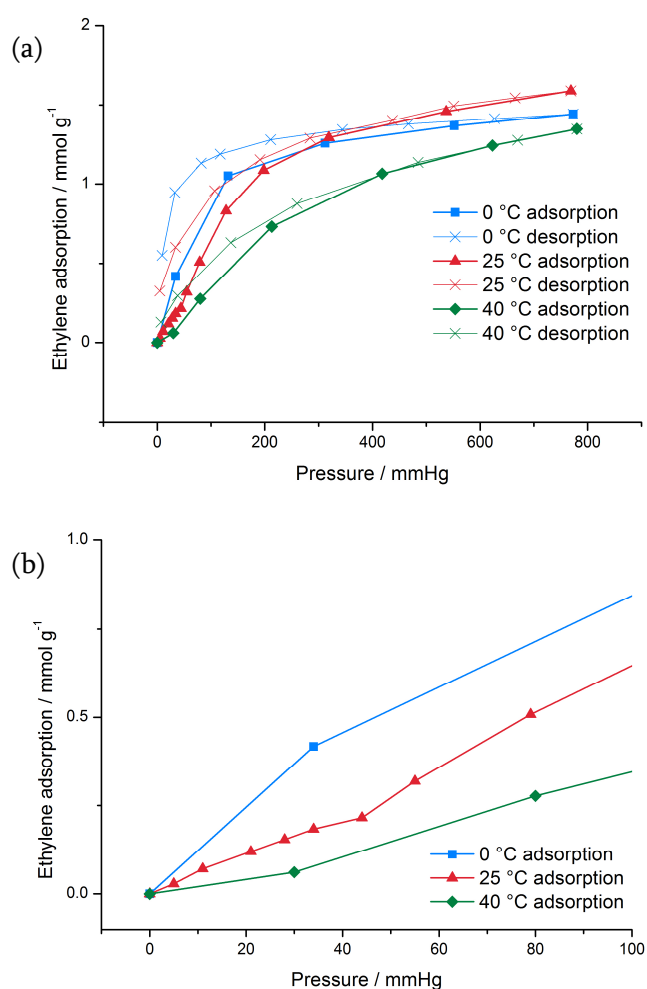


Figure 4.35: (a) Ethylene adsorption and desorption isotherms for STAM-1 at varying temperatures; (b) close up of ethylene adsorption on STAM-1 up to 100 mmHg.

Close inspection of the adsorption curves at 25 °C and 40 °C (Figure 4.35(b)) shows that ethylene adsorption occurs in two clear steps. This is similar to the results reported for hydrophilic gases.<sup>14</sup> The first step involves the adsorption of ethylene into the hydrophilic pores, lined with open copper sites. The interaction between ethylene and copper causes the hydrophobic, ester-lined pores to open, allowing a second step of adsorption. For this two-step process to occur, ethylene must interact directly with the metal sites.

## 4.5.2 Propylene

Gravimetric propylene adsorption and desorption isotherms on STAM-1 were carried out at three temperatures: 25 °C, 35 °C, 40 °C and 55 °C (Figure 4.36). Some hysteresis is observed, suggesting that the adsorption of ethylene is not fully reversible.

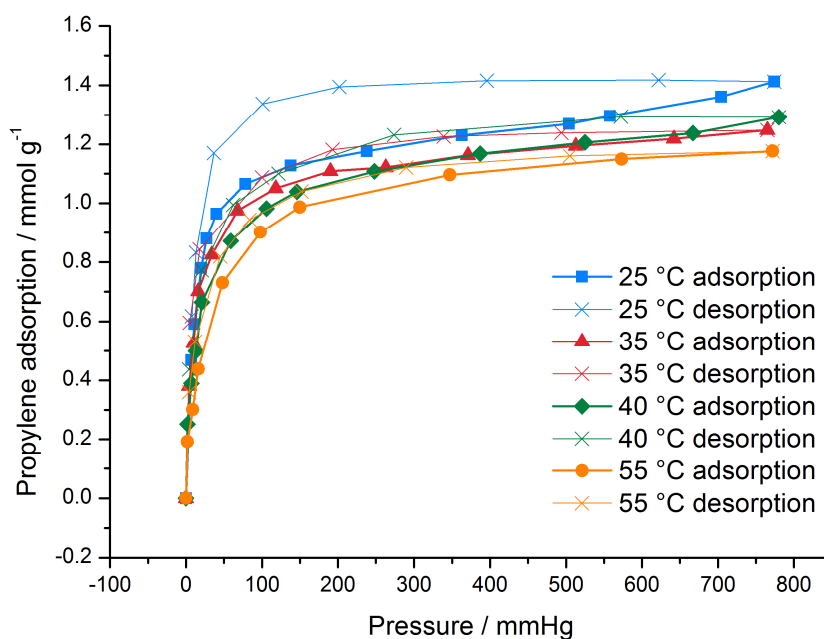


Figure 4.36: Propylene adsorption and desorption isotherms for STAM-1 at varying temperatures.

Initial propylene uptake is much steeper than for ethylene, suggesting that the interaction between propylene and STAM-1 is greater than that between ethylene and STAM-1 and both types of pores are filled. The two-step adsorption process is not observed in these isotherms. It is possible that propylene is adsorbed into the

hydrophilic pores at such low pressures that the hydrophobic pores open to allow adsorption at pressures lower than the first points on the isotherms.

#### 4.6 Comparisons

The propylene adsorption isotherms are steeper at low pressures than the ethylene isotherms (Figure 4.38) on both frameworks. However, at higher pressures ethylene adsorption on HKUST-1 at 25 °C exceeds propylene uptake. At low pressures, both frameworks would be expected to be selective for propylene adsorption. At pressures closer to room pressure, HKUST-1 may show reduced selectivity for propylene.

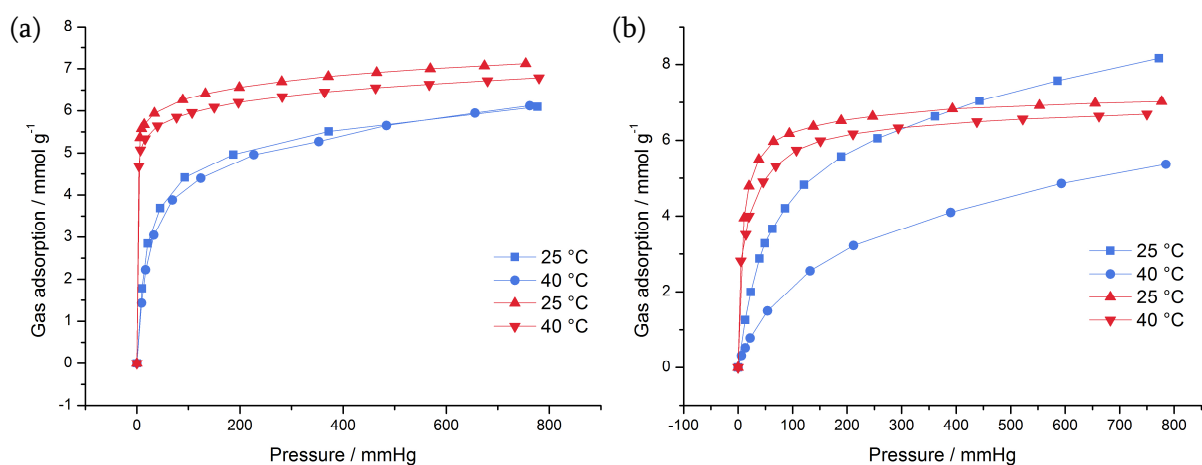


Figure 4.37: Ethylene (blue) and propylene (red) adsorption on (a) Ni-CPO-27 and (b) HKUST-1.

The slopes at the beginning of the ethylene adsorption isotherms are similar at 25 °C on the two frameworks. However, at higher pressures HKUST-1 adsorbs more ethylene than Ni-CPO-27 (Figure 4.38). At 40 °C, HKUST-1's affinity for ethylene adsorption is significantly lower than Ni-CPO-27's, particularly at lower pressures. The ethylene adsorption isotherms have not reached a plateau at any temperature or pressure investigated, suggesting that ethylene adsorption capacity may increase further at higher pressures. Propylene adsorption onto the two frameworks is similar throughout the temperature and pressure range investigated.

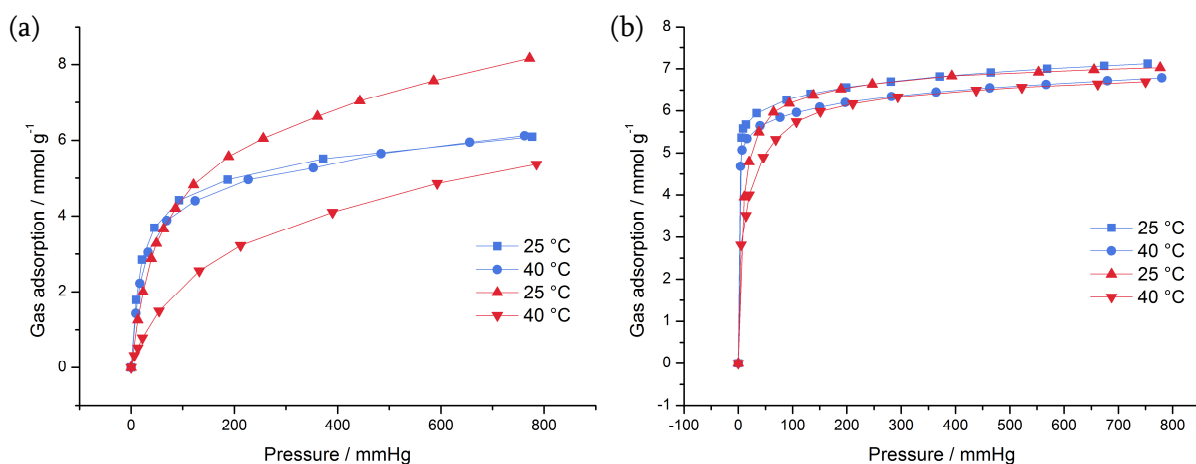


Figure 4.38: (a) Ethylene and (b) propylene adsorption on Ni-CPO-27 (blue) and HKUST-1 (red).

Isosteric heat of adsorption at zero coverage is much higher for propylene than ethylene on both frameworks (Table 4.8). This suggests that propylene adsorption occurs preferentially on both Ni-CPO-27 and HKUST-1.

Table 4.8: Isosteric heats of adsorption of ethylene and propylene at zero coverage on Ni-CPO-27 and HKUST-1.

Framework	$\Delta H_{\text{ethylene}} / \text{kJ mol}^{-1}$	$\Delta H_{\text{propylene}} / \text{kJ mol}^{-1}$
Ni-CPO-27	$57.79 \pm 5.80$	$125.96 \pm 17.45$
HKUST-1	$42.03 \pm 14.45$	$124.72 \pm 9.51$

## 4.7 Summary

Adsorption and desorption isotherms have been measured at various temperatures for ethylene and propylene on Ni-CPO-27 and HKUST-1. In some cases the data are best represented by two separate models, suggesting that the adsorption processes occur in two steps dependent on framework coverage or gas pressure. However, in other cases the data are better represented by a one-step adsorption process.

Where possible, isosteres were plotted to calculate the isosteric heat of adsorption at varying coverages. In all cases, the isosteric heat of adsorption initially increased slightly with coverage due to adsorbed olefin molecules encouraging further

adsorption through intermolecular interactions. In the case of ethylene on Ni-CPO-27, the isosteric heat of adsorption was found to fall after all open metal sites were occupied. On HKUST-1 the isosteric heat of adsorption could not be calculated for coverages higher than 100 % metal site occupancy; if isotherms could be measured at higher pressures and therefore higher coverages, it is possible that a similar reduction in isosteric heat of adsorption would be seen. Isosteric heats at varying coverage could not be calculated for propylene on Ni-CPO-27.

The isosteric heat of adsorption at zero coverage is significantly higher for propylene adsorption than ethylene adsorption on either framework, suggesting that both frameworks are selective for propylene over ethylene. The differences between frameworks are within the calculated errors and so are not significant. However, adsorption isotherms are different for each framework. Propylene adsorption has a steeper increase at low pressures on both frameworks and, in most cases, a higher coverage overall. However, ethylene adsorption at 25 °C on HKUST-1 outperforms propylene at higher pressures. Ethylene adsorption on HKUST-1 at 40 °C is significantly lower than propylene adsorption at all pressures investigated, suggesting that HKUST-1 at 40 °C will show the highest selectivities for propylene over ethylene.

Two-step adsorption isotherms were observed for ethylene adsorption on STAM-1, where the uptake of ethylene onto the copper sites in the hydrophilic pores caused the hydrophobic pores to open and allow the adsorption of more gas. Ethylene interacts directly with the open metal sites in STAM-1. The similarities between STAM-1 and HKUST-1 suggest that a similar ethylene-metal interaction occurs during adsorption on HKUST-1, and it seems likely that the same process also occurs on the open nickel sites in Ni-CPO-27.

#### **4.8 References**

1. P. D. C. Dietzel, Y. Morita, R. Blom, and H. Fjellvåg, *Angew. Chem. Int. Ed.*, 2005, **44**, 6354–6358.
2. P. D. C. Dietzel, B. Panella, M. Hirscher, R. Blom, and H. Fjellvåg, *Chem. Commun.*, 2006, 959.
3. P. D. C. Dietzel, R. Blom, and H. Fjellvåg, *Eur. J. Inorg. Chem.*, 2008, **2008**, 3624–3632.

4. P. D. C. Dietzel, R. E. Johnsen, R. Blom, and H. Fjellvåg, *Chem. Eur. J.*, 2008, **14**, 2389–2397.
5. M. Märcz, R. E. Johnsen, P. D. C. Dietzel, and H. Fjellvåg, *Microporous Mesoporous Mater.*, 2012, **157**, 62–74.
6. N. L. Rosi, J. Kim, M. Eddaoudi, B. Chen, M. O’Keeffe, and O. M. Yaghi, *J. Am. Chem. Soc.*, 2005, **127**, 1504–1518.
7. E. J. García, J. P. S. Mowat, P. A. Wright, J. Pérez-Pellitero, C. Jallut, and G. D. Pirngruber, *J. Phys. Chem. C*, 2012, **116**, 26636–26648.
8. E. D. Bloch, W. L. Queen, R. Krishna, J. M. Zadrozny, C. M. Brown, and J. R. Long, *Science*, 2012, **335**, 1606–1610.
9. A. J. Matzger, A. G. Wong-Foy, and S. Caskey (The University of Michigan, USA). Microporous Coordination Polymers as Novel Sorbents for Gas Separation. US Patent 073739, June 11, 2009.
10. S. S. Chui, S. M. Lo, J. P. H. Charmant, A. G. Orpen and I. D. Williams, *Science*, 1999, **283**, 1148–1150.
11. Q. Min Wang, D. Shen, M. Bülow, M. L. Lau, S. Deng, F. R. Fitch, N. O. Lemcoff, and J. Semanscin, *Microporous Mesoporous Mater.*, 2002, **55**, 217–230.
12. T. M. Nicholson and S. K. Bhatia, *J. Phys. Chem. B*, 2006, **110**, 24834–24836.
13. S. Wang, Q. Yang, and C. Zhong, *Sep. Purif. Technol.*, 2008, **60**, 30–35.
14. M. I. H. Mohideen, B. Xiao, P. S. Wheatley, A. C. McKinlay, Y. Li, A. M. Z. Slawin, D. W. Aldous, N. F. Cessford, T. Düren, X. Zhao, R. Gill, K. M. Thomas, J. M. Griffin, S. E. Ashbrook, and R. E. Morris, *Nat. Chem.*, 2011, **3**, 304–310.
15. A. C. McKinlay. New Nitric Oxide Releasing Materials. PhD Thesis, University of St Andrews, 2010.

## CHAPTER 5: Olefin separation using coordinatively unsaturated MOFs

### 5.1 Aims

Ideal adsorbed solution theory will be used to predict the abilities of Ni-CPO-27 and HKUST-1 to separate binary mixtures of ethylene and propylene by calculating their selectivities based upon the pure adsorption isotherms reported in Chapter 4. The selectivities will be compared for each framework at two different temperatures and for three different ethylene/propylene mixtures.

In order for industrial adsorptive separation to be economically and energetically viable, the desorption process must also be understood. To this end, temperature programmed desorption experiments will be performed for ethylene on Ni-CPO-27 and HKUST-1 at different ramp rates, allowing the calculation of their respective enthalpies of desorption.

### 5.2 Ideal adsorbed solution theory

The ideal adsorbed solution theory (IAST) can be used to predict competitive adsorption of different gases onto solid supports, and has been used successfully with a number of MOFs.<sup>1,2</sup>

The IAST assumes that the gas surrounding a solid exerts a spreading pressure,  $\pi$ . This spreading pressure can be calculated from the experimental adsorption isotherm using the Gibbs adsorption isotherm, equation (5.1), where  $c$  is the concentration of the adsorbed gas, or gas coverage ( $\text{mol L}^{-1}$ ),  $c_{eq}$  is the concentration of the adsorbed gas at equilibrium,  $R$  is the universal gas constant and  $\Gamma$  is the density of the adsorbed gas ( $\text{mol m}^{-1}$ ). The area under a plot of  $c$  vs.  $\frac{\Gamma}{c}$  is equal to  $\frac{\pi}{RT}$ .<sup>3</sup>

$$\pi = RT \int_0^{c_{eq}} \frac{\Gamma}{c} dc \quad (5.1)$$

A plot of pressure against  $\pi$  for each adsorption isotherm allows the calculation of  $P^o$ , the equilibrium pressure required to exert the spreading pressure.<sup>4</sup>

The total pressure for a 1: $m$  mixture is calculated using equation (5.2).<sup>2</sup>

$$P = \frac{(m+1)P_i^o P_j^o}{P_i^o + mP_j^o} \quad (5.2)$$

Selectivity for the adsorption of gas  $i$  over gas  $j$ , termed  $S_{i,j}$ , can be calculated using equation (5.3). If  $S_{i,j}$  is greater than 1, then component  $i$  is preferentially adsorbed.

$$S_{i,j} = \frac{P_j^o}{P_i^o} \quad (5.3)$$

### 5.2.1 Ni-CPO-27

The spreading pressure,  $\pi$ , was calculated from experimental isotherms at 25 °C and 40 °C for both ethylene and propylene adsorption (Figure 5.1).

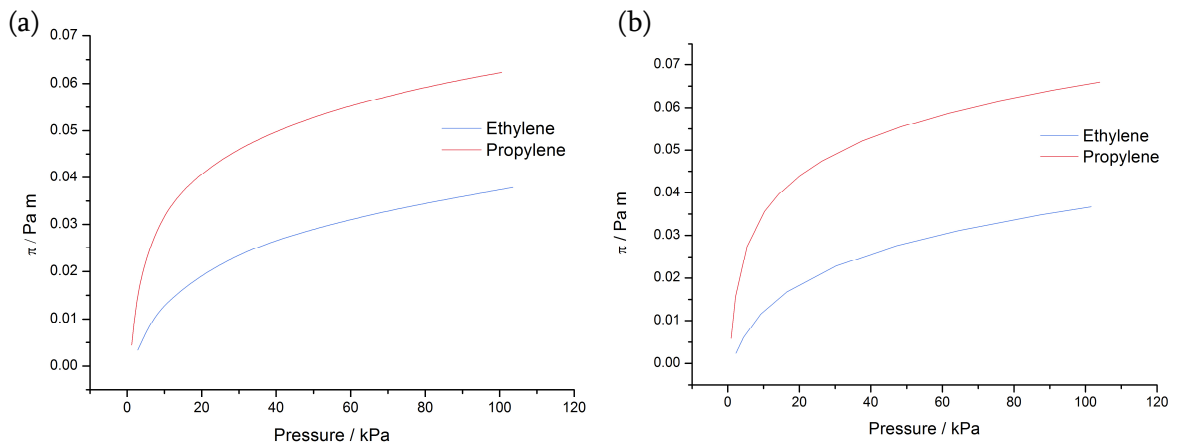


Figure 5.1: Spreading pressure of ethylene and propylene on Ni-CPO-27 at (a) 25 °C and (b) 40 °C.

Selectivity was calculated for propylene/ethylene mixtures with the ratios 1:1, 1:2 and 1:99 (Figure 5.2).

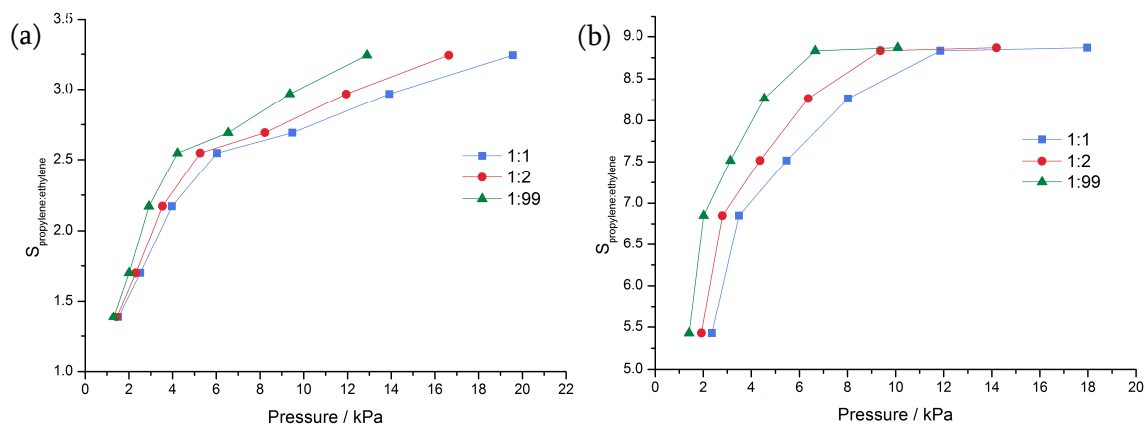


Figure 5.2: Calculated selectivity for propylene over ethylene at varying mixture compositions for Ni-CPO-27 at (a) 25 °C and (b) 40 °C.

Ni-CPO-27 is selective for propylene over ethylene and selectivity is greater at higher pressures. At the temperatures and pressures investigated, selectivity is greater at higher temperature. In both cases, the higher the percentage of ethylene in the gas mixture, the better the framework's selectivity. At 25 °C, selectivity increases up to atmospheric pressure and this increase may continue at higher pressures, yet at 40 °C the increase in selectivity plateaus at approximately 12 kPa for all gas mixtures.

### 5.2.2 HKUST-1

The spreading pressure was calculated from experimental isotherms at 25 °C and 40 °C for both ethylene and propylene adsorption (Figure 5.3).

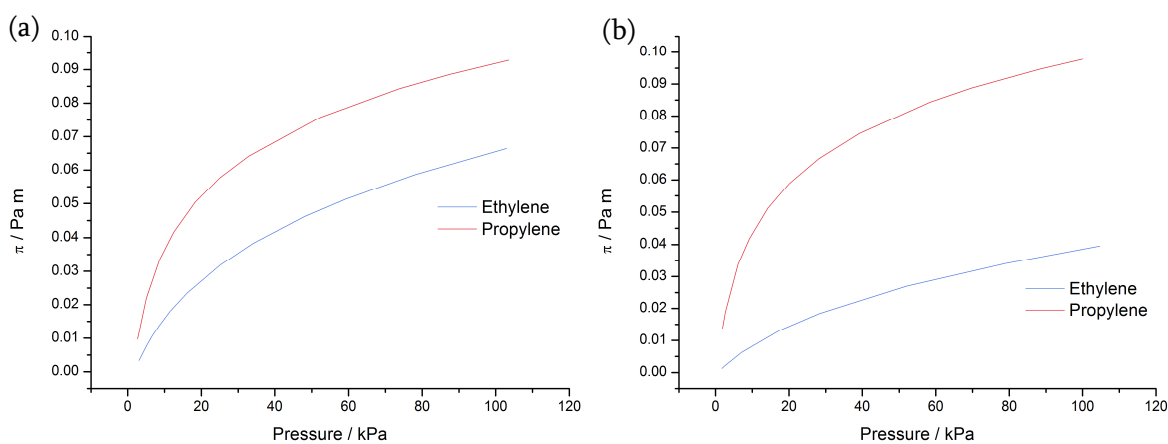


Figure 5.3: Spreading pressure of ethylene and propylene on Ni-CPO-27 at (a) 25 °C and (b) 40 °C.

Selectivity was calculated for propylene/ethylene mixtures with the ratios 1:1, 1:2 and 1:99 (Figure 5.4).

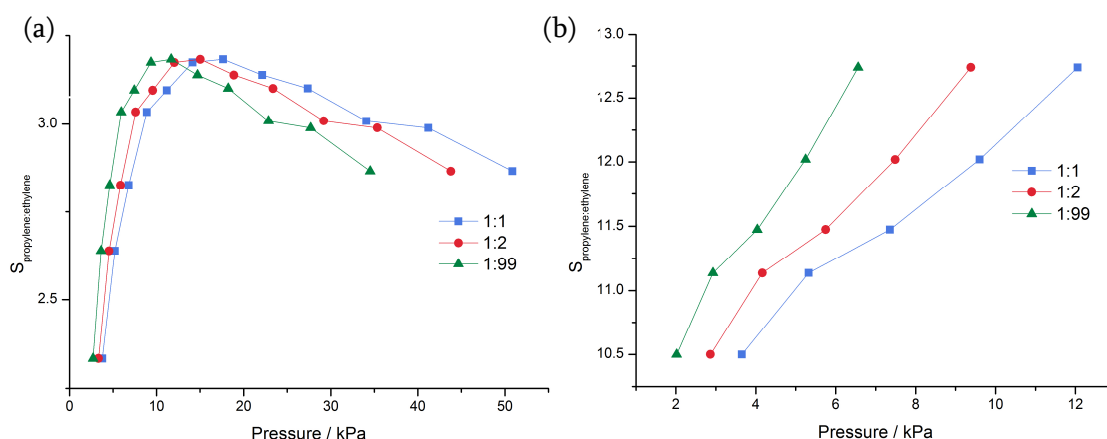


Figure 5.4: Calculated selectivity for propylene over ethylene at varying mixture compositions for HKUST-1 at (a) 25 °C and (b) 40 °C.

At the pressures investigated, separation of a propylene/ethylene mixture using HKUST-1 is significantly more selective at 40 °C than at 25 °C. At pressures up to 10 kPa, separation of a mixture with a higher ethylene percentage is more selective than with a lower ethylene percentage. Up to this low pressure, selectivity of HKUST-1 increases with increasing pressure at both temperatures.

For a binary mixture of ethylene and propylene on HKUST-1 at 25 °C, selectivity increases initially up to a maximum of approximately 3.2 for all three

coverages, before decreasing slowly. At this point, separation of a mixture with a lower ethylene percentage becomes more selective.

### 5.2.3 Comparisons

Both frameworks are selective for propylene over ethylene at all temperatures and pressures investigated. Interactions between the frameworks and propylene molecules are greater, as evidenced by the higher enthalpies of adsorption at zero coverage for propylene (Table 4.8).

Both Ni-CPO-27 and HKUST-1 were more selective for propylene in an ethylene:propylene mixture at 40 °C than at 25 °C. For a 1:1 mixture, Ni-CPO-27 and HKUST-1 achieved maximum selectivities of 8.9 at 18.0 kPa and 12.7 at 12.1 kPa respectively.

At pressures of approximately 12 kPa for both frameworks with a 1:1 mixture at 40 °C, Ni-CPO-27 had a selectivity of 8.8 and HKUST-1 had a selectivity of 12.7. Examination of the ethylene and propylene adsorption isotherms as shown in Figure 4.36 shows that the difference in ethylene and propylene adsorption capacities is greatest for HKUST-1 at 40 °C; while HKUST-1 has a high affinity for propylene at all temperatures, its affinity for ethylene is greatly reduced at higher temperatures. Under the conditions tested, propylene capture from a propylene/ethylene mixture would be most selective using an HKUST-1 support at 40 °C.

Examination of the adsorption isotherms side-by-side, as shown in Figure 4.37, reveals that at 25 °C both frameworks adsorb similar amounts of propylene but Ni-CPO-27 adsorbs considerably less ethylene than HKUST-1. This evidence suggests that, at 25 °C Ni-CPO-27 may have a higher propylene selectivity. In fact, Figure 5.5 shows that the selectivity of the two frameworks is very similar at the pressures investigated, but experiments under higher pressures may reveal the predicted differences.

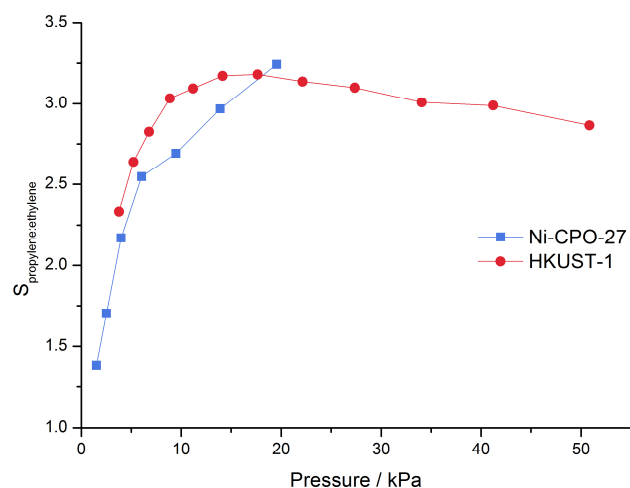


Figure 5.5: Calculated selectivity for propylene over ethylene at 25 °C on Ni-CPO-27 and HKUST-1.

## 5.3 Desorption

### 5.3.1 Ni-CPO-27

Temperature programmed desorption (TPD) was carried out for Ni-CPO-27 at ramp rates ranging from 0.5 to 5 °C min<sup>-1</sup> (Figure 5.6).

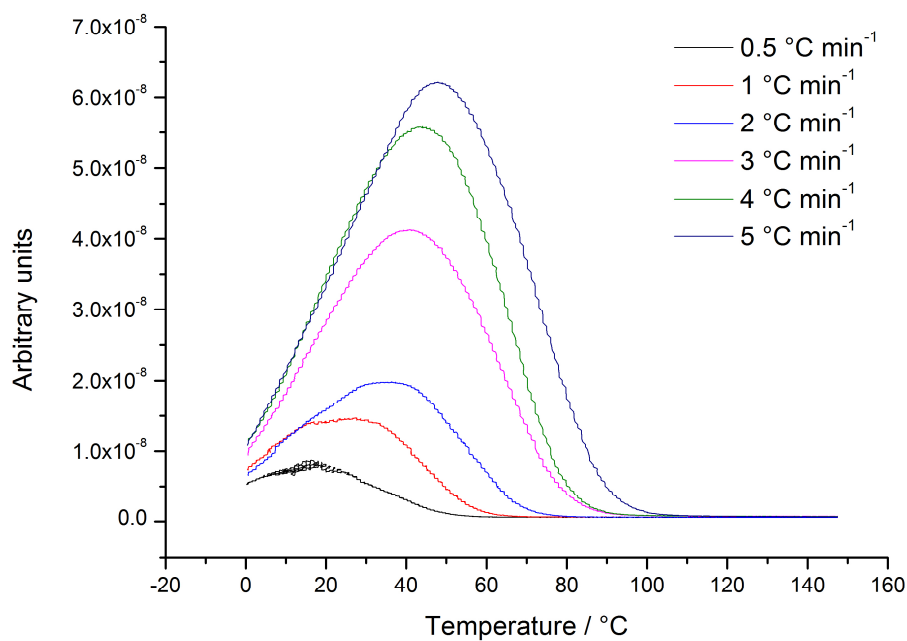


Figure 5.6: TPD spectra for ethylene on Ni-CPO-27 at varying ramp rates.

As the ramp rate increases, the peak temperature increases. The positions of the peak maxima can be used to calculate the enthalpy of desorption using two different methods; Redhead's equation and the heating rate variation technique.

Redhead's equation allows the calculation of the enthalpy of desorption based upon just one TPD curve. As such,  $E_d$  was calculated for each ramp rate (Table 5.1).

Table 5.1: Enthalpy of desorption for ethylene on Ni-CPO-27, calculated using Redhead's equation.

Ramp rate / °C min <sup>-1</sup>	$E_d$ / kJ mol <sup>-1</sup>
0.5	77.30
1	77.97
2	79.31
3	79.50
4	79.53
5	79.94

Using Redhead's method, the enthalpy of desorption increases slightly as the ramp rate is increased. This suggests that the assumptions made in the application of the Redhead equation, such as the pre-exponential factor, do not accurately represent the system.

The heating rate variation method uses TPD curves measured at different ramp rates to produce Figure 5.7. The enthalpy of desorption is  $50.35 \pm 1.89$  kJ mol<sup>-1</sup>.

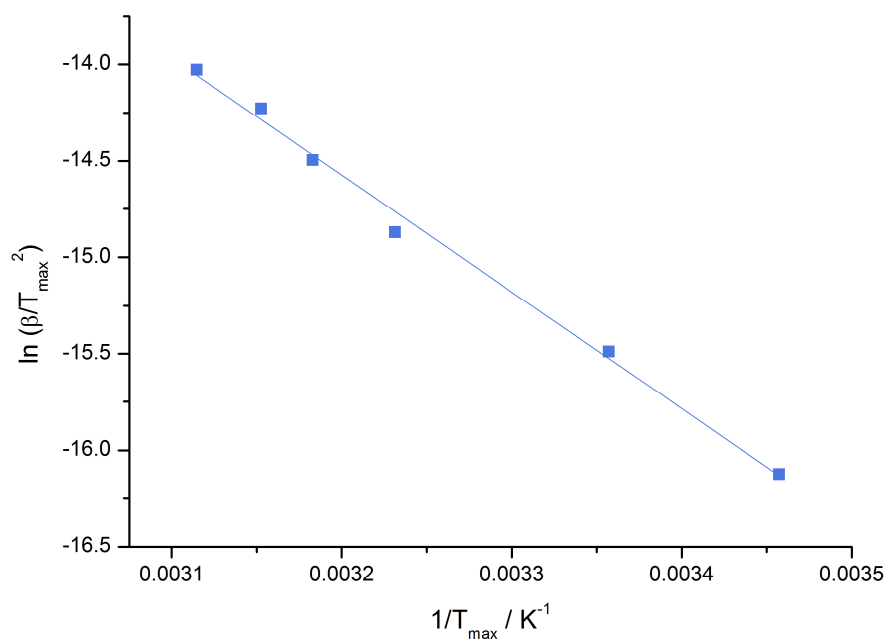


Figure 5.7: Heating rate variation method for calculating the enthalpy of desorption of

ethylene from Ni-CPO-27. The gradient is equal to  $\frac{E_d}{R}$ .

The isosteric heat of adsorption at zero coverage for ethylene on Ni-CPO-27, as calculated in Chapter 4, was  $57.79 \pm 5.80 \text{ kJ mol}^{-1}$ . This is very similar to the enthalpy of desorption, although the error on the adsorption enthalpy is too large to allow meaningful comparisons.  $E_d$  is low, however, and desorption of ethylene from Ni-CPO-27 occurs at low temperatures, therefore reactivation of the substrate after a separation procedure would only require mild heat treatment.

The enthalpy of desorption obtained from the heating rate variation method was used to calculate the pre-exponential factor using Redhead's equation (Table 5.2).  $A$  is related to the frequency of the copper-ethylene bond and so would be expected to be of an order of magnitude between  $10^{11}$  and  $10^{15} \text{ s}^{-1}$ .<sup>5</sup> The values obtained here are significantly smaller due to the slow diffusion of ethylene from the framework pores, termed diffusional resistance, readsorption effects where less readsorption occurs at higher flow rates, or due to a combination of the two.<sup>6</sup>

Table 5.2: Pre-exponential factor,  $A$ , for ethylene on Ni-CPO-27 calculated using Redhead's equation.

Ramp rate / °C min <sup>-1</sup>	$A$ / s <sup>-1</sup>
1	1358024
2	1437572
3	1292311
4	1424023
5	1565449

### 5.3.2 HKUST-1

TPD was carried out on HKUST-1 at ramp rates ranging from 2 to 20 °C min<sup>-1</sup> (Figure 5.8).

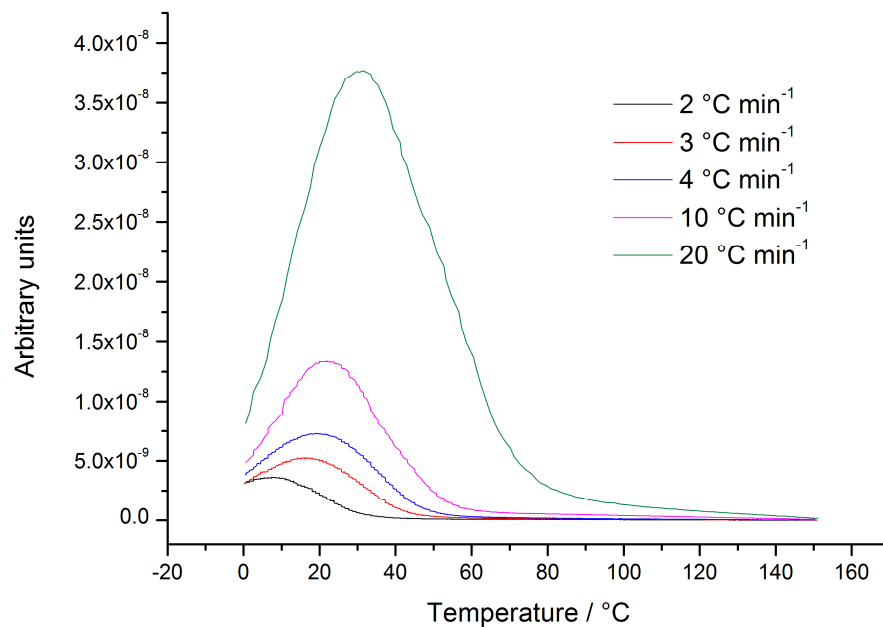


Figure 5.8: TPD spectra for ethylene on HKUST-1 at varying ramp rates.

Using Redhead's equation,  $E_d$  was calculated for each ramp rate (Table 5.3).

Table 5.3: Enthalpy of desorption for ethylene on HKUST-1, calculated using Redhead's equation.

<b>Ramp rate</b> <b>/ °C min<sup>-1</sup></b>	<b><math>E_d</math> / kJ mol<sup>-1</sup></b>
2	71.67
3	72.98
4	73.03
10	71.55
20	72.22

The enthalpy of desorption is not consistent throughout the range of ramp rates. This suggests that the assumptions made in the application of the Redhead equation, such as the pre-exponential factor, do not accurately represent the system.

The heating rate variation method uses TPD curves measured at different ramp rates to produce Figure 5.9. The enthalpy of desorption is  $34.00 \pm 13.46$  kJ mol<sup>-1</sup>.

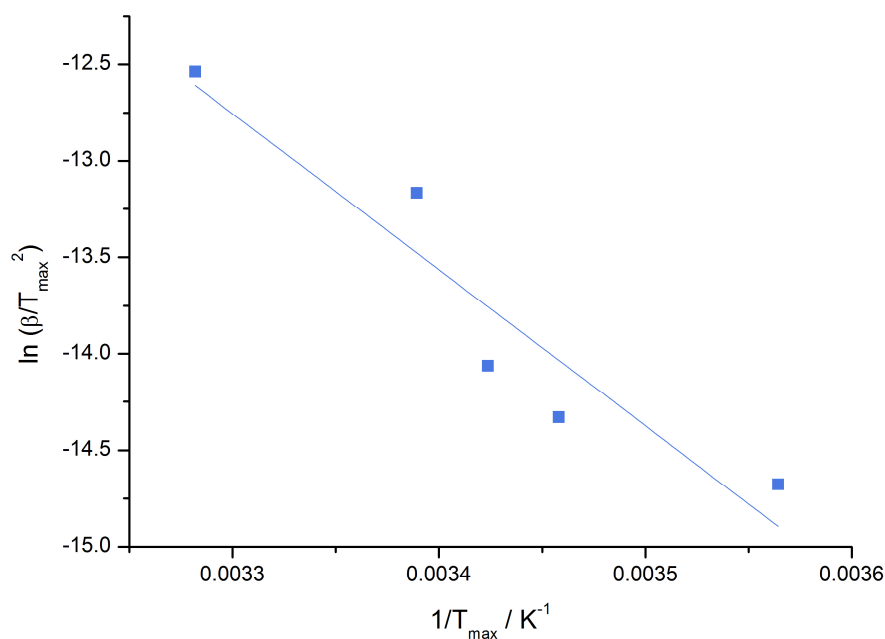


Figure 5.9 : Heating rate variation method for calculating the enthalpy of desorption of ethylene from HKUST-1.

The isosteric heat of adsorption at zero coverage for ethylene on HKUST-1, as calculated in Chapter 4, was  $42.03 \pm 14.45 \text{ kJ mol}^{-1}$ . This is very similar to the enthalpy of desorption, although the error on the adsorption and desorption enthalpies are too large to allow meaningful comparisons.  $E_d$  is low, however, and desorption of ethylene from HKUST-1 occurs at low temperatures, therefore reactivation of the substrate after a separation procedure would only require mild heat treatment.

The enthalpy of desorption obtained from the heating rate variation method was used to calculate the pre-exponential factor using Redhead's equation (Table 5.4). The values obtained here are significantly smaller than expected due to diffusional resistance, readsorption effects, or a combination of the two.<sup>6</sup> The pre-exponential factor is consistently lower for ethylene desorption from HKUST-1 than Ni-CPO-27, suggesting that diffusional resistance and/or readsorption effects are greater for HKUST-1 than for Ni-CPO-27.

Table 5.4: Pre-exponential factor,  $A$ , for ethylene on HKUST-1 calculated using Redhead's equation.

Ramp rate / °C min <sup>-1</sup>	$A$ / s <sup>-1</sup>
2	2248
3	2724
4	3179
10	6442
20	12349

#### 5.4 Summary and further work

Desorption of ethylene from Ni-CPO-27 and HKUST-1 has been measured using TPD at a range of ramp rates. Redhead's method and the heating rate variation method were both used to calculate the enthalpy of desorption,  $E_d$ , and the heating rate variation method was found to better represent the data. Enthalpy of desorption is very similar to the isosteric heat of adsorption at zero coverage for both frameworks. The low values of  $E_d$  along with the low temperatures at which desorption was observed during the TPD experiments suggest that reactivation of the frameworks after a separation procedure would only require mild heating under vacuum or an inert gas.

In order to fully understand the proposed propylene/ethylene separation process, TPD experiments for propylene on Ni-CPO-27 and HKUST-1 would be extremely useful; the higher isosteric heats of adsorption for propylene on the frameworks would suggest that its desorption would take place at higher temperatures and provide a higher enthalpy of desorption.

Ideal adsorbed solution theory was used to calculate the selectivities of propylene/ethylene separation at two different temperatures and at a range of gas mixture compositions. Both frameworks were selective for propylene over ethylene,

as evidenced by  $S_{\text{propylene:ethylene}}$  values greater than 1. Similarly, both frameworks showed higher selectivities at 40 °C than at 25 °C. Selectivities were greater at lower pressures for a 99 % ethylene/propylene mixture than for a 50 % mixture. The highest selectivity for the conditions studied with the IAST was for HKUST-1 at 40 °C, with a selectivity of 12.7.

The selectivity of HKUST-1 for propylene over ethylene at 40 °C increases with increasing pressure, but does not reach a maximum at the pressures investigated. The same is true for Ni-CPO-27 at 25 °C, and possibly at 40 °C. It is likely that increased pressures could provide higher selectivities for propylene over ethylene. In order to investigate this further, pure gas adsorption isotherms would have to be performed up to higher pressures. The investigation of propylene/ethylene separation would be best carried out by performing experimental separations, allowing the comparison of simulated selectivities with those achieved experimentally.

## **5.5 References**

1. B. Liu and B. Smit, *Langmuir*, 2009, **25**, 5918–5926.
2. J. M. Simmons, H. Wu, W. Zhou, and T. Yildirim, *Energy & Environmental Science*, 2011, **4**, 2177.
3. M. M. Benjamin, *Environ. Sci. Technol.*, 2009, **43**, 2530–2536.
4. A. L. Myers and J. M. Prausnitz, *AIChE Journal*, 1965, **11**, 121–127.
5. R. Zacharia. Desorption of gases from graphitic and porous carbon surfaces. PhD Thesis, Free University of Berlin, 2010.
6. A. Palermo and C. . Aldao, *Thermochim. Acta*, 1998, **319**, 177–184.

## CHAPTER 6: Development of a static gas cell for *in situ* single crystal X-ray diffraction

### 6.1 Declaration

Gas cell experiments in Chapter 6 and Chapter 7 were carried out in collaboration with Dr Phoebe Allan, a PhD student also supervised by Professor Russell Morris. Catherine Renouf and Phoebe Allan contributed equally to the work, and some of the results appeared in Dr Allan's thesis in 2012.<sup>1</sup>

### 6.2 Introduction

Early gas cells for powder X-ray diffraction allowed the flow of a gas over a disc of sample. Catalytic experiments could be carried out where the gas was analysed on exit by mass spectrometry or gas chromatography, so the progress of a reaction could be followed with respect to changes in the sample's powder pattern. Flow cells such as this were not transparent to visible light, so centring a sample was a lengthy process that used the strongest reflection of a known phase within the sample. Thermal expansion of components within the gas cells coupled with this difficulty in centring produced errors that had to be compensated for mathematically. Interesting results were reported where, for example, the progress of a reaction could be followed by monitoring peak heights of reactants and products within the sample. Limitations, however, included the fact that these gas cells could not be used at pressures above or below ambient and that X-rays had to pass twice through three different materials before detection.<sup>2</sup>

A more recent example of a gas cell used in powder X-ray diffraction was developed at the European Synchrotron Radiation Facility (ESRF) in Grenoble.<sup>3</sup> This gas cell used quartz capillaries and so reactions could be visually inspected throughout the experimental process. Gases could be condensed *in situ* with experiments run at pressures up to 7 bar and at temperatures as low as 60 K. The design of the cell meant that the gas line could be disconnected after gas loading to allow the capillary to spin

on the diffractometer, or it could be left connected and the capillary oscillated if the experiment required changes in gas pressure.<sup>3</sup>

Gas cells for the study of single protein crystals developed alongside small molecule powder techniques. An early example from 1994 employed a dilution valve for the dosing of gases into the cell. Crystal structures of partially oxygenated haemoglobin were successfully determined, but the design meant that experiments could only be carried out at room temperature and the exact partial pressure inside the cell had to be determined by extrapolation from an experimentally determined titration curve.<sup>4</sup> By 1996 a gas cell had been developed that used commercially available capillaries and allowed samples to be mounted as quickly and easily as for more routine protein crystallography experiments. This gas cell could maintain a pressure of up to 20 bar for 48 hours.<sup>5</sup>

Gas cells for use in small molecule single crystallography were developed at a relatively late stage; a gas cell that could withstand pressures up to 1000 bar of gas or liquid was reported in 2005. The use of quartz capillaries meant that the crystal could easily be centred on the diffractometer, although it did create a significant halo in the diffraction frames. An experiment using 200 bar of water and another using 400 bar of nitrogen were successfully carried out. However, the pressure within the gas cell itself could not be monitored leading to ambiguity in any results obtained, and the cell had to be sealed and disconnected from the gas line before data collection. This was not a problem for experiments conducted under pressure, but is a serious limitation for *in situ* adsorption experiments as pressures could not be changed after removal of the gas line.<sup>6</sup>

### **6.2.1 SRS, beamline 9.8**

In 2009, Warren et al. reported a gas cell designed specifically for the study of single crystals in different gaseous environments. The cell was designed for use on beamline 9.8 at the Synchrotron Radiation Source (SRS) in Daresbury, and is now used on beamline I19 at Diamond. Many components of the cell can be easily replaced such as the Nalgene tubing for the gas inlet/outlet and the borosilicate or quartz capillaries used for the cell body. The use of transparent capillaries also makes it easy to centre the cell in the X-ray beam and visually inspect the sample throughout the experiment.

The cell can be used in flow configuration or static configuration, and a dynamic vacuum can also be applied. It has been tested with hydrogen chloride and sulphur dioxide gases, and a successful experiment has been reported where a crystal was heated under vacuum and then exposed to a sulphur dioxide and argon mixture.<sup>7</sup>

This environmental gas cell was used by Dr Peter Byrne for the study of SO<sub>2</sub> and NO adsorption on Co-CPO-27.<sup>8</sup> Dehydration of the framework was carried out under dynamic vacuum at 90-100 °C, and the occupancy of the metal site by water molecules was reduced to a minimum of 35 %. Following exposure to NO, this high water occupancy made it difficult to confidently locate adsorbed NO molecules (as discussed in detail in Chapter 7). Moreover, the high level of hydration prevented the study of gaseous species that form weak bonds with the cobalt sites.

## 6.2.2 Co-CPO-27

Co-CPO-27 (Figure 6.1) was selected for single crystal X-ray diffraction experiments because it readily forms single crystals up to 100 μm in size. Dehydration of the framework was studied crystallographically by Dietzel et al. using single crystals in a hot nitrogen stream and it was shown to retain crystallinity throughout the dehydration process.<sup>9</sup>

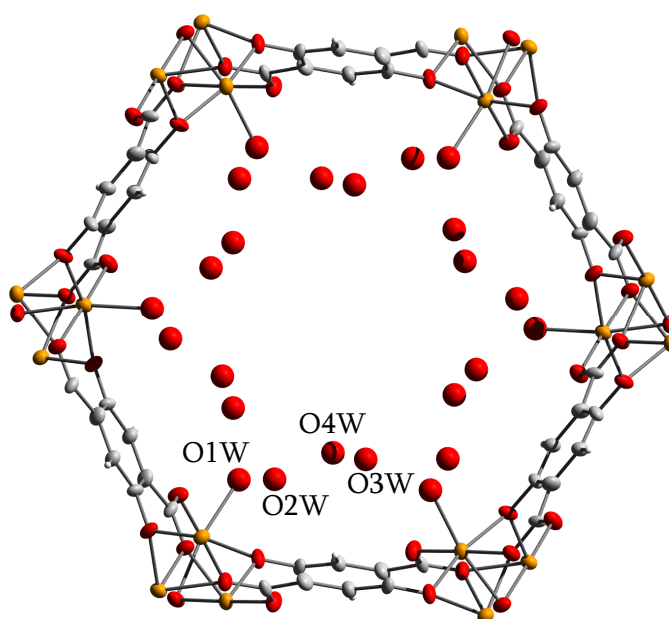


Figure 6.1: Hydrated Co-CPO-27, with coordinated (O1W) and non-coordinated (O2W, O3W and O4W) water molecules. Cobalt atoms shown in orange, oxygen in red and carbon in grey.

### 6.2.3 HKUST-1

HKUST-1 crystals are large enough to be used for single crystal X-ray diffraction experiments<sup>10</sup> but are often twinned so careful crystal picking and screening is crucial. Dehydration of the framework has not previously been studied using single crystal X-ray diffraction.

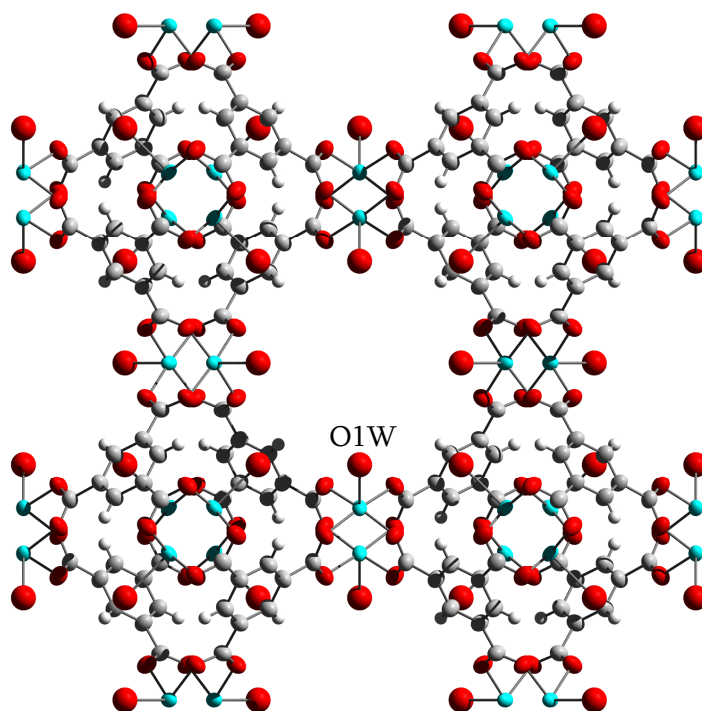


Figure 6.2: Hydrated HKUST-1, with coordinated water molecules (O1W). Copper atoms shown in turquoise, oxygen in red and carbon in grey.

### 6.3 ALS beamline 11.3.1

The static gas cell used for all gas cell experiments discussed here was developed on beamline 11.3.1 at the Advanced Light Source (ALS) at the Lawrence Berkeley National Laboratory in Berkeley, California. Alongside the gas cell itself, a corresponding gas handling system was developed in order to enable a range of experimental conditions to be tested.

The gas cell (Figure 6.3) consists of a standard goniometer head with a glass attachment on top, soldered into a metal base which is then placed on top of the goniometer head and sealed with a lightly greased O-ring and a metal screw loop. The glass gas cell head enables the crystal to be visually inspected; in many

experiments crystal colour is an important indicator of the progress of an experiment, but this also allows the crystal to be centred visually in the usual way. The crystal is mounted on a long, trimmed-to-fit MiTeGen MicroMount which is then glued into a hole on the top of the goniometer head, ensuring that the crystal remains stable throughout a series of data collections. A hole through the base of the gas cell connects to a stainless steel tube (Figure 6.4) which leaves the gas cell and attaches with a Swagelok adaptor to a 1/8 inch diameter Teflon tube. This flexible tube allows the gas cell to rotate freely in all directions on the diffractometer, while the sturdy Swagelok adaptor holds it securely in place if a small amount of tension should be applied to the tube during an experiment.

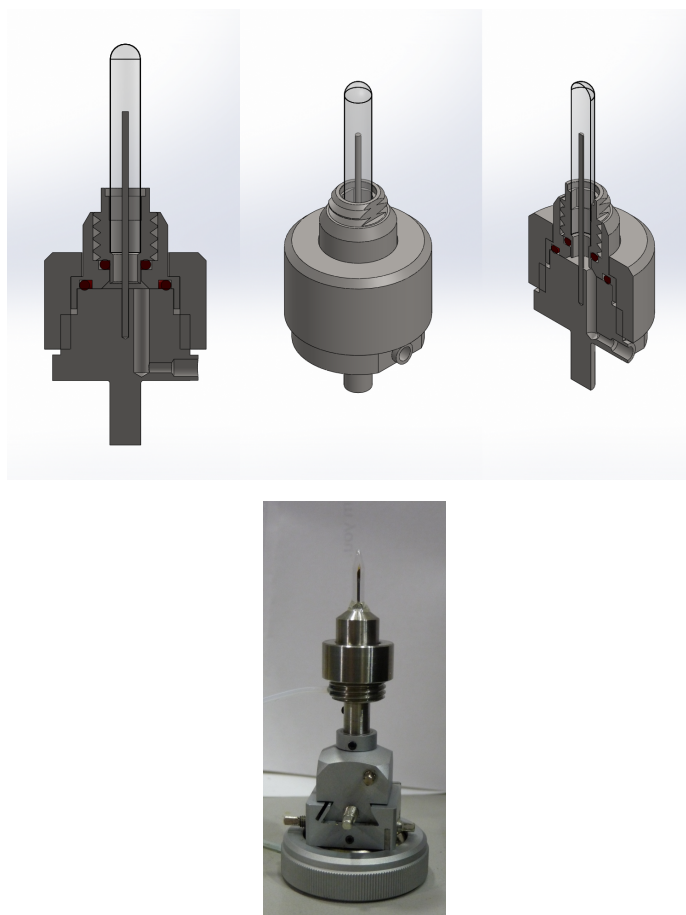


Figure 6.3: Cross-sectional images and photograph of the gas cell (images provided by Simon Teat and Jamie Nasiatk).

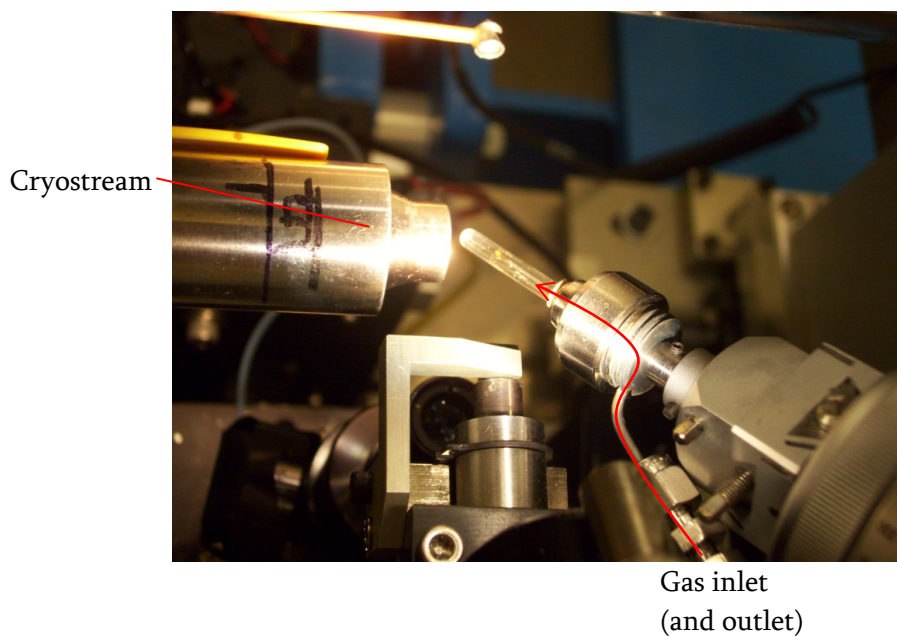


Figure 6.4: Gas cell mounted on the diffractometer on beamline 11.3.1 (image provided by Christine Beavers).

The Teflon tube is attached using another Swagelok adaptor to a stainless steel tube in the hutch, which is connected to the vacuum pump and the gas delivery system. A pressure gauge is also positioned near to this connection point so that the pressure within the gas cell can be monitored when the tube is connected to the hutch.

In gas cell experiments performed on beamline 11.3.1 before October 2011, a simple gas handling set-up was used (Figure 6.5). Only one cylinder at a time could be installed in the cabinet by a qualified member of staff, and so experimental conditions had to be considered in advance. The lines between the cylinder and the gas cell were loaded with gas before closing the cylinder and introducing the gas to the cell. This meant that the gas cell was never connected directly to an open cylinder; an important safety consideration when handling toxic or flammable gases under high pressure. However, the pressure could only be monitored in the gas cell and not in the cabinet itself, and the gas cell's pressure gauge was not visible when handling the gases; two people were always required when carrying out gas loading experiments.



Figure 6.5: First version of the gas handling setup on beamline 11.3.1. The single gas cylinder is on the right. House nitrogen is supplied through the plastic tubing. The stainless steel tube on the left connects to the gas cell in the hutch (image provided by Simon Teat).

In the summer of 2011 a new gas handling system was installed (Figure 6.6 and Figure 6.7), incorporating a number of improvements. Four different gases can be installed within the cabinet simultaneously as well as an external supply of house

nitrogen. One of the gas lines (labelled for SO<sub>2</sub> in the schematic) is suitable for the use of corrosive gases. The gas cabinet contains a mixing chamber and a pressure gauge, so the mixing chamber can be preloaded with a known pressure of gas before exposure to the gas cell. The incorporation of mass flow controllers allows the concentration of gas mixtures to be finely controlled, and adds an extra safety barrier to direct contact between open gas cylinders and the gas cell.



Figure 6.6: New gas handling system on beamline 11.3.1 (images provided by Simon Teat).

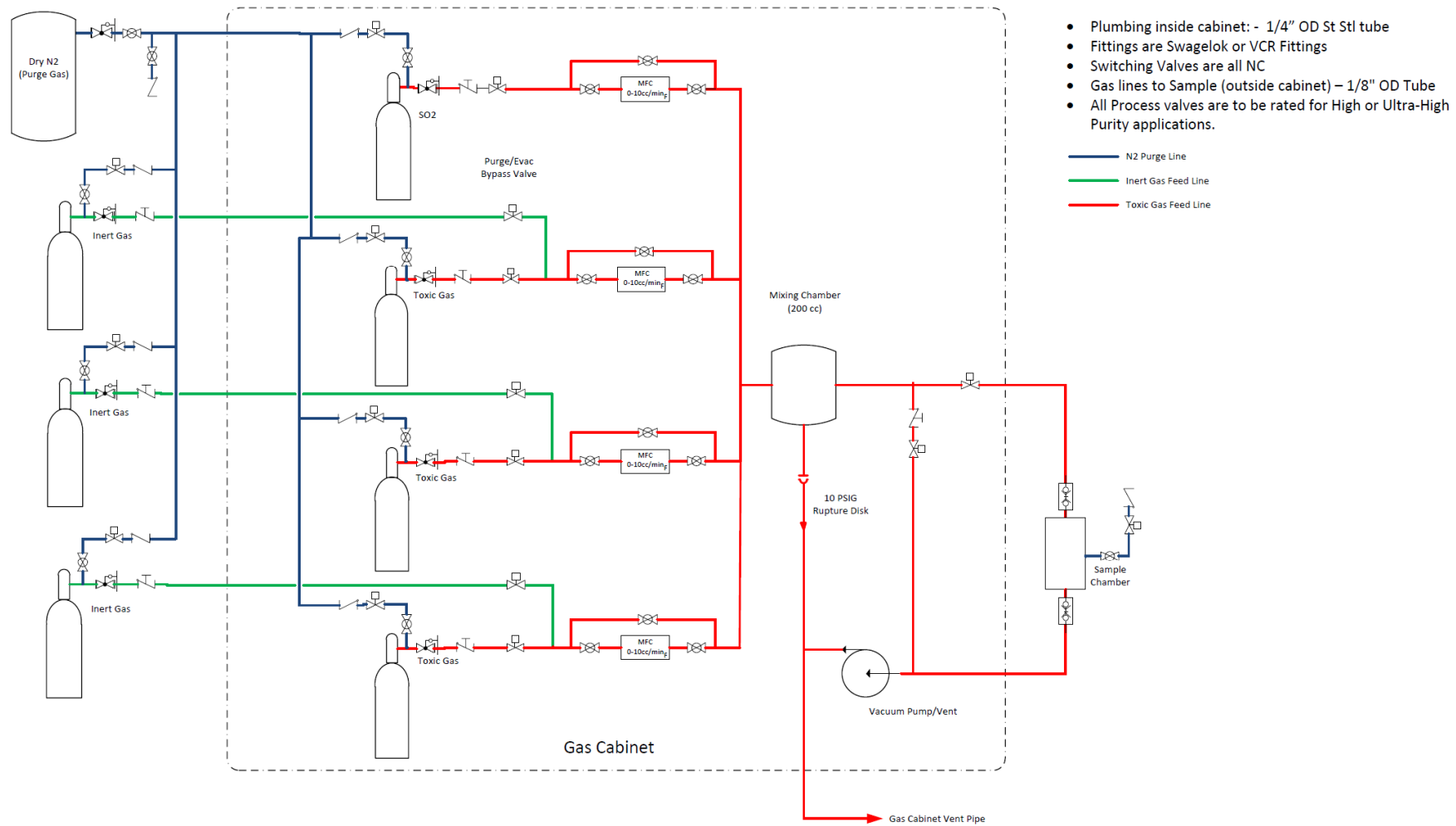


Figure 6.7: Schematic of the new gas handling system on beamline 11.3.1 (adapted from a schematic provided by Simon Teat and Jamie Nasiatk).

The gas cell is used at a synchrotron facility, and the higher X-ray flux that this provides is extremely beneficial. Small crystals can be used at a synchrotron such as the ALS, which is useful for *in situ* experiments that involve the adsorption or desorption of gases as the gas will penetrate a small crystal more quickly. Similarly, the higher flux allows data collection to occur at a much faster rate, thus speeding up the time it takes to perform an *in situ* experiment within the gas cell. Even on a synchrotron, many of the experiments discussed here took at least 8 hours to perform. Exposure to X-rays or to gases over an extended period of time can reduce the crystallinity of a sample, and so the shorter collection times and subsequently shorter overall experimental times can allow a crystal to survive through a lengthy experiment that includes many data collections.

### 6.3.1 General experimental procedure

A single crystal of Co-CPO-27 was selected under an optical microscope and mounted onto the tip of a MiTeGen micromount using a minimal amount of epoxy glue, taking care not to coat the surfaces of the crystal. This pin was glued into a bored hole in the goniometer head to hold it securely throughout the data collections. After the epoxy glue had dried, a lightly greased O-ring was placed around the base of the pin and the glass head was lowered over it, taking care not to allow the crystal to touch the sides. The glass head was tightened by hand using a metal screw loop. Once mounted on the diffractometer, the crystal could be centred in the usual way.

The gas cell's Teflon tubing was connected to the gas rig through which a dynamic vacuum was applied. The crystal temperature was controlled using an Oxford Cryostream 700 Plus device, which could heat the sample up to a maximum of 500 K. During dehydration procedures and after cooling the system, the Teflon tube was dried with a heat gun to encourage the removal of condensed water. The dynamic vacuum could be removed, leaving the crystal under a static vacuum, by closing a valve. Air could be reintroduced into the gas cell by disconnecting the Teflon tube from the gas rig and attaching a Swagelock adapter.

For Co-CPO-27 the coordinated water molecule, O1W, and sometimes the non-coordinated water molecule, O2W, were usually located in the initial structure solution. In others, peaks of electron density corresponding to the oxygen atoms of

these water molecules were not observed until subsequent refinement cycles. O3W and O4W were assigned during the refinement process. The occupancy of each water molecule was allowed to refine freely whilst its atomic displacement parameter (ADP) was fixed at 0.05, a value approximately twice that of the framework atoms. For HKUST-1, O1W was assigned using the Q-peaks. Its ADP was fixed at 0.1, a value approximately twice that of the other framework atoms, while its occupancy was allowed to refine freely. If the occupancy of a water molecule refined to a value of 1.00, its occupancy was fixed at 1.00 and its ADP was allowed to refine freely.

### 6.3.2 Gas cell improvements

In early gas cell experiments, the glass portion of the cell was constructed from an NMR (nuclear magnetic resonance) tube with a glass thickness of 0.5 mm. The gas cell was consequently very sturdy and could easily withstand the low pressures required for experiments under vacuum. However, the thickness of the glass produced a halo of background scattering in every frame, particularly between 1.5 and 1.1 Å. This reduced the quality of the data and led to an increased  $R_{int}$  value.

In an effort to improve the quality of the data and reduce the  $R_{int}$  values, thinner glass was installed on the gas cell. A custom-made tube with walls 60 µm thick was found to offer the best compromise, with the production of a minimal amount of background scattering while still being able to withstand a dynamic vacuum (Figure 6.8, Table 6.1).

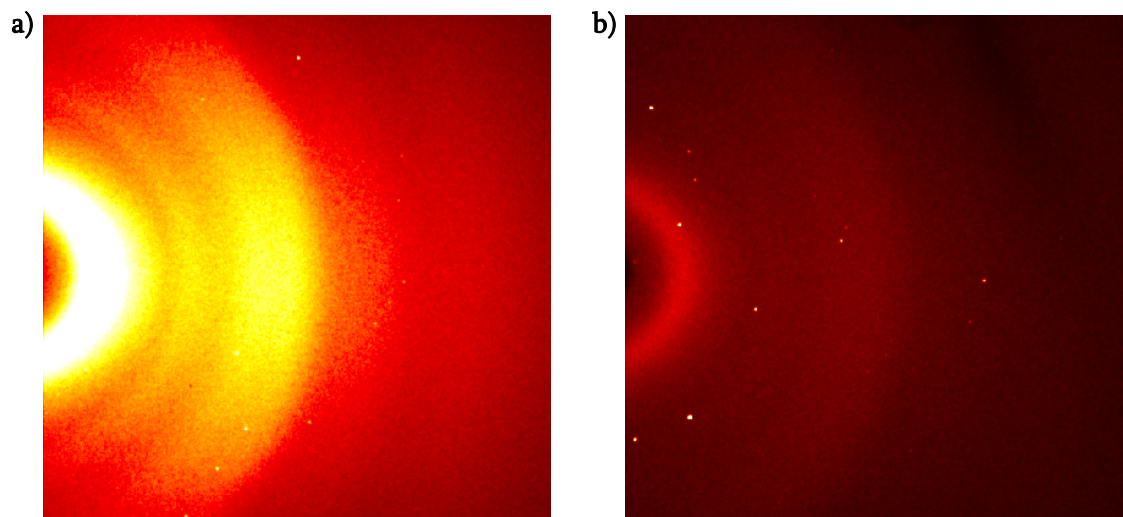


Figure 6.8: Diffraction images collected using single crystals of Co-CPO-27 in the gas cell on beamline 11.3.1, through glass of different thickness: a) 500  $\mu\text{m}$ , b) 60  $\mu\text{m}$ .

Table 6.1: Internal error of three selected data sets measured through 500  $\mu\text{m}$  and 60  $\mu\text{m}$  thick glass. Results selected represent the lowest, median and highest  $R_{int}$  values recorded.

Data set	Temperature	$R_{int}$
	/ K	/ %
500micron1	400	8.98
500micron2	293	16.85
500micron3	300	28.58
60micron1	355	5.49
60micron2	470	7.43
60micron3	298	18.42

## 6.4 Dehydration

### 6.4.1 Co-CPO-27

The first stage of all gas adsorption experiments using Co-CPO-27 involves a dehydration procedure. Dietzel et al. performed the *in situ* dehydration experiment at 95 °C, but reported that the compound retains crystallinity in an inert atmosphere up to 200 °C and in air up to 140 °C.<sup>9</sup>

In accordance with dehydration procedures reported in the literature,<sup>11</sup> the dehydration process within the gas cell was initially studied at 400 K. After 36 h at this temperature under vacuum, a dehydrated crystal structure was obtained with no water within the pores (400cpo1). However, the data set collected after the crystal was cooled to room temperature displayed approximately 26 % water occupancy on the cobalt sites (400cpo1b). This is a similar occupancy to that observed by Byrne.<sup>8</sup> Since this large amount of water reappeared without reversal of the vacuum, it is likely that water removed from the metal sites during the dehydration process remained disordered within the framework so that, when the temperature was reduced, this water returned to the metal sites. With shorter heating times, data sets obtained at 400 K were not themselves fully dehydrated (400cpo2, 400cpo3, 400cpo4).

Since the framework can withstand considerably higher temperatures than this while retaining crystallinity, the dehydration procedure was carried out at a range of higher temperatures from 420 K to 500 K (420cpo1, 423cpo, 450cpo, 470cpo, 480cpo1, 500cpo1, 500cpo2, 500cpo3, 500cpo4). 500 K is the maximum temperature at which the gas cell can operate. In some cases the crystal was then cooled to room temperature at which point a second data set was collected to follow the return of water to the metal site on cooling (420cpo1b, 480cpo1b, 500cpo1b, 500cpo2b, 500cpo3b, 500cpo4b). These results are summarised in Table 6.2.

Table 6.2: The extent of dehydration achieved for Co-CPO-27 at varying temperatures.

Data set	Temperature / K	O1W occupancy / %	SQUEEZE e- count	$R_f$ / %
400cpo1	400	0	161	3.55
400cpo1b	293	25.6(8)	177	4.49
400cpo2	400	18.7(7)	190	4.92
400cpo3	400	4.9(16)	220	5.98
400cpo4	400	53.5(7)	239	6.45
420cpo1	420	9.4(5)	171	4.19
420cpo1b	300	18.7(6)	189	4.56
423cpo	423	0	346	6.16
450cpo	450	32.6(4)	112	3.65
470cpo	470	33.4(5)	123	4.38
480cpo1	480	0	229	3.86
480cpo1b	293	27.5(6)	177	4.38
500cpo1	500	0	337	3.89
500cpo1b	283	0	368	3.58
500cpo2	500	0	162	3.90
500cpo2b	253	16.0(6)	246	5.11
500cpo3	500	0	194	4.08
500cpo3b	223	6.7(5)	161	4.11
500cpo4	500	0	187	4.93
500cpo4b	223	17.8(8)	173	5.79

In a number of data sets some water occupancy was still observed on the metal site at high temperature, but since there is no appreciable trend this is likely due to problems with the gas cell itself. On some occasions, such as 480cpo1/1b, the high temperature data set showed complete dehydration but a large amount of water returned to the metal sites upon cooling; 27.5% of the metal sites were reoccupied with water molecules. This increase in water occupation corresponded to a decrease

in the excess electron count in the pores, which suggests that at least some of this re-coordinated water was retained at high temperature, disordered within the pores.

It is clear from the results in Table 6.2 that 500 K is the optimum temperature for Co-CPO-27 dehydration within the gas cell. In all four cases full dehydration was achieved at high temperature. Most notably, though, full dehydration was preserved after cooling to below room temperature in 500cpo1b. No water could be located crystallographically within the structure, but the excess electron count within the pores of 500cpo1b was higher than for the other 500cpo structures, so there was probably a small amount of disordered water on the metal sites at a concentration too small to observe.

The dehydration process for Co-CPO-27 occurs in two steps; first the non-coordinated water in the pores is removed under vacuum and mild heating. The second stage of dehydration requires a higher temperature and involves the removal of the coordinated water molecules. Three uncoordinated water molecules can be observed in the pores: O2W, O3W and O4W. Previous experiments have shown that O3W and O4W are removed from the pores with only mild heating,<sup>1</sup> with O4W disappearing from the structure first. O2W, which is held in place by hydrogen-bonding with the coordinated O1W molecule, is the last non-coordinated water molecule to leave the framework and requires either a higher temperature or prolonged heating.

Through the study of many dehydration experiments, the concentration of water molecules within the pores of Co-CPO-27 could be studied in depth. Different levels of rehydration following dehydration procedures produced vastly differing occupancies of all four water molecules within the framework pores (Table 6.3). To investigate the relationship between occupancies of different water sites, plots of O1W-O2W, O2W-O3W and O3W-O4W occupancies were produced (Figure 6.9).

Table 6.3: Water occupancies within Co-CPO-27 in different data sets.

Data set	Temperature / K	O1W occupancy / %	O2W occupancy / %	O3W occupancy / %	O4W occupancy / %	$R_I$ / %	$R_{int}$ / %
dehyd1	293	100.0	91.5(12)	41.3(13)	39.1(13)	7.62	16.85
dehyd2	300	100.0	87.4(10)	40.0(10)	31.4(9)	6.02	6.59
dehyd3	298	100.0	83.8(11)	30.6(10)	38.9(10)	7.59	8.71
dehyd4	293	100.0	83.6(17)	43.0(15)	9.3(16)	6.74	8.58
dehyd5	293	100.0	82.4(15)	44.5(16)	8.0(15)	8.42	9.05
dehyd6	300	100.0	79.7(10)	34.9(9)	22.9(9)	6.33	7.36
dehyd7	298	100.0	59.4(12)	34.0(13)	8.0(12)	6.96	18.42
dehyd8	500	43.2(7)	-	-	-	4.11	7.36
dehyd9	223	42.3(16)	25.2(16)	18.4(16)	-	11.14	7.35
dehyd10	223	40.4(13)	27.6(14)	12.7(14)	-	10.33	16.34
dehyd11	298	35.5(7)	-	-	-	6.68	15.90
dehyd12	470	33.4(5)	-	-	-	4.38	7.43
dehyd13	450	32.6(4)	-	-	-	3.65	6.14
dehyd14	293	27.5(6)	-	-	-	4.38	9.44
dehyd15	298	26.4(6)	-	-	-	5.24	12.62
dehyd16	293	25.6(8)	-	-	-	4.49	11.95
dehyd17	223	20.4(10)	11.1(10)	5.1(10)	-	6.38	8.61
dehyd18	400	18.7(7)	-	-	-	4.92	20.91
dehyd19	300	18.7(6)	-	-	-	4.56	7.42
dehyd20	223	18.3(8)	6.6(8)	-	-	5.79	8.03

dehyd21	253	16.0(6)	-	-	-	5.11	9.12
dehyd22	355	13.8(6)	-	-	-	4.00	5.49
dehyd23	420	9.4(5)	-	-	-	4.19	7.55
dehyd24	223	6.7(5)	-	-	-	4.11	9.28
dehyd25	400	4.9(16)	-	-	-	5.98	6.07
dehyd26	500	1.1(7)	-	-	-	3.98	5.70

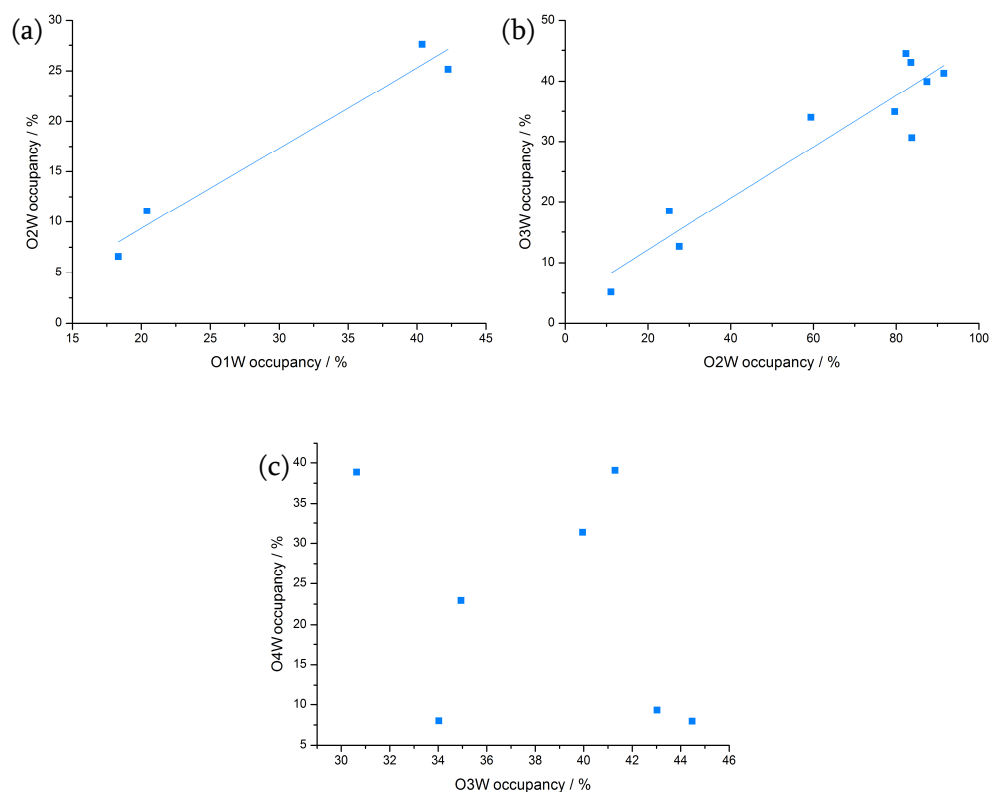


Figure 6.9: Relationship between percentage occupancy of different water sites within Co-CPO-27; a) O1W-O2W, b) O2W-O3W and c) O3W-O4W.

Whenever the O1W site was fully occupied, water could be observed at all three other sites. At 223 K (-50 °C), O2W and O3W could be observed when the occupancy of O1W was as low as 18.3 %, but at higher temperatures these sites could only be observed when O1W was fully occupied. Excess water molecules were probably present in the framework pores at the higher temperatures but were

distributed throughout the pore, whereas at a lower temperature they condensed into the O2W and O3W sites and could be observed crystallographically.

There is no linear relationship between the occupancies of O3W and O4W, likely in part due to the low occupancy of both water sites producing more error in the calculations during refinement of the crystal data. The removal of non-coordinated water from these two sites is independent of one another, and there is little interaction between the two water molecules.

There is a positive linear relationship between the occupancies of O1W and O2W ( $R^2 = 0.9456$ ,  $y = 0.7971x - 6.58165$ ), and also between the occupancies of O2W and O3W ( $R^2 = 0.87225$ ,  $y = 0.42531x + 3.5968$ ). The intercept in the first case indicates that a minimum occupation of the O1W site is required before the O2W site begins to be filled. In the second case, the value of the intercept suggests that O3W is partially occupied when O2W is empty. This is not observed in the crystal structures, so the intercept was fixed at the origin to represent the fact that, at zero occupancy of O2W, O3W is also unoccupied ( $y = 0.48329x$ ). Using the linear regression lines as a model it is possible to predict the occupancy of O1W if the occupancy of either O2W or O3W is known. Such predictions are used in Chapter 7.

The presence of a particular concentration of coordinated water, O1W, enables a certain concentration of O2W to be held within the framework through hydrogen bonding, with an O1W...O2W bond distance of 3.03(4) Å. Non-coordinated O2W begins to be found within the framework before all of the metal sites are occupied by O1W molecules; in data sets dehyd9, dehyd10 and dehyd18 some O3W water molecules can also be observed before the cobalt coordination sphere is saturated. This relationship is only seen in the low temperature data sets. As discussed above, in higher temperature experiments the water is probably present in the pores but cannot be detected crystallographically. Therefore any predictions of O1W occupancy made at higher temperatures using the linear regression will probably underestimate the actual percentage of coordinated O1W.

## 6.4.2 HKUST-1

Dehydration of HKUST-1 was carried out by heating a single crystal inside the gas cell under a dynamic vacuum at 420 K for 2 hours. A crystal structure, HKUSTdehyd, was obtained at 420 K (Table 6.4).

Table 6.4: Crystallographic data for hydrated HKUST-1, from the literature, and dehydrated HKUST-1, HKUSTdehyd.

	Hydrated <sup>10</sup>	HKUSTdehyd
T / K	293	420
$R_{int}$	16.00	7.69
Formula	C <sub>6</sub> H <sub>4</sub> CuO <sub>5</sub>	C <sub>6</sub> H <sub>2.06768</sub> CuO <sub>4.03384</sub>
FW / g mol <sup>-1</sup>	219.64	202.23
Crystal system	Cubic	Cubic
Space group	$Fm\bar{3}m$	$Fm\bar{3}m$
$a$ / Å	26.343(5)	26.196(5)
$V$ / Å <sup>3</sup>	18280(7)	17976(6)
$Z$	48	48
$\rho_{calc}$ / Mg m <sup>-3</sup>	0.958	0.897
$\mu$ / mm <sup>-1</sup>	1.422	4.12
Data / restraints / parameters	853 / 0 / 43	1419 / 0 / 37
Goodness of fit on $F^2$	1.151	0.788
Final $R$ indices [ $I > 2\sigma(I)$ ] / %	$R_1 = 0.0599$ , $wR_2 = 0.1678$	$R_1 = 0.0271$ , $wR_2 = 0.0932$
$R$ indices (all data) / %	$R_1 = 0.0905$ , $wR_2 = 0.2652$	$R_1 = 0.0344$ , $wR_2 = 0.0999$

With the thermal parameter of the coordinated water molecule set at 0.10, the water occupancy was found to be 3.38 %. SQUEEZE indicates that 515 electrons are disordered within the pores which suggests, based upon the Co-CPO-27 dehydration studies, that some of this would recondense onto the metal sites upon cooling and lead to an increase in water occupancy. However, the crystal degraded due either to prolonged X-ray exposure or to its exposure to vacuum and high temperatures so no further experiments could be carried out.

Upon removal of water from the pores, the unit cell axes of HKUST-1 were reduced by approximately 0.147 Å. This shrinking of the unit cell corresponds to a 0.142 Å decrease in the Cu-Cu internuclear separation within the copper dimer (Table 6.5, Figure 6.10). The Cu-OH<sub>2</sub> bond length increased significantly upon dehydration, but the very low occupancy of the O1W site together with the high temperature at which the data were collected means that the error on the bond length in HKUSTdehyd was very large.

Table 6.5: Key distances in hydrated and dehydrated HKUST-1.

	Hydrated <sup>10</sup>	HKUSTdehyd
<b>Cu-Cu distance</b>	2.628(2)	2.486(1)
<b>Cu-OCO bond length</b>	1.952(3)	1.928(1)
<b>Cu-OH<sub>2</sub> bond length</b>	2.165(8)	2.42(13)

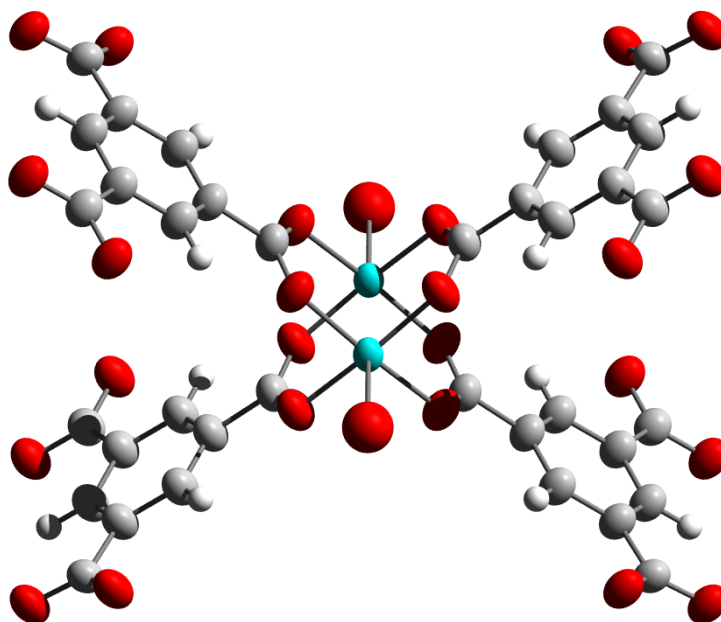


Figure 6.10: Copper(II) tetracarboxylate building block with 2.66 % water occupancy.

HKUST-1 contains square-shaped pores that run throughout the framework in three directions, with copper atoms at the corners of the squares. From copper to copper, the pores in the hydrated structure have sides 7.999 Å long and 11.312 Å diagonally across. HKUSTdehyd has pores with 8.019 Å long sides, 11.340 Å diagonally. These slightly bigger pores in the dehydrated structure are produced when the copper atoms in the dimer building blocks move closer to one another, opening up a larger space in which gaseous molecules can adsorb.

## 6.5 Summary

The static gas cell on beamline 11.3.1 at the ALS has been developed and improved in a number of ways. The gas delivery set-up, originally capable of handling a vacuum pump and a single gas cylinder, is now capable of handling a vacuum pump, a house-supply of nitrogen and four different gas cylinders including a corrosive gas. A mixing chamber has been installed within this set up which will allow for mixtures of gases to be studied in the future.

Similarly, the gas cell itself has been improved significantly by changing its glass head to a much thinner one, which removed a large amount of amorphous scattering, particularly at low angle, and improved the quality of the data it produced.

Dehydration of Co-CPO-27 has been studied in depth. Dehydration has been shown to be most successful within the gas cell under dynamic vacuum when the Cryostream is heated to 500 K. The dehydration process occurs in a predictable manner, and the occupancy of each O1W, O2W or O3W site can be used to infer the occupancy of another of these water sites.

Single crystal dehydration of HKUST-1 has also been studied for the first time using the gas cell under a dynamic vacuum at 420 K. A high level of dehydration was achieved, but the crystal degraded during the experiment to the point where no further results could be collected. Further investigations with HKUST-1 in the gas cell would be an interesting avenue to pursue; if it retains crystallinity after gas exposure a crystal structure such as NO-loaded HKUST-1 could be produced.

## 6.6 CIF key

Table 6.6: Key to CIFs (Appendix) referred to in Chapter 6.

Reference code	CIF name	Reference code	CIF name
500micron1	01.cif	dehyd2	25.cif
500micron2	02.cif	dehyd3	26.cif
500micron3	03.cif	dehyd4	27.cif
60micron1	04.cif	dehyd5	28.cif
60micron2	05.cif	dehyd6	29.cif
60micron3	06.cif	dehyd7	03.cif
400cpo1	04.cif	dehyd8	30.cif
400cpo1b	07.cif	dehyd9	31.cif
400cpo2	08.cif	dehyd10	32.cif
400cpo3	09.cif	dehyd11	33.cif
400cpo4	10.cif	dehyd12	02.cif
420cpo1	11.cif	dehyd13	14.cif
420cpo1b	12.cif	dehyd14	16.cif
423cpo	13.cif	dehyd15	34.cif
450cpo	14.cif	dehyd16	07.cif
470cpo	02.cif	dehyd17	35.cif
480cpo1	15.cif	dehyd18	08.cif
480cpo1b	16.cif	dehyd19	12.cif
500cpo1	17.cif	dehyd20	24.cif
500cpo1b	18.cif	dehyd21	20.cif
500cpo2	19.cif	dehyd22	36.cif
500cpo2b	20.cif	dehyd23	11.cif
500cpo3	21.cif	dehyd24	22.cif
500cpo3b	22.cif	dehyd25	09.cif
500cpo4	23.cif	dehyd26	37.cif
500cpo4b	24.cif	HKUSTdehyd	38.cif
dehyd1	05.cif		

## 6.7 References

1. P. K. Allan, University of St Andrews, 2012.
2. D. C. Puxley, G. D. Squire, and D. R. Bates, *J. Appl. Crystallogr.*, 1994, **27**, 585–594.
3. M. Brunelli and A. N. Fitch, *J. Synchrotron Radiat.*, 2003, **10**, 337–339.
4. K. S. Kroeger and C. E. Kundrot, *J. Appl. Crystallogr.*, 1994, **27**, 609–612.
5. M. H. B. Stowell, S. M. Soltis, C. Kisker, J. W. Peters, H. Schindelin, D. C. Rees, D. Cascio, L. Beamer, P. J. Hart, M. C. Wiener, and F. G. Whitby, *J. Appl. Crystallogr.*, 1996, **29**, 608–613.
6. D. S. Yufit and J. A. K. Howard, *J. Appl. Crystallogr.*, 2005, **38**, 583–586.
7. J. E. Warren, R. G. Pritchard, D. Abram, H. M. Davies, T. L. Savarese, R. J. Cash, P. R. Raithby, R. Morris, R. H. Jones, and S. J. Teat, *J. Appl. Crystallogr.*, 2009, **42**, 457–460.
8. P. J. Byrne, University of St Andrews, 2009.
9. P. D. C. Dietzel, Y. Morita, R. Blom, and H. Fjellvåg, *Angew. Chem. Int. Ed.*, 2005, **44**, 6354–6358.
10. S. S. Chui, S. M.-F. Lo, J. P. H. Charmant, A. G. Orpen, and I. D. Williams, *Science*, 1999, **283**, 1148–1150.
11. A. C. McKinlay, B. Xiao, D. S. Wragg, P. S. Wheatley, I. L. Megson, and R. E. Morris, *J. Am. Chem. Soc.*, 2008, **130**, 10440–10444.

## CHAPTER 7: *In situ* gas adsorption single crystal studies

### 7.1 Aims

This study aims to utilise the new *in situ* gas cell for a proof-of-concept experiment, exposing a single crystal to gas during an X-ray diffraction experiment for the first time in order to obtain a gas-loaded crystal structure. Co-CPO-27 is chosen for the single crystals due to its high crystallinity and its strong and well understood interaction with NO gas. A full dehydration/adsorption/release cycle of NO in Co-CPO-27 will be obtained in order to understand the cycle fully for the further development of M-CPO-27 frameworks as biological NO delivery agents, as well as to test the capabilities of the gas cell.

The same technique will be employed to expose single crystals of Co-CPO-27 to CO gas and obtain a new crystal structure. The bonding mode of CO on the Co-centre will be examined in detail as a CO-loaded CPO-27 structure has not been obtained before by crystallographic means.

Furthermore, single crystallography experiments will be performed with olefins in an attempt to understand their interactions with the open metal sites in the M-CPO-27 series. Ethylene and propylene adsorption on Co-CPO-27 will be studied using the same *in situ* gas cell.

### 7.2 Nitric oxide

Nitric oxide, or nitrogen monoxide, is a diatomic molecule with the molecular orbital diagram shown in Figure 7.1. There is significant s-p mixing, so the  $\pi_{2p}$  orbital lies lower in energy than the  $\sigma_{2p}$  orbital. The antibonding  $\pi_{2p}^*$  orbital is both the highest occupied molecular orbital (HOMO) and the lowest unoccupied molecular orbital (LUMO). Nitric oxide has a bond order of 2.5 with a bond length of 1.151 Å.<sup>1</sup>

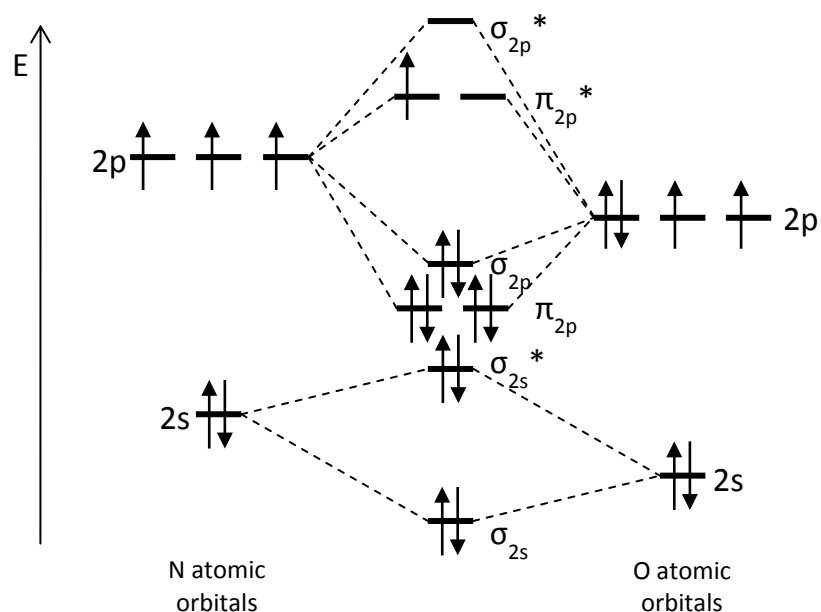


Figure 7.1: Molecular orbital diagram of nitric oxide.

The unpaired electron in the  $\pi_{2p}^*$  orbital causes NO to be a radical, although it does not readily dimerise to form ON-NO in the gaseous state as the entropy lost in dimerisation is much greater than the energy gained by the formation of a weak N-N bond. NO forms a  $[\text{NO}]^+$  and a  $[\text{NO}]^-$  species by the loss and the gain of a single electron, respectively.

Nitric oxide reacts with transition metals to produce nitrosyl complexes. NO can bind to a metal centre in two different binding modes; linearly as a 3-electron donor, or in a bent conformation as a 1-electron donor (Figure 8.2). Before interaction, the transition metal has a singly occupied  $d_\pi$  orbital and an empty  $d_\sigma$  orbital and NO has a doubly occupied  $\sigma_{2p}$  orbital and a singly occupied  $\pi_{2p}^*$  orbital.

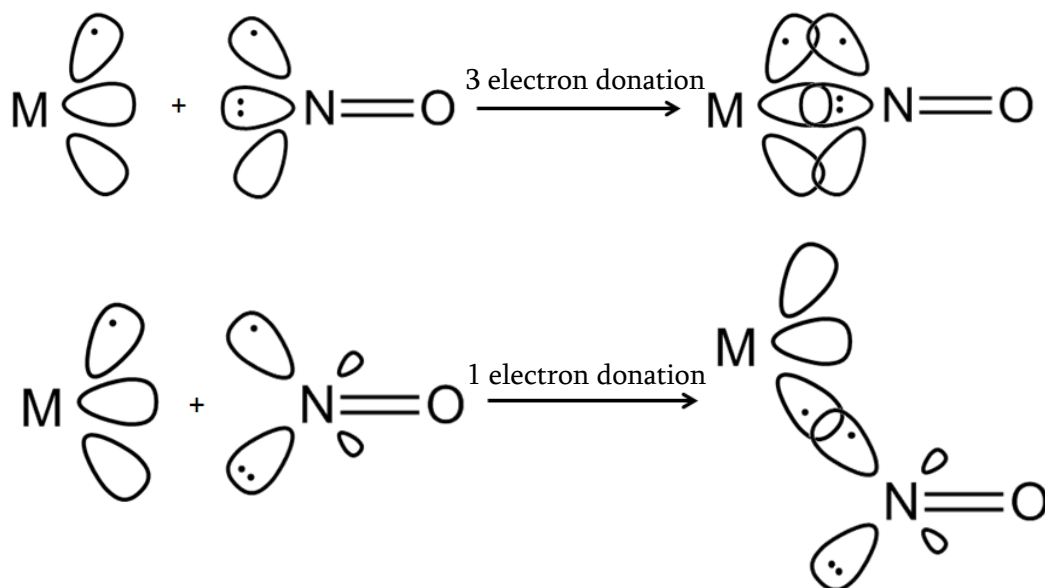


Figure 7.2: Electronic structure of NO and its binding modes to a transition metal centre.

In the linear case, the  $d_{\pi}$  orbital and the  $\pi_{2p}^*$  orbital each donate one electron to produce a M-N  $\pi$  bond and the  $\sigma_{2p}$  orbital donates 2 electrons into the  $d_{\sigma}$  orbitals to produce a M-N  $\sigma$  bond. Overall, the NO molecule donates 3 electrons. In the bent case the N atom of NO rehybridises to produce two  $sp^2$  orbitals, one containing two electrons and the other a single electron. The partially occupied  $sp^2$  orbital interacts with the partially occupied  $d_{\pi}$  orbital to produce a single M-N bond.<sup>2</sup>

### 7.2.1 Applications

Gaseous NO is produced in internal combustion engines alongside  $\text{NO}_2$  creating  $\text{NO}_x$ , a major component of smog. Despite its toxicity, NO is important in a number of aspects of human biology. Its role as a signalling molecule in the cardiovascular system was discovered by Furchgott, Ignarro and Murad, and for this work they were jointly awarded the 1998 Nobel Prize in Physiology.

NO has a very low physiological concentration of approximately 5 nM, due in part to its low solubility in water but also due to its high reactivity.<sup>3</sup> It is produced in the body by three different types of nitric oxide synthase (NOS) enzymes. Endothelial NOS (eNOS), which regulates vascular function, is present in the layer of cells that line the walls of blood vessels and can also be found in the kidneys, heart and brain. Inducible NOS (iNOS) is found in macrophage cells (a type of white blood cell), but it is only produced when required; iNOS is involved in the immune response

and produces the NO used to cause cell death (apoptosis). Neural NOS (nNOS), present in brain cells, is involved in cell communication.<sup>4</sup>

The importance of NO in the body is demonstrated by the effects of incorrect physiological concentrations. Elevated NO concentration causes conditions such as Parkinson's disease, fibrosis, hypertension and sexual impotence, whereas reduced concentration causes septic shock, excessive bleeding, hypotension, meningitis, diabetes, asthma and rheumatoid arthritis.<sup>4</sup>

NO activates the enzyme guanylate cyclase in platelets, preventing their aggregation in blood vessels. It may also cause the vascular muscles to relax, further aiding in the prevention of platelet aggregation. In another of its functions, NO forms nitrates with oxygen-based radicals in the blood, preventing macrophages from adhering to a cut in an artery wall and thus preventing stenosis, or narrowing of the blood vessel. In some cases stents must be surgically inserted in order to enlarge a blood vessel, and such a site promotes the formation of blood clots; some stents contain NO-releasing materials which aid in the prevention of thrombosis formation. NO is also important in wound healing with respect to both speed and strength of collagen production and so its use in dressings could be beneficial in many cases, particularly for diabetic ulcers when wound healing is more difficult.<sup>5</sup>

A number of therapies involving the delivery of NO to the body have been developed. The concentration required to obtain the biological effect depends upon the response desired; a concentration in the nanomolar range is required to observe antiplatelet action, whereas a millimolar concentration is needed for antibacterial action.<sup>6,7</sup> The method of NO delivery must, therefore, provide an exact amount of gas over a certain period of time. Direct delivery to the targeted area is most desirable as the physiological lifetime of NO is very short, while also avoiding the production of side effects in other parts of the body.

Glyceryl trinitrate (GTN) has been used to treat angina pectoris for over one hundred years. Its mechanism involves enzyme metabolism to produce NO *in vivo*, and it is this that causes the important vasodilatory effect.<sup>8</sup> The same treatment is used to treat thrombosis, but side effects such as headaches and dizziness are common.

Diazeniumdiolates (NONOates) and S-nitrothiols both produce NO in chemical reactions within the body and they have been investigated for use as medical coatings to prevent platelet aggregation and restenosis (the recurrence of a narrowed blood vessel). NO gas is administered to full-term infants with respiratory failure, reducing the need to reoxygenate the blood outside the body, although this treatment is unsuccessful with premature infants.<sup>9,10</sup>

Post-injury the NO concentration in damaged areas of the body varies over time, and it has been found that an arginine-enriched diet (arginine being a precursor to NO in the body) improves the speed and strength of wound healing. It is reasonable to propose that NO delivered directly to a wound could promote wound healing.

One way to deliver NO to the skin is to use creams or ointments that release NO. Acidified nitrite cream, for example, is used to treat athlete's foot by releasing NO to kill the fungus.<sup>11</sup> A similar cream has been used to promote wound healing in both normal and diabetic mice,<sup>12</sup> but such preparations also produce inflammation and scarring<sup>13</sup>. In an individual case study involving a chronic leg ulcer that had failed to heal after two years, application of 200 ppm gaseous nitric oxide overnight for 14 days resulted in complete healing of the wound.<sup>14</sup>

Another way in which NO could be delivered to a specific site on the skin is to use dressings that contain a solid that releases NO over time. For example, the bioactivities of both NO-loaded zeolite-A and NO-loaded HKUST-1 have been reported in the literature,<sup>15,16</sup> with further studies on-going involving the incorporation of NO-loaded MOFs into polymer films.

## 7.2.2 Previous work

The adsorption of NO onto Co-CPO-27 produces a Type I isotherm. The framework has a NO capacity of approximately 7 mmol g<sup>-1</sup> at room temperature, with significant hysteresis being observed. After desorption of the physisorbed gas, 4.99 mmol g<sup>-1</sup> remains chemisorbed to the vacant metal sites (Figure 7.3).

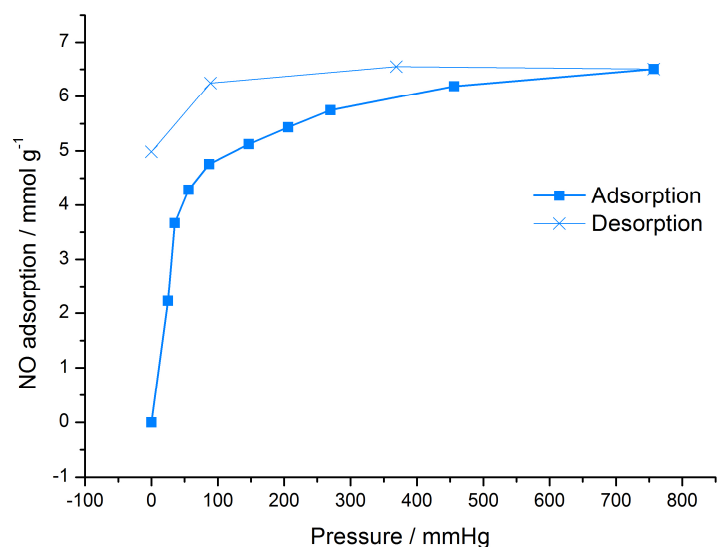


Figure 7.3: NO adsorption and desorption isotherm at 298 K.

Exposure to moisture displaces the adsorbed NO, with the release of all the stored gas occurring over approximately 20 hours but most of the NO being displaced in the first 5 hours (Figure 7.4).

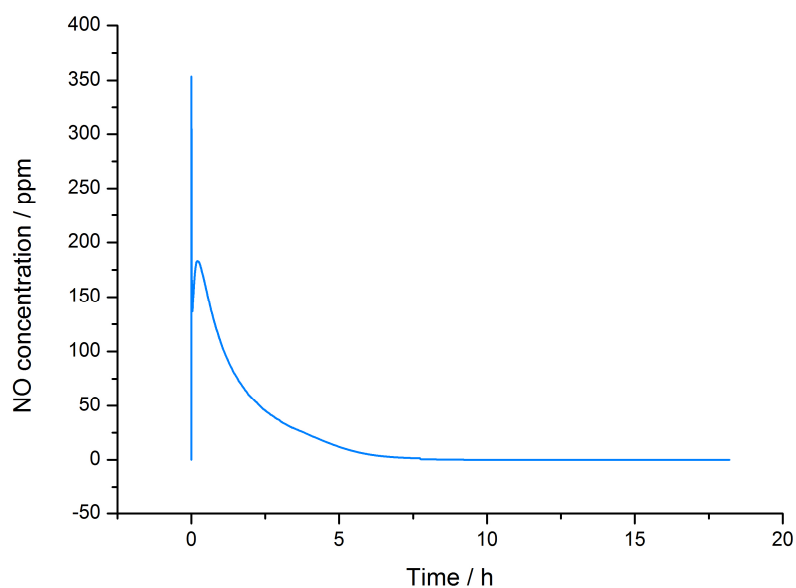


Figure 7.4: NO release from Co-CPO-27. NO concentration indicates the concentration of NO in a wet nitrogen stream.

The crystallinity of Co-CPO-27 is retained after dehydration. Rietveld refinement against powder X-ray diffraction data indicates that the NO molecules are coordinated to the metal sites in a bent geometry through the nitrogen atom (Figure 7.5).<sup>17</sup>

The model obtained from powder data was improved upon using an environmental gas flow cell at Station 9.8 at the SRS. Partially dehydrated and NO-loaded crystal structures were obtained *in situ*. The N atom of the gas molecule was located on the metal site, and two O environments for the O atom of NO were assigned, indicating that the NO molecule is disordered. The high level of hydration in all data sets calls these results into question, and the fact that N-O and Co-O bond lengths were modelled and not refined means that the crystal structure provides little new information.<sup>18</sup> The limitations of this previous work means that the relative occupancy of the metal centre by NO and water is unclear, delocalisation of the NO oxygen atom cannot be visualised and Co-N, Co-O and N-O bond lengths and angles are highly ambiguous.

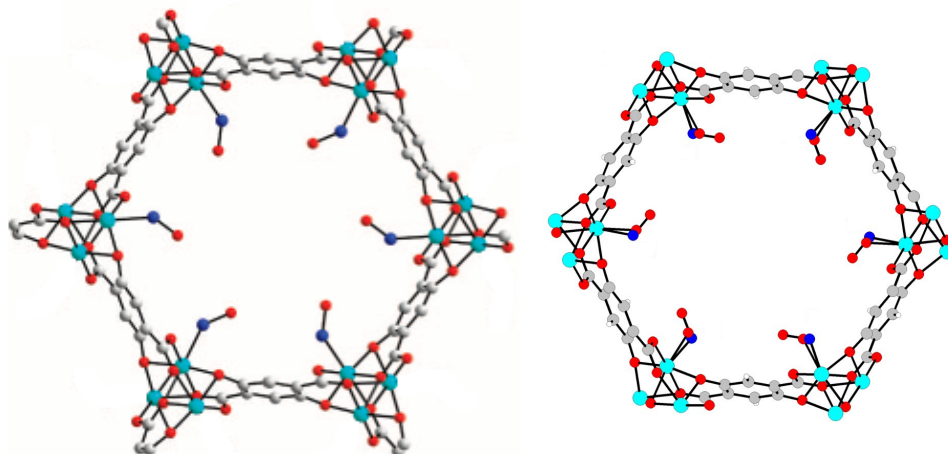


Figure 7.5: Co-CPO-27 pores with NO bound to the metal sites. (a) Structure obtained from powder X-ray diffraction. Image adapted from reference 19. (b) Structure obtained from single crystal X-ray diffraction using a flow gas cell, showing dual occupancy of the metal sites by NO and water. Image adapted from reference 18.

### 7.2.3 Experimental

Crystal selection and dehydration was performed as described in Chapter 6. A crystal structure of the dehydrated framework was collected at 500 K (CPO-500dehyd).

After dehydration, the crystal was cooled to the desired temperature by adjusting the target temperature of the Cryostream to 355 K, at which point a crystal structure was collected to gauge the amount of water occupancy before NO loading (CPO-355dehyd). The cell was isolated from the gas rig and the vacuum pump was

turned off. A small amount of NO was used to purge the lines and mixing chamber within the gas rig. NO gas was introduced into the mixing chamber of the gas rig at a steady rate by a mass flow controller to a pressure of approximately 800 torr, the mass flow controller was turned off and the gas was introduced into the gas cell. The mass flow controller was used to slowly increase the pressure within the gas cell up to approximately 800 torr, before it and the cylinder were both closed. Data collection began after approximately 10 minutes, providing time for the NO gas to penetrate into the crystal (CPO-NO-a/b/c/d).

The NO gas was removed from the system using the vacuum pump (CPO-283vac). The gas cell was heated to 373 K (CPO-373vac), 450 K (CPO-450vac) and 500 K (CPO-500vac) before being cooled to room temperature and exposed to air (CPO-293air) by removing the Teflon tube from the gas rig and attaching a Swagelok adaptor to the end.

In the NO-containing crystal structures, the same procedure was followed for each data set. The crystal structure was solved using SIR97<sup>20</sup>, and from the solution all framework atoms were assigned. In some cases the coordinated nitrogen atom on the cobalt sites was also located from the structure solution. Aromatic hydrogen atoms were placed geometrically. The framework was refined anisotropically and the nitrogen atom was refined isotropically. Significant Q-peaks around the nitrogen atom were assigned as disordered oxygen from the coordinated NO molecule. More details about the treatment of the NO molecule for each refinement are provided alongside the results.

## 7.2.4 Results

### 7.2.4.1 Dehydrated Co-CPO-27

At 500 K, 1.1 % of the metal sites were occupied by water (CPO-500dehyd). After being heated at 500 K for 4 hours, the crystal was cooled to 355 K and at this temperature the metal site was 13.6 % occupied by re-coordinated water (CPO-355dehyd) (Figure 7.6).  $R_i$  converged to 3.98 %.

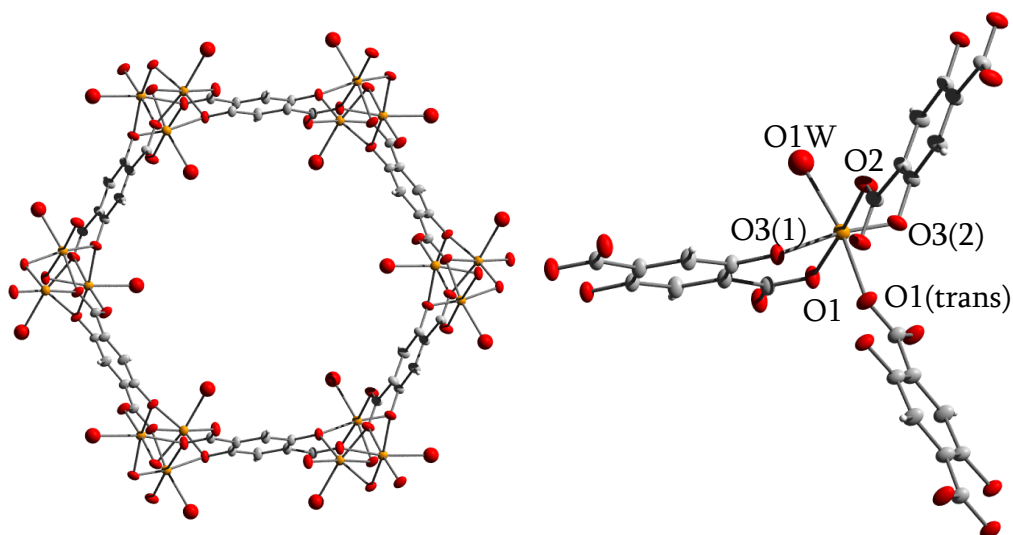


Figure 7.6: Co-CPO-27 at 355 K (CPO- 355dehyd) after dehydration. (a) One pore. (b) One cobalt centre, with coordinated oxygen atoms labelled.

#### 7.2.4.2 NO-loaded Co-CPO-27

NO was loaded onto the framework at 355 K before the crystal was cooled to 283 K and a data set was collected.

Nitric oxide binds to the cobalt site through the nitrogen atom in a bent configuration. With the occupancy of N1 fixed at 100 % and the NO oxygen atoms' isotropic thermal parameters fixed at  $0.05 \text{ \AA}^2$ ,  $R_I$  converged to 7.03 %. The Co-N bond is shorter than that found in the powder diffraction experiment. It is also significantly shorter than the Co-O bond in the hydrated structure (Table 7.1). NO binds to the cobalt centre with Co-N-O angles in the range of  $117.8(15)^\circ$  to  $133.2(26)^\circ$  (Table 7.2). Coordination occurs through the donation of one electron from a partially occupied  $sp^2$  hybridised N orbital to a partially occupied Co  $d_\pi$  orbital to form a single Co-N bond. The N-O bond order is reduced from 2.5 to 2, so a weaker and therefore longer N-O bond is expected in comparison to the free gaseous molecule ( $1.151 \text{ \AA}$ )<sup>1</sup>. The N-O bond length in the CPO-NO model is, however, artificially short due to the highly disordered oxygen atom on the NO molecule placing a higher proportion of electrons in the area occupied by the N-O bond.

Table 7.1: Bond lengths for the coordinated molecule in hydrated and NO-loaded Co-CPO-27.

SEM = standard error of the mean.

	Hydrated Co-CPO-27 <sup>21</sup>	NO-loaded Co-CPO-27 (CPO-NO-a)	NO-loaded Co-CPO-27 (PXRD) <sup>17</sup>
Co-N	-	1.990(5) Å	2.196(16) Å
Co-OH <sub>2</sub>	2.158(7) Å	-	-
N-O	-	1.03965 (SEM = 0.033) Å	1.43(3) Å

Table 7.2: Bond angles for the coordinated NO molecule in NO-loaded Co-CPO-27.

	NO-loaded Co-CPO-27 (CPO-NO-a)	NO-loaded Co-CPO-27 (PXRD) <sup>17</sup>
Co-N-O	125.68 (SEM = 1.89) °	140.4(12) °

The disorder of the NO molecule's oxygen atoms indicates that the oxygen is spinning around the metal site, as there is no structural or electronic reason to suggest that the oxygen atom is located in one of six discrete positions. The oxygen portion of the NO molecule would therefore better be represented by a circle. Similarly, the N-O bond would be expected to be of equal length throughout the crystal regardless of the position of the oxygen atom. SADI commands were used to introduce restraints (CPO-NO-b), leading to a Co-O bond length of 1.997(6) Å and an average N-O bond length of 1.0348 (SEM = 0.0061) Å. The short N-O bond length is due to the low occupancy of the oxygen sites around the nitrogen atom.  $R_I$  converged to 7.1 %.

The occupancy of the oxygen atoms has thus far been allowed to refine freely and the sum of the refined occupancies suggest that the metal atom is 75.4 % occupied by NO molecules. Refinement of the occupancy of the nitrogen site, however, indicates that it is fully occupied. This disagreement could occur for a number of reasons: the model of the oxygen disorder may significantly underestimate the

amount of oxygen present, the metal centre may also be partially occupied by water molecules or, if there is a circle of oxygen instead of six separate sites, some electron density may have been missed by the model.

To test whether the discrepancy is due to an underestimation of the oxygen present around the metal sites, each of the six oxygen sites were fixed at an occupancy of 16.7 % and their thermal parameters were allowed to refine freely (CPO-NO-c).  $R_I$  converged to 7.3 %; an increase compared to before this treatment of the structure. The thermal parameters of the oxygen atoms varied widely from  $0.038 \text{ \AA}^2$  to  $0.260 \text{ \AA}^2$ .

Due to previous difficulties experienced with retaining a fully dehydrated structure (as discussed in Chapter 6), it seems likely that some water is present within the framework. The N atom's occupancy was fixed at 75.4 % and an additional oxygen atom was positioned at the same place with an occupancy of 24.6 % (CPO-NO-d). After refinement  $R_I$  converged to 6.99 %, with a Co-N bond length of  $2.0005(4) \text{ \AA}$  and a Co-OH<sub>2</sub> bond length of  $1.9935(5) \text{ \AA}$  (Figure 7.7; Figure 7.8; Table 7.3).

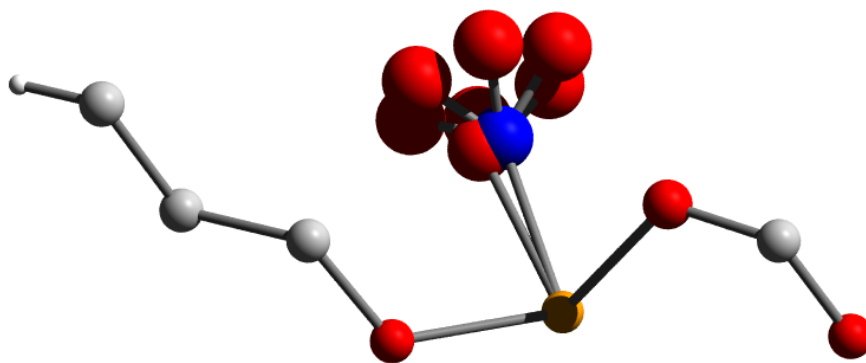


Figure 7.7: Asymmetric unit of NO-loaded Co-CPO-27, showing dual occupancy of the cobalt site.

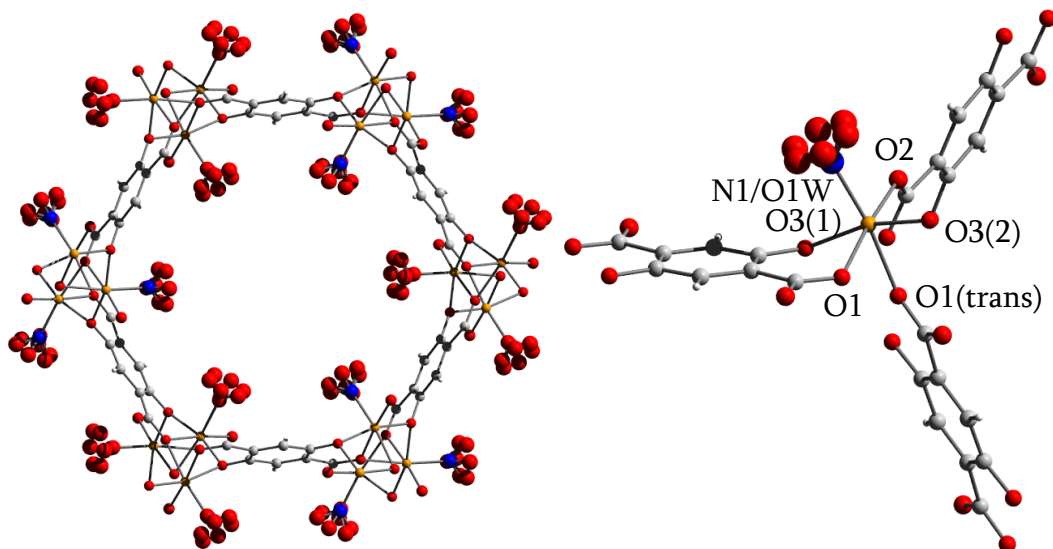


Figure 7.8: NO-loaded Co-CPO-27 at 355 K (CPO-NO-d). (a) One pore. (b) One cobalt centre, with coordinated oxygen and nitrogen atoms labelled.

Table 7.3: Bond lengths for hydrated, dehydrated and NO-loaded Co-CPO-27. (Atom labels correspond to Figure 7.8.)

	Hydrated Co-CPO-27 <sup>21</sup>	Dehydrated Co-CPO-27 (CPO-355dehyd)	NO-loaded Co-CPO-27 (CPO-NO-d)
Co-N1	-	-	2.0005(4) Å
Co-O1W	2.158(9) Å	2.2782(20) Å	1.9935(5) Å
Co-O1(trans)	2.191(8) Å	2.0731(17) Å	2.1599(4) Å
Co-O1	2.061(6) Å	2.0809(19) Å	2.0726(7) Å
Co-O2	2.037(6) Å	2.0109(18) Å	2.0200(8) Å
Co-O3(1)	2.042(5) Å	2.0016(18) Å	2.0100(5) Å
Co-O3(2)	2.047(7) Å	2.0237(16) Å	2.0111(6) Å

The Co-O1(trans) bond in hydrated Co-CPO-27 is elongated compared to the axial Co-O framework bonds. When the water molecule is removed from the structure the cobalt becomes 5-coordinate and this Co-O1(trans) bond shortens to

become similar in length to the other Co-O bonds. When a NO molecule coordinates to the vacant metal site this bond lengthens once more to be longer than all other framework Co-O bonds, but remains shorter than in the original hydrated structure. This phenomenon may be due to lower electron donation from the NO ligand to the cobalt site in comparison to water. However, it could still be a consequence of some bias remaining in the model, moving O1(trans) towards the average centre of electron density.<sup>22</sup>

Table 7.4: Bond angles (in degrees) around the cobalt atom of hydrated Co-CPO-27<sup>21</sup>. (Atom labels correspond to Figure 7.8.)

	O1W	O1(trans)	O1	O2	O3(1)
O1(trans)	170.7(3)	-	-	-	-
O1	92.5(3)	79.6(2)	-	-	-
O2	92.7(3)	95.2(2)	174.8(2)	-	-
O3(1)	95.2(3)	89.0(2)	84.7(2)	95.3(2)	-
O3(2)	92.9(3)	81.5(2)	84.3(2)	95.1(2)	166.5(2)

Table 7.5: Bond angles (in degrees) around the cobalt atom of dehydrated Co-CPO-27 (CPO-355dehyd). (Atom labels correspond to Figure 7.8.)

	O1W	O1(trans)	O1	O2	O3(1)
O1(trans)	170.5(5)	-	-	-	-
O1	91.2(5)	83.2(1)	-	-	-
O2	84.9(5)	100.5(1)	176.0(1)	-	-
O3(1)	90.1(5)	96.7(1)	81.2(1)	99.9(1)	-
O3(2)	90.7(5)	80.9(1)	81.7(1)	97.2(1)	162.9(1)

Table 7.6: Bond angles (in degrees) around the cobalt atom of NO-loaded Co-CPO-27 (CPO-NO-d). (Atom labels correspond to Figure 7.8.)

	O1W	N1	O1(trans)	O1	O2	O3(1)
N1	6.7(10)	-	-	-	-	-
O1(trans)	171.5(8)	172.5(3)	-	-	-	-
O1	91.7(9)	96.6(3)	80.1(1)	-	-	-
O2	94.7(9)	89.7(3)	93.5(1)	173.6(1)	-	-
O3(1)	90.3(9)	95.5(3)	90.8(1)	82.3(1)	96.3(1)	-
O3(2)	96.8(9)	92.8(3)	80.1(1)	82.8(1)	97.9(1)	163.6(1)

The bond angles (Table 7.4) between the coordinated water molecule, the cobalt atom and the axial oxygen atoms range between 92.5(3) and 95.2(3) for the fully hydrated structure. When the water is removed from the framework and the O1W site is only 13.6 % occupied, these angles all reduce to between 84.9(5) and 91.2(5) (Table 7.5). With NO coordinated to the cobalt site, the angles between the nitrogen atom, cobalt and the axial oxygen atoms increase once more to range between 89.7(3) and 96.6(3) (Table 7.6). The presence of a coordinated molecule in the equatorial position repels the axial Co-O bonds, causing them to reside at greater than 90 ° away. Removal of this equatorial molecule removes this electronic repulsion and allows the axial Co-O bonds to relax into values close to the 90 ° expected for such an environment. Introduction of NO into the equatorial position once again increases the axial Co-O angles due to extra repulsions, but the wide range of bond angles prevents an accurate comparison of these repulsive interactions with those experienced in the hydrated structure.

### 7.2.4.3 NO delivery

The NO gas was removed from the gas cell using a vacuum pump and the crystal was exposed to dynamic vacuum (CPO-283vac).

NO remained bound to the cobalt site, as evidenced by the presence of three oxygen atoms surrounding it at a distance of 1.029 Å (SEM = 0.064). The occupancy of the coordinated nitrogen atom was fixed at 47.0 % (the total occupancy of the three NO oxygen atoms when their thermal parameter was fixed at 0.05 Å<sup>2</sup>). A coordinated water molecule, O1W, was placed close to the nitrogen atom, its occupancy was fixed at 53.0 % and its thermal parameter and position was refined freely. The uncoordinated water molecules O2W and O3W could also be located within the pores; their thermal parameters were fixed at 0.05 Å<sup>2</sup> and their occupancies refined to 32.4 % and 18.7 % respectively.

Using the relationship between O1W and O2W occupancy derived in Chapter 6, the occupancy of O1W can be predicted from the crystallographically determined occupancy of O2W to be 48.9 %. This is very similar to that calculated from the NO oxygen atom occupancies, suggesting that the prediction of O1W occupancy using this method is reasonable.

With the gas cell still under dynamic vacuum, the temperature was increased to 373 K (CPO-373vac). At this temperature NO remained coordinated to the cobalt site with five oxygen atoms visible at an N-O distance of 1.065 Å (SEM = 0.005). N1 refined to an occupancy of 59.1 %, which is very close to the total NO oxygen occupancy of 51.6 %; the discrepancy is likely due to a small amount of coordinated water still occupying the cobalt site, as O1W is not fully removed from the framework at 373 K.

The temperature of the gas cell was increased further to 500 K (CPO-500vac). NO was still coordinated to the metal site with an occupancy of 19.2 % and four oxygen atoms were located around the N atom at an N-O distance of 1.031 Å (SEM = 0.025). The total occupancy of the four NO oxygen atoms is 16.8 %, so either there is a small amount of water still coordinated to the cobalt site, or the four NO oxygen

atoms do not accurately model the full amount of oxygen located around the nitrogen atom.

The gas cell was cooled to room temperature by removing the cryostream, the crystal was exposed to air and another data set was collected (CPO-293air). All the NO had been removed from the framework and replaced by water; O1W was found to be 100 % occupied and O2W, O3W and O4W could also be located at respective occupancies of 73.2 %, 35.6 % and 14.6 %.

### 7.2.5 Discussion

At 800 torr of NO, all the open metal sites of Co-CPO-27 were occupied, either by NO molecules or by recondensed water molecules. With one molecule of NO chemisorbed on each metal site an uptake of  $6.41 \text{ mmol g}^{-1}$  is expected, and in the experimental adsorption isotherm an uptake of approximately  $7 \text{ mmol g}^{-1}$  was observed. The excess uptake is due to physisorbed NO within the framework that cannot be located crystallographically.

When the NO gas was removed from the gas cell and the crystal was exposed to a vacuum at 283 K, some of the coordinated NO gas was removed from the framework. This could correspond to the fact that in the experimental adsorption isotherms,  $4.99 \text{ mmol g}^{-1}$  remained within the framework after it was exposed to vacuum, which is less than one molecule of NO per metal site. However, since the NO was displaced by water molecules in the crystal structure to give a fully occupied cobalt site, this reduction in NO occupancy is more likely to be due to the introduction of a small amount of moisture into the gas cell during the experimental process.

The crystal structures collected at 373 K and 500 K clearly demonstrated that water had been removed from the cobalt centres more easily than NO gas; at 500 K all the water had been removed but 19 % of the cobalt sites were still occupied by NO molecules. Although heating the framework under vacuum has been shown to remove some of the coordinated NO, the only way to remove it all was to expose the NO-loaded crystal to atmospheric moisture. The crystal structure of the framework

after exposure to air showed that all of the NO was delivered from the framework, supporting the results previously reported from NO delivery experiments.

Some loss of crystallinity was observed as the experiment progressed due to prolonged exposure to vacuum, heat, nitric oxide and X-rays, as reflected in the gradual increase in  $R_{int}$  values (Table 7.7). The data remained of reasonable quality after completion of numerous data sets over a period of over 12 hours, suggesting that the gas cell shows promise for lengthy experiments requiring varied experimental conditions.

Table 7.7: Summary of the crystallographic study of Co-CPO-27 dehydration, NO adsorption and NO delivery.

	Vacuum at 500 K (CPO-500dehyd)	Vacuum at 355 K (CPO-355dehyd)	800 torr NO at 283 K (CPO-NO-d)	Vacuum at 283 K CPO-283vac	Vacuum at 373 K CPO-373vac	Vacuum at 500 K CPO-500vac	Air at 293 K CPO-293air
<i>R</i> <sub>1</sub> / %	3.98	4.01	6.99	6.17	6.60	4.52	6.90
<i>R</i> <sub>int</sub> / %	5.70	5.49	7.97	8.47	8.75	7.63	10.47
Total N1/O1W occupancy / %	1.1(7)	13.6(6)	100	100	59.1	19.2	100
Total O <sub>NO</sub> occupancy / %	-	-	75.4(27)	47.0(16)	51.6(22)	16.8(12)	-
Calculated O1W occupancy / %	-	-	24.6	53.0	-	-	-

### 7.3 Carbon monoxide

Carbon monoxide is a diatomic molecule with the molecular orbital diagram shown in Figure 7.9. There is significant s-p mixing, so the  $\pi_{2p}$  orbital lies lower in energy than the  $\sigma_{2p}$  orbital. The bonding  $\sigma_{2p}$  orbital is the HOMO and the antibonding  $\pi_{2p}^*$  is the LUMO. Carbon monoxide has a bond order of 3 with a bond length of  $1.128 \text{ \AA}$ .<sup>1</sup>

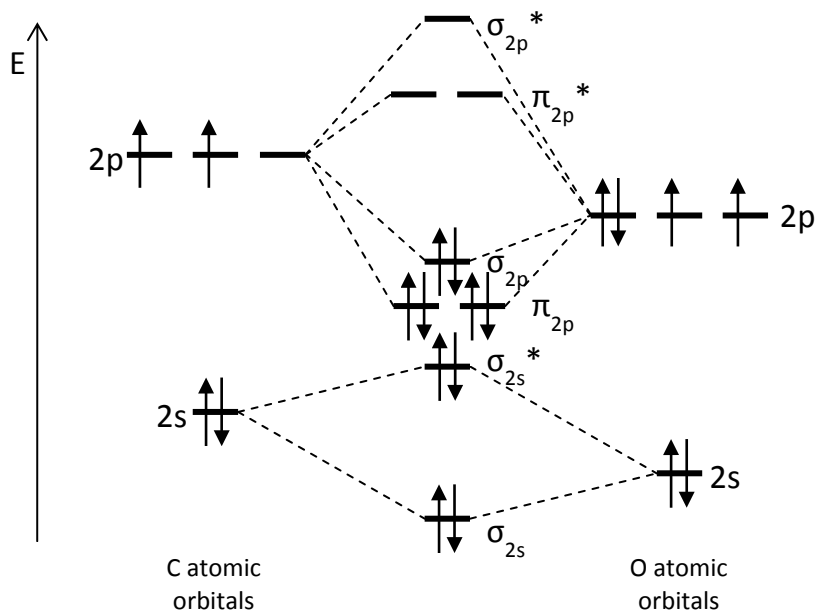


Figure 7.9: Molecular orbital diagram of carbon monoxide.

Carbon monoxide binds to transition metals through the carbon atom to give metal-carbonyl complexes (Figure 7.10). An sp-hybridised orbital on the carbon atom contains a lone pair of electrons which are donated into a vacant  $d_\sigma$  orbital on the metal atom. The excess electron density on the metal atom donates through the  $d_\pi$  orbitals on the metal centre into the antibonding  $\pi^*$  orbitals on the carbon atom. This backbonding interaction into the  $\pi^*$  orbitals strengthens the M-C bond while weakening the C=O bond.

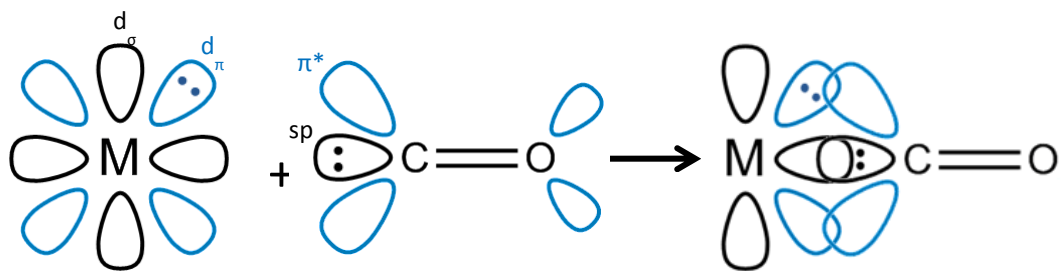


Figure 7.10: Electronic structure of CO ( $\pi$ -orbitals omitted) and its binding mode to a transition metal centre.

### 7.3.1 Applications

CO is a toxic gas produced mainly by the incomplete combustion of carbon-containing compounds, but despite its toxicity it has been found to play an important role in human biology. Since the 1950s it has been known that the breakdown of haem (a component of haemoglobin, Hb, used in the body to transport oxygen from the lungs to the rest of the body) produces CO in the body. In 1968 this was discovered to be due to an enzyme, haem oxygenase.<sup>23</sup>

The primary physiological use of CO is in bruising following a tissue injury. When a tissue is injured, free haem is released from haemoglobin to produce a dark red colour. Free haem is toxic to the body, so haem oxygenase catalyses its oxidation to produce a green pigment, biliverdin. This breaks down further to form a yellow pigment, bilirubin.<sup>23</sup> The carbon monoxide that is produced from the process coordinates to haem to give Hb-CO, which then carries the CO through the blood stream to the lungs for elimination by exhalation. The degradation of each haem group requires 3 equivalents of  $O_2$ , and the deoxygenated venous blood that is produced through providing this excess of  $O_2$  creates the blue colour also seen in bruising.

CO has a very low physiological concentration in the nanomolar region, with blood Hb-CO levels usually ranging from 0.4 – 1 %.<sup>24</sup> Similarly to NO, it is produced in endothelial cells before it diffuses into the smooth muscle where it causes muscle relaxation.<sup>25</sup>

CO can have a significant effect on the success of organ transplants. As soon as an organ is removed it begins to suffer from ischemia, where the cells are oxygen

deprived due to lack of blood flow. The subsequent re-warming of the organ as blood flow is restored (a process called reperfusion) can cause ischemia/reperfusion injury (I/R injury). However, CO has been shown to protect vascular endothelial cells which line the blood vessels, improving circulation and reducing problems related to I/R injuries.<sup>26</sup>

The simplest way in which CO could be delivered to the body is through inhalation. However, since CO is highly toxic above a certain concentration its administration in gaseous form would have to be very tightly controlled. The company Ikaria, for example, has designed the Covox delivery system specifically for the delivery of pharmaceutical-grade CO to a patient for inhalation, and it includes a number of design features that ensure its safety.<sup>27</sup> An alternative method for CO delivery is to bubble CO into a solution which can then be administered by injection, or into the cold storage solution used in organ transplants.<sup>26</sup> The oral administration of a methylene chloride solution induces CO production in the body through a metabolic process in the liver. Furthermore, some metal-carbonyl complexes have been developed as carbon monoxide releasing molecules (CORMs). The use of heavy metals in these compounds is a concern for administration in humans or human organs, but different CORMs release CO over different periods of time and appear to target different areas of the body, providing exciting possibilities for targeted CO delivery.<sup>27</sup>

### **7.3.2 Previous work**

The adsorption of CO onto Co-CPO-27 produces a Type I isotherm. The framework has a CO capacity of approximately 2.6 mmol g<sup>-1</sup> at room temperature, with significant hysteresis being observed. The isotherm is reversible at low pressures, showing that all adsorbed CO is removed from the framework under vacuum (Figure 7.11).

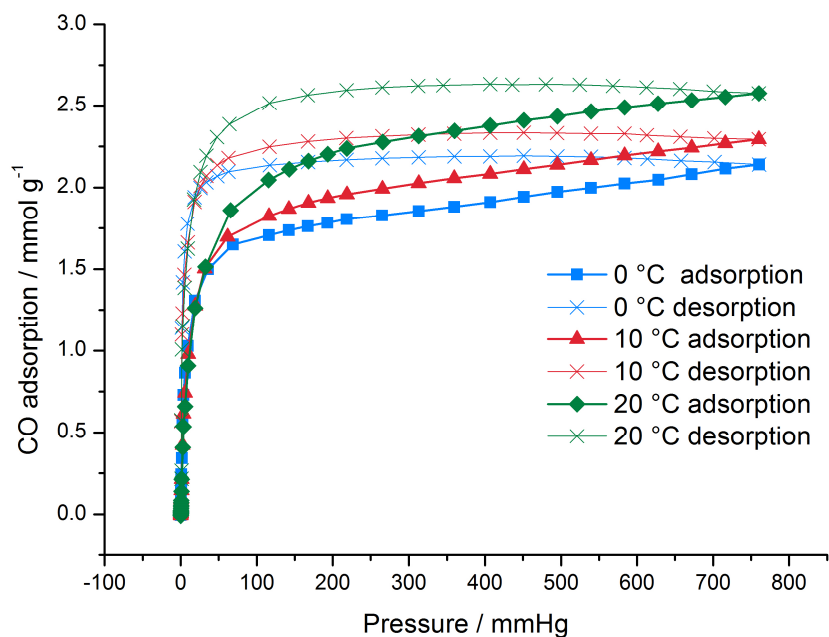


Figure 7.11: CO adsorption and desorption isotherm on Co-CPO-27 at variable temperatures.

Figure adapted from reference 28.

The release of all stored CO occurs over approximately 10 minutes (Figure 7.12). Powder X-ray diffraction shows that the framework retains crystallinity following CO adsorption and release, suggesting that its structure is not degraded during the adsorption process.<sup>28</sup>

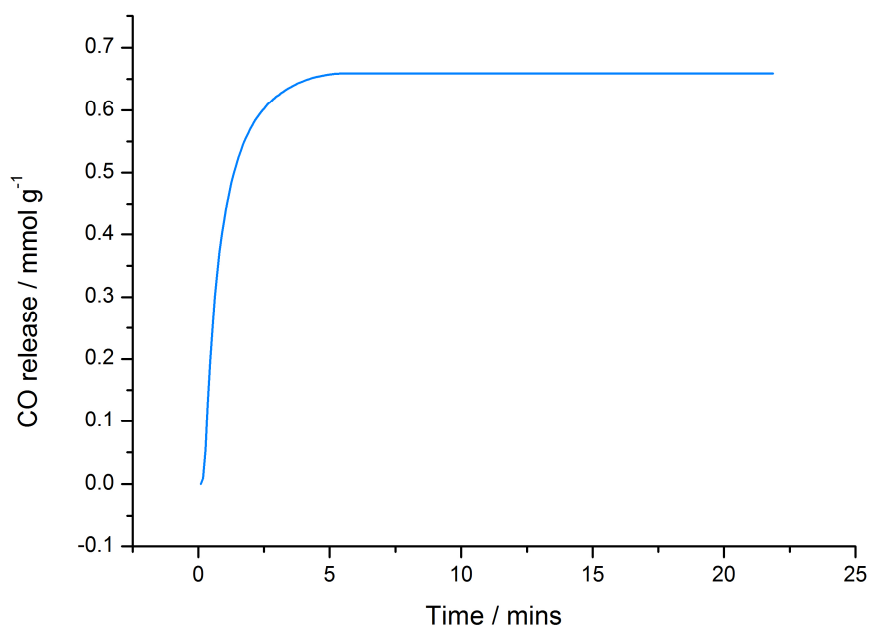


Figure 7.12: CO release from Co-CPO-27.

The interaction between adsorbed CO and the Ni-CPO-27 framework has been studied by IR (infrared) and EXAFS (extended X-ray absorption fine structure) spectroscopy. Although CO tends to form linear carbonyls<sup>29</sup> involving only a  $\sigma$ -bond and electrostatic interactions, IR studies suggest that some  $\pi$ -back-donation is present in the Ni-CPO-27/CO adduct, implying a slightly bent geometry. EXAFS results are compatible with a Ni-C-O angle between 170 ° and 180 °.<sup>30</sup>

### 7.3.3 Experimental

Crystal selection and dehydration was performed as described in Chapter 6.

After dehydration (CPO-500COdehyd), the cell was isolated from the gas rig and the vacuum pump was turned off. A small amount of CO was used to purge the lines and mixing chamber within the gas rig. CO gas was introduced into the mixing chamber to a pressure of approximately 800 torr before it was introduced into the gas cell. The pressure within the gas cell was gradually increased up to approximately 800 torr before all valves and the cylinder were closed. Data collection began after approximately 10 minutes to allow time for the gas to penetrate into the crystal (CPO-500CO).

The temperature of the cryostream was cooled to 400 K at 300 K h<sup>-1</sup>; the pressure within the gas cell was kept at approximately 800 torr and a data set was collected (CPO-400CO). The same procedure was followed to collect data at 298 K (CPO-298CO).

### 7.3.4 Results

After dehydration at 500 K, no water was observed on the cobalt sites. Following CO introduction at this temperature there was still no electron density observed crystallographically in the pores; no Q-peaks above 0.5 e Å<sup>-3</sup> were observed anywhere in the structure and  $R_I$  converged to 5.82 %. At this high temperature CO does not appear to coordinate to the metal sites.

CO was observed on the metal sites after the framework was cooled to 400 K (Figure 7.13). With the thermal parameters of C1M and O1M fixed at 0.05 Å<sup>2</sup>, the occupancy of C1M refined to 34 % and the occupancy of O1M refined to 8 %. The occupancies of C1M and O1M were fixed to be equal to a second free variable.

Restraints were introduced to fix the C-O bond length to be equal to that of a gaseous CO molecule (1.13 Å), and to fix the CO atoms to lie on two intersecting planes (O4-Co1-C1M-O1M and O2-Co1-C1M-O1M) using the FLAT instruction in order to keep the Co1-C1M-O1M bond angle linear. The Co-C1M bond length was fixed to be equal to 2.11 Å<sup>30</sup> and after refinement  $R_I$  converged to 4.76 %. The FLAT restraints were removed and  $R_I$  converged to 4.76 %, with 16 % of the cobalt coordination sites occupied by CO molecules and a Co-C1M-O1M bond angle of 175 (3) °.

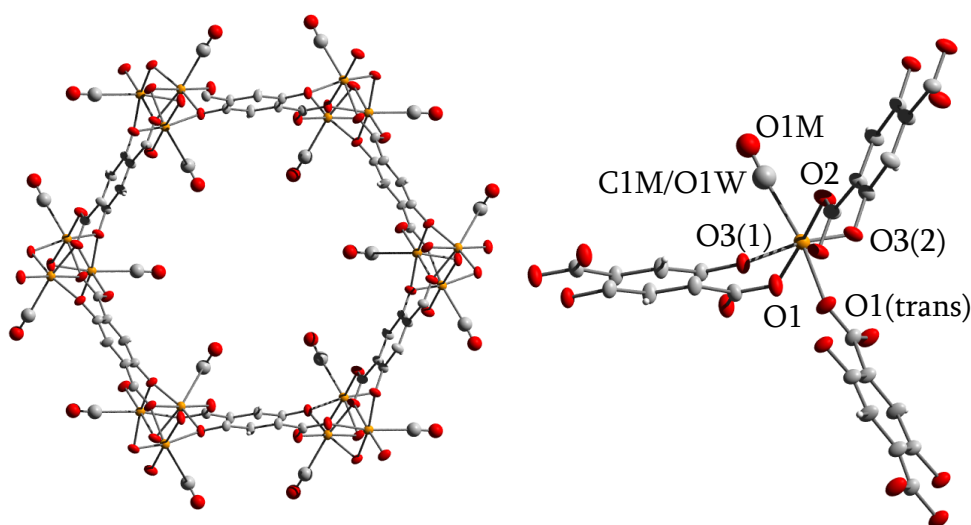


Figure 7.13: CO-loaded Co-CPO-27 at 355 K (CPO-400CO). (a) One pore. (b) One cobalt centre, with coordinated oxygen and carbon atoms labelled.

After cooling the gas cell to 298 K, CO was still observed coordinated to the cobalt. At this temperature the site was fully occupied, so its thermal parameter was allowed to refine freely with  $R_I$  converging to 15.04 %. The occupancy of O1M refined to only 26 %, suggesting that some of the cobalt atoms were coordinated to water molecules instead of CO molecules.

One method for dealing with the dual occupancy of the cobalt coordination site was to use the occupancy of the O2W site to predict that of O1W using the linear relationship described in Chapter 6. As such, the occupancy of O1W was fixed at 60.973 % and the occupancy of C1M was fixed at 39.027 %. Their thermal parameters refined to be 0.12469 Å<sup>2</sup> and 0.00415 Å<sup>2</sup> respectively, and  $R_I$  converged to 15 %. The inconsistently sized thermal parameters suggest that this is not a reliable method of modelling the CO occupancy within the framework at this temperature.

The occupancies of C1M and O1M were fixed to be equal to a second free variable, and O1W was placed close to the C1M atom with the occupancy fixed to be one minus the second free variable. Restraints were introduced to fix the C-O bond length to be equal to that of a gaseous CO molecule (1.13 Å), the Co-C1M bond length was fixed to be equal to 2.11 Å<sup>30</sup> and the FLAT instruction was used to fix the CO atoms to lie on two intersecting planes (O3-Co1-C1M-O1M and O2-Co1-C1M-O1M). *R*<sub>i</sub> converged to 15.07 %. The FLAT restraints were removed and *R*<sub>i</sub> converged to 15.11 %, with 14 % of the cobalt coordination sites occupied by CO molecules and a Co-C1M-O1M bond angle of 164(9) °.

Table 7.8: Bond lengths for hydrated, dehydrated (CPO-355dehyd) and CO-loaded Co-CPO-27 (CPO-400CO). (Atom labels correspond to Figure 7.13.)

	Hydrated Co-CPO-27 <sup>21</sup>	Dehydrated Co-CPO-27 (CPO-355dehyd)	CO-loaded Co-CPO-27 (CPO-400CO)
Co-C1M	-	-	2.1423(4) Å
Co-O1W	2.158(9) Å	2.2782(20) Å	-
Co-O1(trans)	2.191(8) Å	2.0731(17) Å	2.0719(4) Å
Co-O1	2.061(6) Å	2.0809(19) Å	2.0761(8) Å
Co-O2	2.037(6) Å	2.0109(18) Å	2.0094(8) Å
Co-O3(1)	2.042(5) Å	2.0016(18) Å	1.9929(7) Å
Co-O3(2)	2.047(7) Å	2.0237(16) Å	2.0139(4) Å

When a CO molecule coordinates to the vacant metal site the Co-O1(trans) bond shortens slightly from that in the dehydrated structure (Table 7.8), probably due to  $\pi$ -backbonding from cobalt to the CO  $\pi^*$  orbital. This is the opposite to the change observed in NO-loaded Co-CPO-27, where the bent coordination mode prevents backbonding.

Table 7.9: Bond angles (in degrees) around the cobalt atom of CO-loaded Co-CPO-27 (CPO-400CO). (Atom labels correspond to Figure 7.13.)

	C1M	O1(trans)	O1	O2	O3(1)
O1(trans)	171.0(1.0)	-	-	-	-
O1	92.2(1.0)	82.9(1)	-	-	-
O2	85.6(1.1)	99.0(1)	177.6(1)	-	-
O3(1)	91.0(1.0)	80.9(1)	80.9(1)	97.2(1)	-
O3(2)	90.7(1.0)	96.1(1)	81.2(1)	99.9(1)	162.9(1)

With CO coordinated to the cobalt site (Table 7.9), the angles between the carbon atom, cobalt and the axial oxygen atoms increase slightly from those observed in the dehydrated structure (Table 7.5) to range between 85.6(1.1) ° and 92.2(1.0) °. The presence of a coordinated molecule in the equatorial position repels the axial Co-O bonds, pushing them further away than 90 °, but the carbon monoxide position is only partially occupied so this effect is mild. Moreover, the partial presence of coordinated CO causes the related bonds to possess a large error. Some cobalt centres have open metal sites and have angles similar to the dehydrated structure, whereas other cobalt centres coordinate to a CO molecule, increasing the C1M-Co-O<sub>axial</sub> bond angles; the angles reported in Table 7.9 represent an average.

## 7.4 Olefins

### 7.4.1 Ethylene and propylene

#### 7.4.1.1 Previous work

Neutron powder diffraction carried out at 4 K was used to derive structural models of ethylene and propylene adsorbed onto Fe-CPO-27 thorough the use of Rietveld refinements.<sup>31</sup> Ethylene and propylene were shown to bind to the vacant iron site in side-on modes, with Fe-C distances of 2.42(2) Å and 2.56(2) / 2.60(2) Å respectively.

### 7.4.1.2 Experimental

Crystal selection and dehydration was performed as described in Chapter 6.

After dehydration the crystal was cooled to the desired temperature by adjusting the target temperature of the Cryostream. The cell was isolated from the gas rig and the vacuum pump was turned off. A small amount of ethylene or propylene was used to purge the lines and mixing chamber within the gas rig. Ethylene or propylene gas was introduced into the mixing chamber at a steady rate by a mass flow controller to a pressure of approximately 800 torr before the gas was introduced into the gas cell, and then it and the cylinder were both closed. Data collection began after approximately 10 minutes, in order to allow time for the gas to penetrate into the crystal.

### 7.4.1.3 Results

The study of ethylene adsorption on Co-CPO-27 within the *in situ* gas cell was extremely challenging. Due to the nature of a prototype piece of equipment such as the gas cell, a number of problems were encountered before suitable data could be collected.

As discussed at length in Chapter 6, dehydration of the Co-CPO-27 framework within the gas cell is a crucial step of the experiment. While the crystal structure of dehydrated or partially-dehydrated Co-CPO-27 is not new, it is important to know the percentage occupancy of water molecules on the cobalt coordination sites before any gas is introduced into the system. As such, wherever possible, dehydrated data sets were collected before gas adsorption was carried out.

Rehydration of the framework was the first problem encountered while pursuing the adsorption of olefin gases on Co-CPO-27. While a suitably dehydrated framework could be produced through prolonged heating under vacuum (423cpo), water returned to the metal sites upon introduction of ethylene. In early experiments the cobalt sites became fully rehydrated. This was due to problems with the apparatus. Leak tests carried out before ethylene introduction indicated that the gas cell did not leak, so the moisture reintroduction must have been due either to wet

ethylene or water from the dehydration procedure being retained within the system. In order to prevent such rehydration, a line drier was added to the ethylene line within the gas cabinet, the Teflon tube connecting the gas cell to the stainless steel tubing was heated with a heat gun after each dehydration procedure and before introduction of gas to the gas cell and the cryostream was moved very close to the gas cell while future dehydration procedures took place. Subsequent results showed 15.9 % rehydration of the cobalt site after cooling the gas cell to -20 °C (500cpo2b) followed by 52 % rehydration after ethylene introduction. As a further measure, heaters were added to all of the stainless steel tubing between the gas cell and the vacuum pumps to ensure that all water removed from the crystal during dehydration was eliminated from the system entirely and did not condense within the tubing.

During another experiment, ethylene introduction at -50 °C increased the water occupancy of the cobalt site from 6.7 % to 8.9 % (500cpo3b and CPO-223eth). This very small increase suggested that the precautions against rehydration of the framework were successful. Ethylene molecules could not, however, be located on the metal sites, or indeed elsewhere in the framework. Platon SQUEEZE was used to estimate the electron density within the pores; adsorption of ethylene within the framework pores should result in an increase in the excess electron count. When dehydrated to an O1W occupancy of 6.7 %, SQUEEZE produced an excess electron count of 161. After ethylene introduction, this decreased to 94. These results seem counterintuitive, and are probably due to data quality;  $R_{int}$  for 500cpo3b at 9.3 % was higher than  $R_{int}$  for CPO-223eth at 4.7 %, and an experimental technique such as SQUEEZE cannot account for such differences.

A similar technique was used to greater success during a different experiment. Dehydrated Co-CPO-27 (420cpo1b) had an  $R_{int}$  of 7.42 % and a water occupancy of 18.7 %. SQUEEZE gave an excess electron count of 189. After ethylene introduction,  $R_{int}$  remained similar at 6.0 %, water occupancy increased to 26.9 % and SQUEEZE produced an electron count of 359 electrons. This increase in electron count is expected considering that ethylene is adsorbing to the unoccupied metal ions within the framework pores, but some of the increased electron density is probably due to excess disordered water in the pores.

In order to examine ethylene adsorption on Co-CPO-27, low O1W occupancy is very important. Therefore, the data from CPO-223eth were examined more carefully. After exposure to 1 atmosphere of ethylene at  $-50\text{ }^{\circ}\text{C}$ , the cobalt sites were 10.6 % occupied with water molecules. No Q-peaks over 0.22 electrons  $\text{\AA}^{-3}$  could be located within the pores. Data collection at a lower temperature was not possible due to the build-up of ice around the gas cell head.

It was not possible to locate ethylene crystallographically within the framework due to the weak bonds formed between the cobalt atoms and the adsorbed ethylene molecules. Instead, the program COOT (crystallographic object-oriented toolkit) was used to visualise electron density difference maps.<sup>32</sup> Around the water sites, two clear areas of excess electron density began to appear at  $0.2590\text{ e \AA}^{-3}$ , growing significantly as lower electron densities were visualised. This electron density was positioned in a side-on manner similar to that observed by Bloch et al,<sup>31</sup> therefore suggesting the location of the two carbon atoms of an ethylene molecule. The distance between the two proposed carbon atoms was  $1.20\text{ \AA}$ , with Co-C<sub>eth</sub> distances of  $2.40$  and  $2.61\text{ \AA}$ ; very similar to the  $2.42(2)\text{ \AA}$  distance obtained from neutron data.

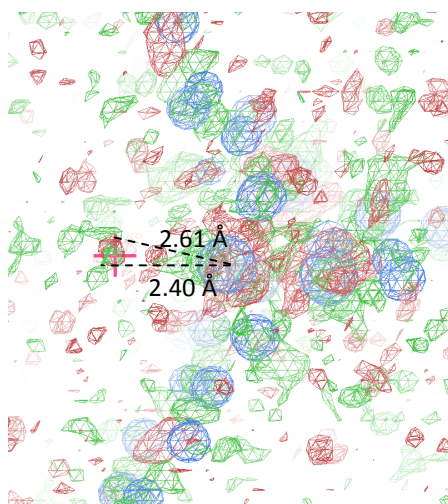


Figure 7.14: Electron density difference map of CPO-223eth at  $0.2081\text{ e \AA}^{-3}$ , viewed down the  $c$ -axis, centred around the cobalt atom and with Co-C<sub>eth</sub> distances labelled. Blue indicates modelled atoms; green indicates excess unmodelled electron density; red indicates over-modelled electron density. The pink cross shows the position of the 10.6 % occupied water molecule.

After exposure to 1 atm propylene at 80 °C, the open cobalt sites were occupied by 14.1 % water. No Q-peaks over 0.47 electrons Å<sup>-3</sup> could be located within the pores. It was not possible to locate propylene crystallographically (CPO-353prop). The gas cell was cooled to 0 °C, at which point the cobalt sites were 47.3 % occupied by water molecules and no Q-peaks above 0.47 electrons Å<sup>-3</sup> were present within the pores. It remained impossible to locate propylene crystallographically (CPO-293prop).

Using COOT, some areas of electron density began to appear around the water molecule at 0.4673 e Å<sup>-3</sup>. This electron density appeared to be on a side-on manner facing down the pores in a similar way to that reported by Bloch et al.<sup>31</sup> When carbon atoms representing a propylene molecule were positioned at the most likely three areas of electron density, the C=C double bond was calculated to be 1.03 Å, the C-C single bond was calculated to be 1.00 Å and the bond angle was 113.3 °. All three measurements disagree significantly with the literature values of 1.34 Å, 1.50 Å and 1.24 ° respectively.<sup>33</sup> Similarly, the Co-C bond lengths to the sp<sup>2</sup> carbon atoms are 2.44 Å and 1.92 Å; considerably shorter than the 2.60 Å and 2.56 Å distances previously reported.<sup>31</sup> This suggests that the small amount of electron density seen around the water molecule is not due to propylene adsorption on the metal sites, but is likely due to an underestimation of the thermal motion of the water molecule. The water occupancy of this site is high at 47.3 %, so it is perhaps unsurprising that adsorbed propylene molecules cannot be located within the crystal structure.

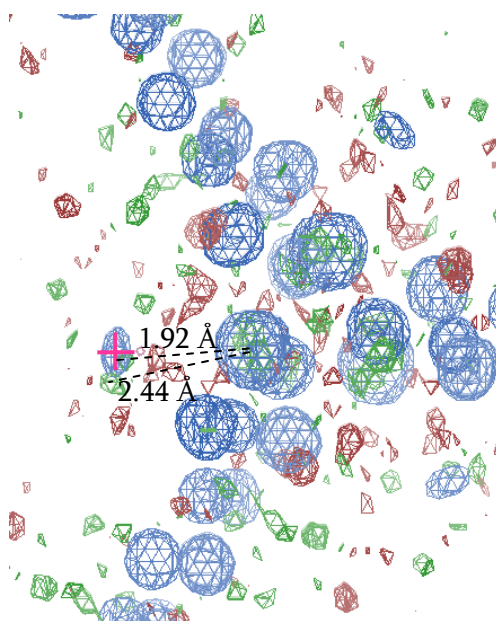


Figure 7.15: Electron density difference map of CPO-293prop at  $0.4673 \text{ e } \text{\AA}^{-3}$ , viewed down the  $c$ -axis, centred around the cobalt atom and with Co-C<sub>prop</sub> distances labelled. The pink cross shows the position of the 47.3 % occupied water molecule.

## 7.5 Summary

The static gas cell has been used successfully to obtain crystal structures of NO-loaded and CO-loaded Co-CPO-27, and to infer the presence of ethylene within the same framework. Data was generally of good quality with  $R_{int}$  values frequently below 10 %, but data with higher  $R_{int}$  values still provided meaningful results.

The full dehydration-adsorption-release cycle of NO adsorption onto Co-CPO-27 was studied crystallographically and it was revealed that the application of heat and vacuum, in an analogous procedure to that used for dehydration, failed to remove all of the adsorbed nitric oxide from the cobalt sites. Exposure to moisture in the air displaced all remaining NO and fully rehydrated the framework. Even after a prolonged experiment such as this, which lasted over 12 hours and involved many data collections, the data obtained from the gas cell was still of good quality.

There is a large amount of further work that could be performed using the environmental gas cell. It would be interesting to study *in situ* gas adsorption on different materials such as other MOFs or zeolites. Similarly, different gases would be interesting to study on Co-CPO-27 such as H<sub>2</sub>S, SO<sub>2</sub>, CO<sub>2</sub> and other olefins.

Expanding the results already obtained would also be another interesting field to investigate; *in situ* isotherms could be obtained by introducing tiny amounts of NO or CO into the gas cell within a dry carrier gas such as N<sub>2</sub> or Ar. This would also utilise the mixing chamber within the gas mixing rig for the first time.

## 7.6 CIFs

Table 7.10: Key to CIFs (Appendix) referred to in Chapter 7.

Reference code	CIF name
CPO-500dehyd	37.cif
CPO-355dehyd	39.cif
CPO-NO-a	40.cif
CPO-NO-b	41.cif
CPO-NO-c	42.cif
CPO-NO-d	43.cif
CPO-283vac	44.cif
CPO-373vac	45.cif
CPO-450vac	46.cif
CPO-500vac	47.cif
CPO-293air	48.cif
CPO-500COdehyd	49.cif
CPO-500CO	50.cif
CPO-400CO	51.cif
CPO-298CO	52.cif
423cpo	13.cif
500cpo2b	20.cif
500cpo3b	22.cif
420cpo1b	12.cif
CPO-223eth	53.cif
CPO-353prop	54.cif
CPO-273prop	55.cif

## 7.7 References

1. D. R. Lide, *CRC handbook of chemistry and physics : 2008-2009*, CRC Press, Boca Raton; London; New York, 89th edn., 2008.
2. R. H. Crabtree, *The organometallic chemistry of the transition metals*, John Wiley, Hoboken, N.J., 4th edn., 2005.
3. C. N. Hall and J. Garthwaite, *Nitric Oxide*, 2009, **21**, 92–103.
4. A. Butler and R. Nicholson, *Life, death, and nitric oxide*, RSC, Cambridge, UK, 2003.
5. M. R. Schäffer, U. Tantry, S. S. Gross, H. L. Wasserkrug, and A. Barbul, *J. Surg. Res.*, 1996, **63**, 237–240.
6. R. L. Mancinelli and C. P. McKay, *Appl Environ Microbiol.*, 1983, **46**, 198–202.
7. M. S. Crane, R. Ollosson, K. P. Moore, A. G. Rossi, and I. L. Megson, *J. Biol. Chem.*, 2002, **277**, 46858–46863.
8. L. J. Ignarro, *Proc. Natl. Acad. Sci. USA*, 2002, **99**, 7816–7817.
9. R. H. Clark, T. J. Kueser, M. W. Walker, W. M. Southgate, J. L. Huckaby, J. A. Perez, B. J. Roy, M. Keszler, and J. P. Kinsella, *N Engl J Med*, 2000, **342**, 469–474.
10. J. P. Kinsella, G. R. Cutter, W. F. Walsh, D. R. Gerstmann, C. L. Bose, C. Hart, K. C. Sekar, R. L. Auten, V. K. Bhutani, J. S. Gerdes, T. N. George, W. M. Southgate, H. Carriedo, R. J. Couser, M. C. Mammel, D. C. Hall, M. Pappagallo, S. Sardesai, J. D. Strain, M. Baier, and S. H. Abman, *N Engl J Med*, 2006, **355**, 354–364.
11. R. Weller, A. D. Ormerod, R. P. Hobson, and N. J. Benjamin, *J. Am. Acad. Dermatol.*, 1998, **38**, 559–563.
12. R. Weller and M. J. Finnen, *Nitric Oxide*, 2006, **15**, 395–399.
13. A. D. Ormerod, P. Copeland, I. Hay, A. Husain, and S. W. B. Ewen, *J. Investig. Dermatol.*, 1999, **113**, 392–397.
14. C. C. Miller, M. K. Miller, A. Ghaffari, and B. Kunimoto, *J. Cutan. Med. Surg.*, 2004, **8**, 233–238.
15. P. S. Wheatley, A. R. Butler, M. S. Crane, S. Fox, B. Xiao, A. G. Rossi, I. L. Megson, and R. E. Morris, *J. Am. Chem. Soc.*, 2006, **128**, 502–509.
16. B. Xiao, P. S. Wheatley, X. Zhao, A. J. Fletcher, S. Fox, A. G. Rossi, I. L. Megson, S. Bordiga, L. Regli, K. M. Thomas, and R. E. Morris, *J. Am. Chem. Soc.*, 2007, **129**, 1203–1209.
17. A. C. McKinlay, B. Xiao, D. S. Wragg, P. S. Wheatley, I. L. Megson, and R. E. Morris, *J. Am. Chem. Soc.*, 2008, **130**, 10440–10444.
18. P. J. Byrne. Structural studies of ionic liquids and ionothermally-prepared materials. PhD Thesis, University of St Andrews, 2009.

19. A. C. McKinlay. New Nitric Oxide Releasing Materials. PhD Thesis, University of St Andrews, 2010.
20. A. Altomare, M. C. Burla, M. Camalli, G. L. Cascarano, C. Giacobazzi, A. Guagliardi, A. G. Moliterni, G. Polidori, and R. Spagna, *J. Appl. Crystallogr.*, 1999, **32**, 115–119.
21. P. D. C. Dietzel, Y. Morita, R. Blom, and H. Fjellvåg, *Angew. Chem. Int. Ed.*, 2005, **44**, 6354–6358.
22. C. A. Fyfe, D. H. Brouwer, A. R. Lewis, L. A. Villaescusa, and R. E. Morris, *J. Am. Chem. Soc.*, 2002, **124**, 7770–7778.
23. R. Tenhunen, H. S. Marver, and R. Schmid, *Proc. Natl. Acad. Sci. USA*, 1968, **61**, 748–755.
24. D. R. Von Burg, *J. Appl. Toxicol.*, 1999, **19**, 379–386.
25. R. Motterlini, J. E. Clark, R. Foresti, P. Sarathchandra, B. E. Mann, and C. J. Green, *Circulation Research*, 2002, **90**, e17–e24.
26. A. Nakao, A. M. K. Choi, and N. Murase, *J. Cell. Mol. Med.*, 2006, **10**.
27. R. Motterlini and L. E. Otterbein, *Nat. Rev. Drug Discov.*, 2010, **9**, 728–743.
28. P. K. Allan. A Study of Metal-Organic Frameworks for the Storage and Release of Medical Gases. PhD Thesis, University of St Andrews, 2012.
29. D. Cappus, J. Klinkmann, H. Kühlenbeck, and H.-J. Freund, *Surf. Sci.*, 1995, **325**, L421–L427.
30. S. Chavan, J. G. Vitillo, E. Groppo, F. Bonino, C. Lamberti, P. D. C. Dietzel, and S. Bordiga, *J. Phys. Chem. C*, 2009, **113**, 3292–3299.
31. E. D. Bloch, W. L. Queen, R. Krishna, J. M. Zadrozny, C. M. Brown, and J. R. Long, *Science*, 2012, **335**, 1606–1610.
32. P. Emsley and K. Cowtan, *Acta Crystallogr., Sect D: Biol. Crystallogr.*, 2004, **60**, 2126–2132.
33. D. R. Lide and D. Christensen, *J. Chem. Phys.*, 1961, **35**, 1374–1379.

## CHAPTER 8: Conclusions and further work

The overall aim of this thesis was to assess the capacity of MOFs with open metal sites for the separation of olefin mixtures through sorption and structural studies.

Adsorption and desorption isotherms were obtained for ethylene and propylene on Ni-CPO-27, HKUST-1 and STAM-1 at a range of temperatures. Of the two gases investigated, propylene adsorption isotherms showed a steeper increase at low pressures on all frameworks, which corresponded to higher enthalpies of adsorption at zero coverage. Comparison of the enthalpies of adsorption as well as direct comparisons of the adsorption isotherms suggested that the separation of olefins would be possible using MOFs with open metal sites such as these.

The adsorption of ethylene onto STAM-1 was shown to occur through a two-step process, where the initial adsorption of ethylene into the hydrophilic pores altered the framework to allow further uptake into the hydrophobic pores. Such a two-step adsorption process was not observed for propylene, but the overall uptake was very similar. Either propylene was adsorbed into both types of pore from the beginning, or propylene adsorption into the hydrophilic pores at low pressures was significant enough that the change in framework uptake could not be observed using this isotherm measuring technique. In order to examine this further, more detailed isotherms at low pressures would be required for both ethylene and propylene adsorption on STAM-1.

IAST was used to estimate the selectivities of Ni-CPO-27 and HKUST-1 for the separation of propylene/ethylene binary mixtures. Both frameworks were selective for propylene over ethylene, as predicted in Chapter 4. Ni-CPO-27 and HKUST-1 both showed higher selectivities for propylene at 40 °C than 25 °C due to the greater differences between uptake at higher temperatures. Of the combinations studied, separation of a 99 % ethylene/propylene mixture at 40 °C using HKUST-1 showed the highest selectivity.

The selectivities obtained from IAST indicated that the selectivity of HKUST-1 at 40 °C had not reached a maximum at the pressures investigated here. Adsorption isotherms for both gases on HKUST-1 at pressures above 800 torr and the subsequent calculation of selectivities at higher pressures would reveal the maximum selectivity as predicted using the IAST.

TPD experiments for ethylene on Ni-CPO-27 and HKUST-1 indicated that regeneration of the framework would be possible at relatively low temperatures under the flow of an inert gas. This is very promising for their use in industry as a support for the separation of olefins. The study of propylene desorption from the two frameworks would also be very useful; the enthalpy of adsorption for this gas is higher than for ethylene on both frameworks, so it would be expected that the enthalpy of desorption would also be higher and that the TPD peaks would occur at higher temperatures.

Since IAST indicates that separation of propylene and ethylene is possible, experimental separations would be a very interesting and promising avenue for further work. The regenerability of the frameworks after separation is also very important; repeated adsorption/desorption isotherms on the same sample would reveal the working capacity of the frameworks, which is a very important factor to consider for industrial separation procedures.

The separation of other olefins would be another interesting area to investigate; but-1-ene could be compared to both ethylene and propylene to investigate the effect of chain size on separation capacity, and branched isobutene could be compared to linear but-1-ene to investigate the adsorption of a branched olefin and its consequential steric effects. In order to carry out these comparisons, it would be necessary to obtain adsorption and desorption isotherms for but-1-ene and isobutene at a range of temperatures, as well as TPD spectra.

Furthermore, experimental separation experiments would be an interesting avenue to pursue and the breakthrough curves obtained would provide experimental selectivities that could be compared to those predicted from IAST.

The development of the *in situ* environmental gas cell has progressed significantly, with changes being made to the glass head, the gas delivery system, the position of the vacuum pumps and the experimental procedure. Complete dehydration of Co-CPO-27 was extremely challenging, and so many partially hydrated crystal structures were collected throughout the development process; these were used to increase the understanding of the dehydration process.

The *in situ* gas cell has been developed to a standard that has allowed the study of the full dehydration-adsorption-delivery cycle for NO on Co-CPO-27. NO was shown to bind to cobalt in a bent conformation, and the NO-loaded crystal structure greatly improved upon the models suggested by McKinlay et al.<sup>1</sup> and Byrne<sup>2</sup>. After the prolonged development of both the gas cell itself and the gas delivery system, a single crystal of Co-CPO-27 could be dehydrated, loaded with NO and exposed to vacuum and air without removing the gas cell from the diffractometer. The quality of the data after 12 hours and a number of data collections was slightly lower, as evidenced by higher  $R_{int}$  values, but was still of high quality.

Treatment of the NO-loaded structure during the refinement process was complicated by the partial rehydration of the Co-CPO-27 crystal upon cooling. Different methods of refining the occupation of the cobalt-site were attempted and discussed in detail in Chapter 7. Some NO was removed from the framework with the application of vacuum and heat, but full NO delivery only occurred after the crystal was exposed to atmospheric moisture.

Ethylene and propylene-loaded Co-CPO-27 structures could not be obtained using the techniques described in this thesis. The position of adsorbed ethylene could be suggested from examination of electron density maps, but this was not possible with propylene. Experiments performed at lower temperatures may provide a crystal structure in which the adsorbed olefin can be located crystallographically, as with neutron diffraction performed at 4 K by Bloch et al.<sup>3</sup>, but at temperatures below -20 °C the formation of ice on the outside of the gas cell prevented data collection.

There are significant differences between the adsorption behaviour of ethylene and propylene with propylene having a higher enthalpy of adsorption.

However, only ethylene can be located crystallographically. This could be due to steric effects of the larger propylene molecule preventing its approach to the metal site at the corner of the pore. Further work including diffraction studies of ethylene and propylene on HKUST-1 would go some way towards investigating this theory.

The successful development of the environmental gas cell could lead to a huge amount of further research involving the study of crystals under different gaseous environments. Different MOFs or zeolites could be investigated, with or without open metal sites. Similarly, different gases could be studied on Co-CPO-27 or on other MOFs. By introducing small amounts of NO or CO into the gas cell within a dry carrier gas, *in situ* isotherms could be obtained, which would enable a greater understanding of the gas loading process.

The adsorption of olefins into Co-CPO-27 could be studied crystallographically at higher pressures using a diamond anvil cell. Longer chained olefins that are liquids at room temperature, such as pent-1-ene and hex-1-ene, could be loaded into a diamond anvil cell and used as the hydrostatic medium. By squeezing the olefin into the pores, coordinated water may be displaced from the metal sites, thus potentially alleviating the problem of rehydration.